Title

Innovation in Photovoltaic Science, Engineering, and Policy: A Potential Trillion-Dollar Global Industry for Sustainable Energy

Permalink

Author

Zheng, Cheng

Publication Date

2014

Peer reviewed|Thesis/dissertation

Innovation in Photovoltaic Science, Engineering, and Policy: A Potential Trillion-Dollar

Global Industry for Sustainable Energy

By

Cheng Zheng

A dissertation submitted in partial satisfaction of the

Requirements for the degree of

Doctor of Philosophy

in

Engineering – Mechanical Engineering

in the

Graduate Division

of the

University of California, Berkeley

Committee in charge:

Professor Ralph Greif, Co-chair
Professor Costas P. Grigoropoulos, Co-chair
Professor Van P. Carey
Professor Daniel M. Kammen

Fall 2014

Abstract

Innovation in Photovoltaic Science, Engineering, and Policy: A Potential Trillion-Dollar

Global Industry for Sustainable Energy

By

Cheng Zheng

Doctor of Philosophy in Engineering – Mechanical Engineering

University of California, Berkeley

Professor Ralph Greif, Co-chair

Professor Costas P. Grigoropoulos, Co-chair

The solar photovoltaic (PV) technology was an expensive niche energy source only for satellite applications, hallmarked by the Bell Lab's launch of the Telstar satellite with PV cells in 1962. Over the past decades, the accumulation of vast amount of effort across various disciplines in science, engineering, and policy has enabled the phenomenal growth of the solar PV industry into a global enterprise with about 140 gigawatt (GW) of cumulative installations by the end of 2013. Further cost reduction through innovation holds the promise in deploying terawatt (TW)-scale solar PV systems globally in both developed and developing countries, meeting growing energy demand and mitigating climate change. Chapter 1 presents a big picture view of the unsustainable path, heavily relying on fossil fuels, in the current global energy landscape.

The main body of the dissertation examines the solar PV technology from a holistic and interdisciplinary perspective: from the basic research, to innovations in manufacturing and installing PV modules, to the driving energy policies. Chapter 2 offers a fundamental understanding of the PV technology and a review on recent scientific advances in improving PV efficiency (W/m^2).

Chapter 3 reviews the state-of-the-art process flow in manufacturing commercial PV modules. In the context of pursuing further reduction in manufacturing cost (\$/m^2), the thin Si film concept and its recent research effort are reviewed. Aiming to explore novel ways to produce high-quality seed crystals for thin Si film deposition, the key findings of the laser crystallization experiment is presented in Chapter 4. The fundamental thermophysics of nucleation and crystal growth is first reviewed, which highlights the importance of temperature evolution and heat transport in modelling the ultrafast laser crystallization process. Laser

crystallization of a range of Si nanostructures are then carried out to study the nucleation and crystal growth behavior under some novel conditions, such as suspended narrow Si membranes and Si nanoparticles confined on top of oxide nanostructures.

The cost of a PV module ($/W) is determined by both its rated efficiency (W/m^2) and its manufacturing cost ($/m^2). However, the same PV module with the same cost can lead to significantly different levelized cost of electricity (LCOE) in $/kWh, depending on the location and configuration of the installed PV system. Chapter 5 starts with an overview of the geographic distribution of solar resources and retail electricity rates, which yield a range of grid parity points across the world. Then, energy yield simulations for different PV panel tilt configurations are carried out using the angle-and-wavelength-resolved solar irradiance data, to examine the effect of angular and spectral variations in the solar spectrum on system performance.

Energy policies have been the driving forces for the phenomenal progress of the PV technology: the continuing reduction in cost and the rapid growth in deployment. Chapter 6 first reviews major policy instruments for PV, and then discusses about a few important policy lessons from the rapid development of the global PV industry during 2000-2013. Concerned with the mounting fiscal pressure from deployment incentives and focused on further cost reductions, an innovation-focused policy framework is proposed to revive the PV manufacturing sector and to pursue an innovation-driven global PV industry moving forward.

Table of Contents

List of Figures

ii

Acknowledgements

Living in an era with increasing needs for sustainable social and economic models, to meet the world's expectation for further economic development, I feel very fortunate to spend the past five and a half meaningful years in Berkeley, pursuing my PhD study in clean energy from an interdisciplinary and holistic approach, and interacting with inspiring thought leaders seasoned and young. I am forever indebted to the Cal community, which has been instrumental in shaping my global perspectives, discovering my true passions, and developing my essential skills.

First, I would like to thank Professor Ralph Greif for his insight and encouragement. I am fortunate to have him as the co-chair of the dissertation committee, whose incisive input has greatly strengthened the physics aspect of the dissertation. I also learnt from him the delicate art of being confident as well as being humble.

I would also like to thank Professor Costas P. Grigoropoulos for his patient guidance and support on the experiment. He introduced me to the fascinating topic of recrystallizing semiconductor materials by ultrafast localized laser heating, which formed the experimental part of the dissertation.

I would also like to thank Professor Daniel M. Kammen, whom I had the privilege to work with on the energy policy topics, for his invaluable advices, resources, and insights. Deep appreciation and thanks go to Professor Van P. Carey for lending his advices and expertise in the topics of phase change and statistical thermophysics. I thank them for their time to serve on the dissertation committee and their invaluable inputs to the manuscript. I am also grateful for the advices, insights, inspirations, and support from Professor Arun Majumdar, who brought me to the Berkeley graduate school before he went on to found the ARPA-E.

My sincere gratitude goes to the generous financial support from the Singapore NRF Clean Energy PhD Scholarship, which has created the essential room for me to explore and take risks during the whole PhD course. Heartfelt thanks go to members of the Laser Thermal Lab and the Majumdar group, who have been extremely helpful and kind to share resources and experiences with me. I thank members of the Marvell Nanofabrication Lab, who have trained me on various pieces of clean room equipment, shared their process recipes, and sometimes lent me crucial help during fabrication.

Last but not least, I thank my dear family and friends, who have been the most reliable source of emotional support during this challenging and fruitful journey. During difficult times, their kindness, care, appreciation, encouragement, and love have enabled me to quickly heal up and regain my feet to overcome the challenges.

1. The Global Economy with Sustainable Energy

1.1. From the Unsustainable Fossil Fuel Path to Sustainable Energy

The world's energy consumption is currently dominated by fossil fuel sources: about 87% of the 12.7 billion tons of oil equivalent (toe) of primary energy consumption in 2013 is from coal, oil, and natural gas [1]. Furthermore, the world's energy consumption is likely to increase significantly in the next decades in various projections [1-3]. According to the BP outlook [1], the world's energy consumption could increase by more than 40% from 12.7 btoe in 2013 to 17.6 btoe in 2035, where the share for fossil fuels decreases to 81.6% and the share for non-hydro renewables (solar, wind, and others) increases to 6.4%.

This heavy reliance on fossil fuels in the current global energy landscape has important implications on the climate change dialogue. Without low-carbon and affordable energy sources, such as non-hydro renewable energy (renewables), hydro-electricity, and nuclear-electricity, there will be unavoidable conflict between mitigating energy-related CO_2 emissions and accommodating the developing countries' growing energy needs (Fig. 1.1). In a business-as-usual scenario where the per capita CO_2 emissions from the developed and developing countries converge, the CO_2 emissions from the developing countries could potentially triple to 65 billion tons per year from the 21 billion tons per year in 2013. A more sustainable path, in the context of mitigating climate change, would require drastic increase in using renewable energy sources on the global scale.

Meeting the growing energy demand in the developing countries with growing fossil fuel consumption is unsustainable also due to prevailing environmental pollution problems. For example, the urban air pollution across major Chinese cities has now become a highly concerning social problem [4], which could lead to serious health consequences and cost [5]. China's air pollution problem largely arises from its rapid increase in fossil fuel consumption over the past decade (**Fig. 1.2**): China's coal consumption almost tripled between 2000 and 2012, and oil consumption more than doubled between 2000 and 2012. Pertaining to urban air pollution, the vehicle ownership in Beijing and Shanghai (the two largest cities in China) in 2012 is about 3.3. times and 2.5 times that in 2000, respectively. This rapid increase in the number of vehicles and associated tailpipe emissions is a main factor underlying the worsening air quality across major Chinese cities.

Besides the adverse environmental effect, growing consumption of fossil fuels with finite reserves is physically unsustainable (**Fig. 1.3**). With the current rate of production, the world's proven reserves of oil and natural gas can only sustain another 50 years' supply. Moreover, these fossil fuel reserves are also expected to become more costly to extract in the future: the annual capital expenditure on the supply chains of coal, oil, and natural gas has more than doubled between 2000 and 2013, and reached $950 billion in 2013 [6].
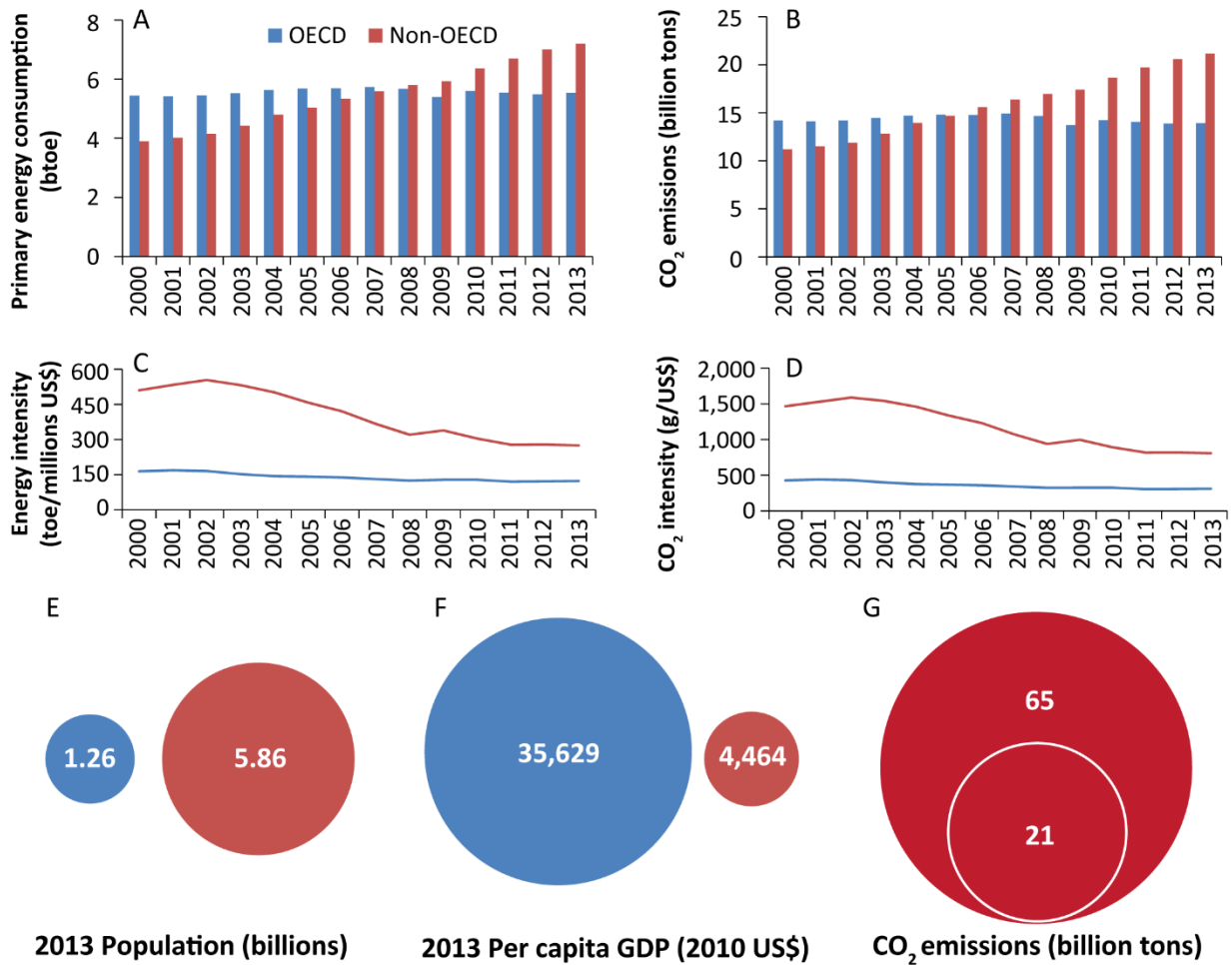
Figure 1.1. Implications of global economic growth on CO_2 emission targets. The Organization for Economic Co-operation and Development (OECD) countries (in blue) and the non-OECD countries (in red) have exhibited opposite trends in primary energy consumption (A) and related CO_2 emissions (B). The primary energy consumption is measured in billion tons of oil equivalent (btoe). Both energy intensity (C) and CO_2 intensity (D) for the non-OECD countries have been declining and converging to those of the OECD countries. The non-OECD countries currently have more population (E) and less per capita GDP (F) than the OECD countries. With a population of about 1.3 billion, China's energy-related CO_2 emissions have more than doubled from 3.4 billion tons in 2000 to 9.5 billion tons in 2013. If the non-OECD countries evolve to have the same per capita CO_2 emissions as the OECD countries, their CO2 emissions could eventually triple to 65 billion tons from 21 billion tons in 2013 (G). All prices are inflation-adjusted to the 2010 U.S. dollars. Sources: BP and World Bank.
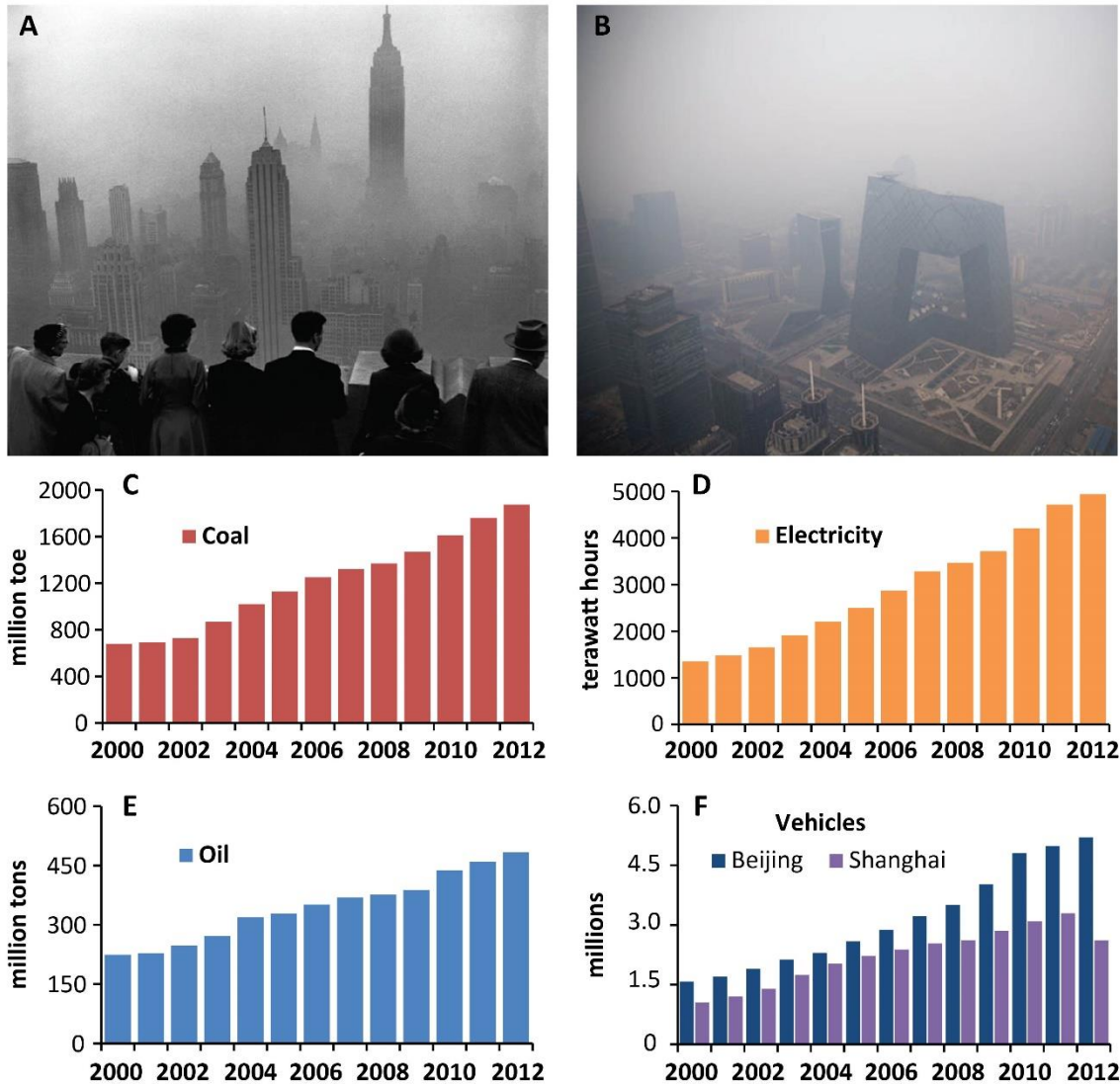
Figure 1.2. Urban air pollution caused by fossil fuel consumption. Images A and B visualize the air pollution in New York City in 1953 and that in Beijing in 2013. The worsening urban air quality in China is largely driven by its rapid increase in fossil fuel consumption, such as coal (C) and oil (E). Coal is the primary energy source for electricity generation in China (D), and the ownership of automobiles in major Chinese cities have more than doubled over the past decade (F). Image courtesy: NYT [4] and Vintage [7]. Source: BP and Chinese local government.
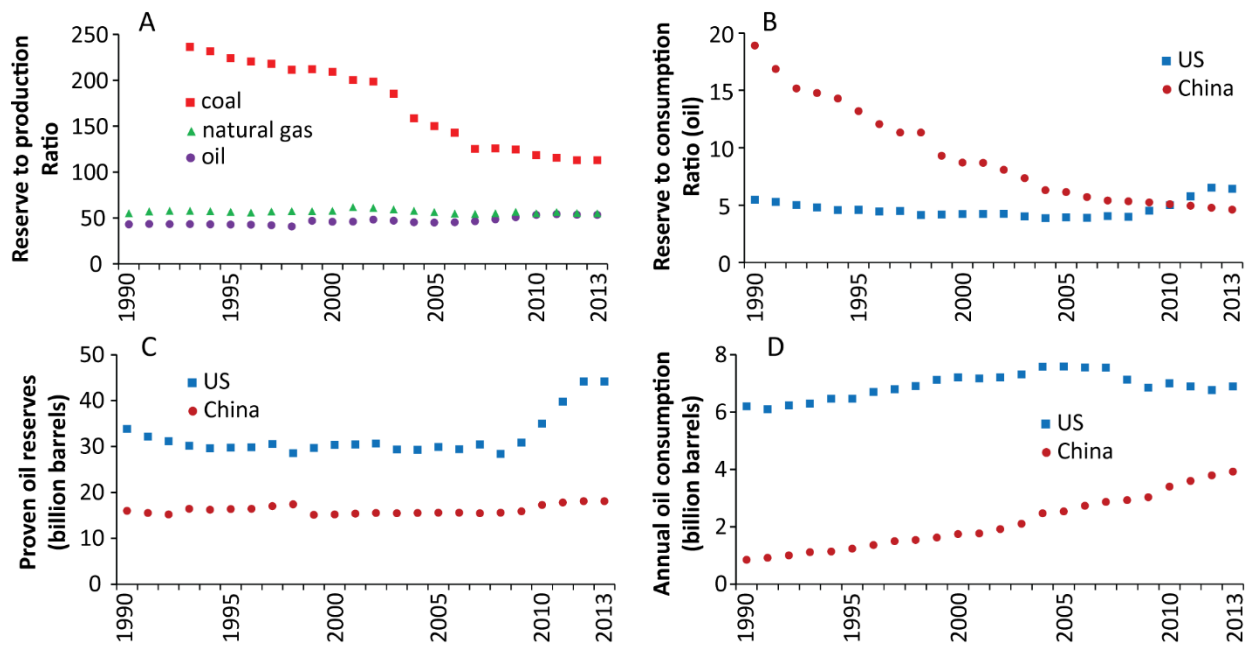
Figure 1.3. Finite reserves of fossil fuel resources. The world's ratios of proven reserve to production for fossil fuels are limited, especially for oil and natural gas (A). The world's largest two economies, the U.S. and China, have oil reserves that can only supply their consumption for fewer than 10 years as in 2013 (B). The recent increase in the U.S. proven oil reserves (C) is mainly due to technological advances in extracting tight oil (oil from low-permeability formations) [*8*]. China's oil consumption has been on a steady increase (D), which accelerates the decrease in the reserve-to-consumption ratio and poses a challenge on securing oil supply. Source: BP.

The geographic distribution of the world's fossil fuel reserves are not matched to individual country's consumption, resulting in issues on energy security and international geopolitics. For example, the oil reserves in the U.S. and in China can only sustain their current rate of consumption for another 5-6 years (**Fig. 1.3B**), which put pressures on these two largest economies to secure their oil supply in the global trade (**Fig. 1.4**). After the 2 oil crises in the 1970s, the share of oil imports to the United States from the Middle Eastern nations declined to 21% in 2013, while 45% of China's oil imports in 2013 were from the Middle Eastern nations to meet its rapid growth in oil consumption [*9*].

Responding to these challenges in environmental impacts, depleting fossil fuel reserves, and energy security, sustainable energy sources, such as solar and wind, have experienced phenomenal growth in deployment in the past decade. Between 2000 and 2013, renewables (non-hydro) has enjoyed an annual growth rate of 14% from 52 million toe (mtoe) to 280 mtoe, much faster than that for total energy consumption (2.4%). With continuing innovations for renewable technologies and a possible global commitment on mitigating greenhouse gas emissions, replacing fossil fuels with renewables will become increasingly feasible on the global scale both technically and economically.

4
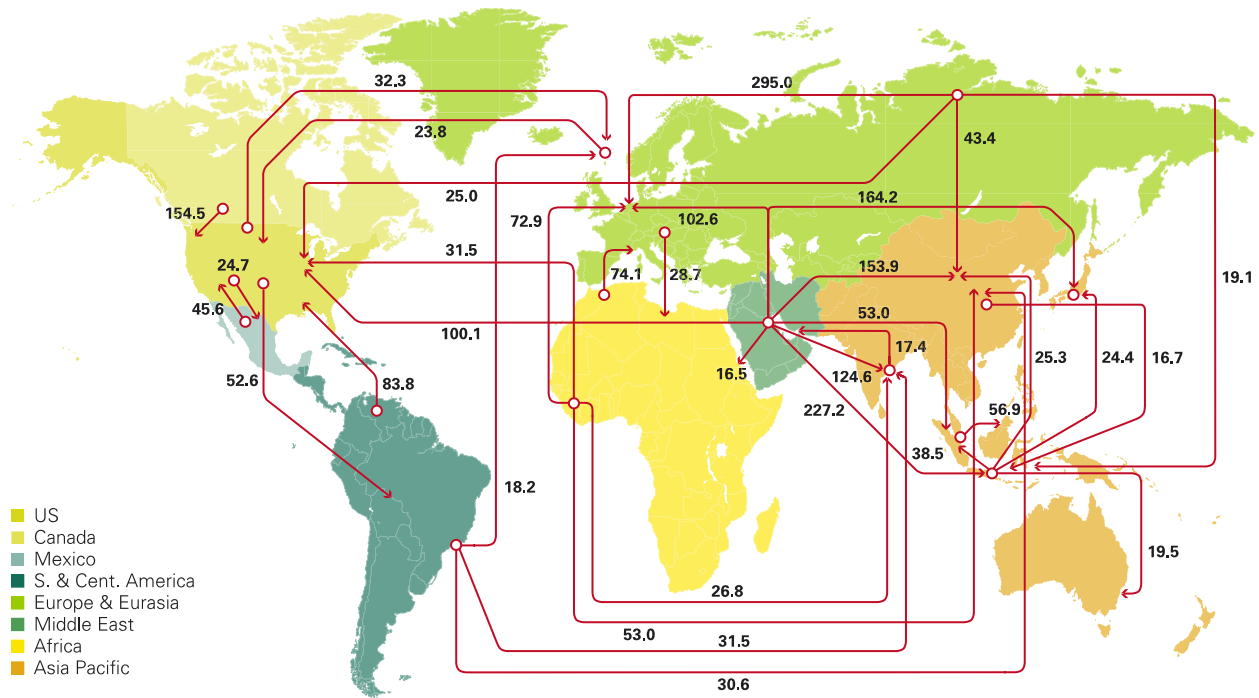
Figure 1.4. Trade flow and supply security of oil in 2013. The arrow indicates the export and import countries with the annual trade flow quantity in million tons. The imbalance between oil production and consumption causes large trade flows of oil across national boundaries, which pose potential energy security issues. Image courtesy: BP [*9*].
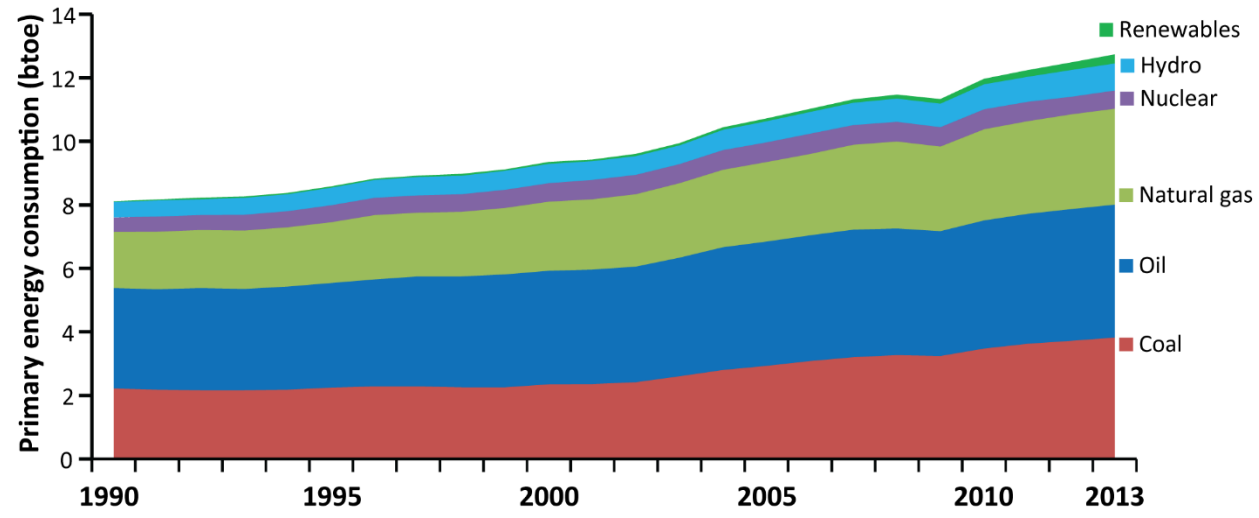
Figure 1.5. Rapid growth of renewables in the energy mix. More than 85% of the world's primary energy consumption has been from fossil fuel sources over the past two decades. The share of non-hydro renewable sources (renewables) in the total energy consumption has enjoyed a rapid growth in the last decade from 0.55% in 2000 to 2.2% in 2013, where the amount of renewables consumption has more than quadrupled or grown at an average annual growth rate of 14%. Source: BP.

1.2. Overview of this Dissertation

This dissertation examines the solar photovoltaic (PV) technology from a holistic and interdisciplinary perspective: from the basic research to improve PV efficiency, to innovations in manufacturing and installing PV modules, to deployment policies. Over the past decades, the accumulation of vast amount of effort across various disciplines in science, engineering, and policy has enabled the phenomenal growth of the PV industry into a global enterprise with about 140 GW of cumulative installations in 2013 [10].

Chapter 2 offers a fundamental understanding of the PV technology and a review on recent scientific advances on improving PV efficiency (W/m^2). The quantum physics of the 3 fundamental energy carriers in a PV device is first reviewed, which assists the description of the PV effect in terms of interactions among the photons, electrons, and phonons. The current-voltage (IV) characteristics of an ideal PV cell is then derived, which provides the framework in discussing strategies to improve PV efficiency. The last section reviews some major scientific advances in the area of optical management and optoelectronic conversion.

Chapter 3 reviews the state-of-the-art process flow in manufacturing commercial PV modules and introduces the thin silicon film PV concept for further cost-reduction ($/m^2). The major steps for manufacturing the crystalline-silicon (c-Si) wafer-based PV modules are outlined, together with those for manufacturing thin-film CdTe PV modules. In the context of pursuing further reduction in manufacturing cost, the thin Si film concept and its recent research effort are reviewed.

Chapter 4 presents the key findings of the laser crystallization experiment, which aims to explore novel ways to produce high-quality seed crystals for Si film deposition. The fundamental thermophysics of nucleation and crystal growth is first reviewed, which highlights the importance of temperature evolution and heat transport in modelling the ultrafast laser crystallization process. Laser crystallization of a range of Si nanostructures are then carried out to study the nucleation and crystal growth behavior under some novel conditions, such as suspended narrow Si membranes and Si nanoparticles confined on top of oxide nanostructures.

The cost of a PV module ($/W) is determined by both its rated efficiency in W/m^2 (**Ch. 2**) and its manufacturing cost in $/m^2 (**Ch. 3**). However, the same PV module with the same cost can lead to significantly different levelized cost of electricity (LCOE) in $/kWh, depending on the location and configuration of the installed PV system. Chapter 5 first provides an overview of the geographic distributions of solar resources and retail electricity rates, which yield a range of grid parity points across the world. Then, energy yield simulations for different PV panel tilt configurations are carried out using the angle-and-wavelength-resolved solar irradiance data, to examine the effect of angular and spectral variations in the solar spectrum on system performance.

Energy policies have been the driving forces for the phenomenal progress of the PV technology: the continuing reduction in cost and the rapid growth in deployment. Chapter 6 first reviews the major policy instruments for PV, and then discusses about a few policy lessons

from the rapid development of the global PV industry during 2000-2013. Concerned with the mounting fiscal pressure from deployment incentives and focused on further cost reductions, an innovation-focused policy framework is proposed to revive the PV manufacturing sector and to pursue an innovation-driven global PV industry moving forward.

2. Innovation in Photovoltaic Science

2.1. The Quantum Picture of the 3 Fundamental Energy Carriers

In a photovoltaic cell, energy is primarily converted among light, electrons, and heat. According to the quantum mechanics description, these different forms of energy are carried by photons, electrons, and phonons, respectively. Each of these fundamental energy carriers occupies discrete energy levels according to the statistics of either fermions or bosons. Knowing the density of energy states and the occupation statistics, number density of energy carriers as well as energy density can be derived [11]. As illustrations, free electron density in semiconductors and the blackbody radiation law will be deduced from these first principles in this section.

2.1.1. Comparing photons, electrons, and phonons

The number of energy states from the wavevector picture (K-space) is uniform among all 3 energy carriers (**Eq. 2.1**), where each unit cell of a quantized energy state is $\left(\frac{2\pi}{L}\right)^3$. According to quantum mechanics, the wavevectors can only take on discrete values. One of the most famous example is a particle inside a 1D infinite potential well [12]. For a 3D system with length L in each dimension, periodic boundary conditions lead to the discrete values, where wavevectors, K_x, K_y, and K_z, can only be multiples of $\frac{2\pi}{L}$.

$$D(K)dK = \frac{4\pi K^2 dK}{(2\pi/L)^3} \qquad \textbf{Equation 2.1}$$

The first difference among the 3 energy carriers arises from the dispersion relations (**Eqs. 2.2-2.4**), which relates the energy/frequency of each energy carrier E/ω with its wavevector K. The density of states as a function of energy/frequency (**Eqs. 2.6-2.8**) can be obtained according to **Eq. 2.5**.

$$E = \hbar\omega = \hbar c K \quad \text{for photons} \qquad \textbf{Equation 2.2}$$

$$E - E_c = \hbar\omega = \frac{\hbar^2 K^2}{2m^*} \quad \text{for electrons} \qquad \textbf{Equation 2.3}$$

$$\omega = v_s K \quad \text{for low temperature phonons in the Debye model} \qquad \textbf{Equation 2.4}$$

$$D(\omega) = D(K)/\frac{\partial\omega}{\partial K} \qquad \textbf{Equation 2.5}$$

$$\frac{D(\omega)}{L^3} = \frac{\omega^2}{2\pi^2 c^3} \quad \text{for photons} \qquad \textbf{Equation 2.6}$$

$$\frac{D(E)}{L^3} = \frac{1}{4\pi^2}\left(\frac{2m^*}{\hbar^2}\right)^{\frac{3}{2}}(E-E_c)^{\frac{1}{2}} \quad \text{for electrons} \qquad\qquad \textbf{Equation 2.7}$$

$$\frac{D(\omega)}{L^3} = \frac{\omega^2}{2\pi^2 v_s^3} \quad \text{for phonons} \qquad\qquad \textbf{Equation 2.8}$$

The second major difference is their occupation statistics. Photons and phonons are bosons, where an arbitrary number of bosons can occupy the same energy state, and populate different energy states according to the Bose-Einstein statistics f_{BE} (**Eq. 2.9**), which is derived from the canonical ensemble. Electrons are fermions, and each energy state in **Eq. 2.1** can be occupied by a maximum of two electrons, that are of the opposite spins. Electrons populate different energy states following the Fermi-Dirac statistics f_{FD} (**Eq. 2.10**), which is derived from the grand canonical ensemble of chemical potential μ, where the total number of electrons is also conserved.

$$f_{BE} = \frac{1}{\exp\left(\frac{\hbar\omega}{k_B T}\right)-1} \qquad\qquad \textbf{Equation 2.9}$$

$$f_{FD} = \frac{1}{\exp\left(\frac{\hbar\omega-\mu}{k_B T}\right)+1} \qquad\qquad \textbf{Equation 2.10}$$

The third difference is the polarizations available for each energy state. For each energy state, photons have 2 transverse modes, electrons have 2 spins, and phonons have 2 transverse modes as well as 1 longitudinal mode.

2.1.2. Free carrier density in semiconductors and blackbody radiation

In a semiconductor, the number density of electrons in the conduction band ($E \geq E_c$) is strongly influenced by the Fermi level and temperature (**Eq. 2.11**), where the Fermi-Dirac statistics is approximated by the Boltzmann statistics (**Eq. 2.12**). In the classical limit, the electrons in the conduction normally satisfies $E - E_F \gg k_B T$.

$$n = \int_{E_c}^{\infty} 2\frac{D(E)}{L^3}f_{FD}(E,E_F,T)dE = N_c \exp\left(-\frac{E_c-E_F}{k_B T}\right) \qquad\qquad \textbf{Equation 2.11}$$

$$f_{FD} = \frac{1}{\exp\left(\frac{E-E_F}{k_B T}\right)+1} \approx \exp\left(-\frac{E-E_F}{k_B T}\right) \qquad\qquad \textbf{Equation 2.12}$$

The Planck blackbody radiation law can be readily derived from the energy density of photons in free space (**Eqs. 2.13&2.14**). Note that the Wien's displacement law for the wavelength at maximum intensity has two versions (**Eqs. 2.15&2.16**), depending on measuring in energy or wavelength (**Fig. 2.2**).

Photons   **Electrons**   **Phonons**

Discrete values in k-space

$$D(K)dK = \frac{4\pi K^2 dK}{(2\pi/L)^3}$$

K_y $2\pi/L$ $\updownarrow 2\pi/L$ K_x

Dispersion relations

ω C_0 K

E E_c K

ω V_s K

DOS (excl. polarizations)

$$g(\omega) = \frac{D(\omega)}{L^3} = \frac{\omega^2}{2\pi^2 c^3}$$

$$g(E) = \frac{1}{4\pi^2}\left(\frac{2m^*}{\hbar^2}\right)^{\frac{3}{2}} (E - E_c)^{\frac{1}{2}}$$

$$g(\omega) = \frac{\omega^2}{2\pi^2 v_s^3}$$

Statistical distributions

Bose-Einstein (bosons)   Fermi-Dirac (fermions)   Bose-Einstein (bosons)

5.0 $f_{BE} = \dfrac{1}{\exp\left(\frac{\hbar\omega}{k_B T}\right)-1}$ 1.0   0.1

1.0   0.7   1.4   Energy (k_BT)

$f_{FD} = \dfrac{1}{\exp\left(\frac{\hbar\omega - \mu}{k_B T}\right)+1}$ 0.5 μ Energy (k_BT)

tail approximation $f_B = \exp\left(-\frac{\hbar\omega}{k_B T}\right)$ 2.5   10   Energy (k_BT)

Polarizations   2 T   2 Spins   2 T + 1 L

Energy storage   Wave Amplitude ↑ $E_1 \rightarrow E_2$ Wave Amplitude ↑

Energy density $\int_0^\infty 2 \cdot g(\omega) \cdot f_{BE} \cdot \hbar\omega \, d\omega$ $\int_{E_c}^\infty 2 \cdot g(E) \cdot f_{FD} \cdot E \, dE$ $\int_0^{\omega_D} 3 \cdot g(\omega) \cdot f_{BE} \cdot \hbar\omega \, d\omega$

Figure 2.1. Comparison between photons, electrons, and phonons in the quantum mechanics picture.

Figure 2.1 highlights the similarities and differences among the 3 fundamental energy carriers. These basic understandings allow us, in the next section, to describe key processes in the photovoltaic cell as energy exchanges among these "particles".

$$I_\omega = \frac{cu_\omega}{4\pi} = 2\frac{D(\omega)}{L^3} f_{BE} \, \hbar\omega = \frac{\hbar\omega^3}{4\pi^3 c^2} \frac{1}{\exp(\hbar\omega/k_B T)-1}$$ **Equation 2.13**

$$I_\lambda = I_\omega \left|\frac{\partial\omega}{\partial\lambda}\right| = \frac{\hbar\omega^3}{4\pi^3 c^2} \frac{1}{\exp(\hbar\omega/k_B T)-1} \cdot \frac{2\pi c}{\lambda^2} = \frac{2hc^2}{\lambda^5} \frac{1}{\exp(hc/\lambda k_B T)-1}$$ **Equation 2.14**

$$\frac{T}{E_{max}} = 4127\frac{K}{eV} \, \hbar\omega$$ **Equation 2.15**

$$\lambda_{max} T = 2.898 \cdot 10^6 \, \text{nm.K}$$ **Equation 2.16**
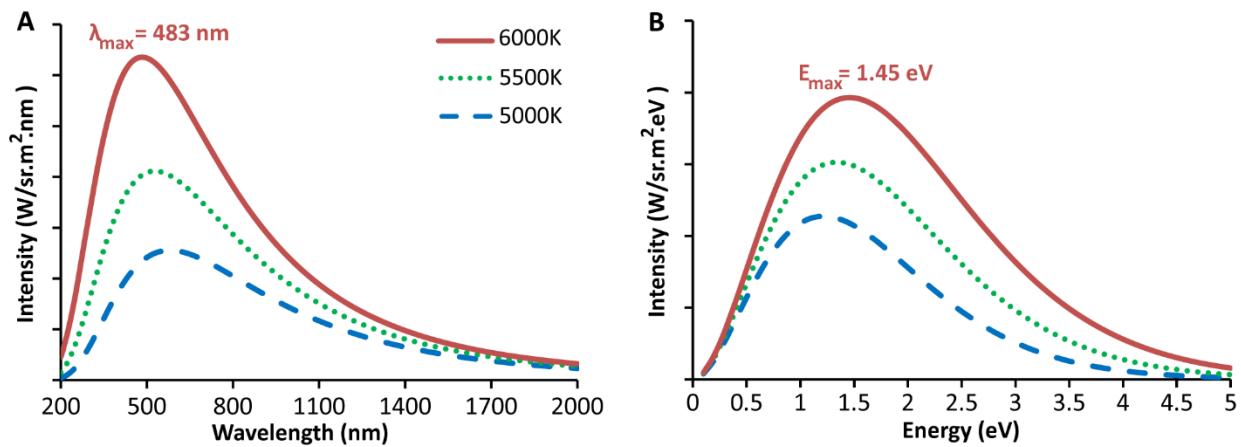
Figure 2.2. Planck's blackbody law expressed in terms of wavelength and energy. Changing the unit of measurement from the conventional wavelength (A) to energy (B) causes the position of maximum intensity to be red-shifted.

2.2. Photovoltaic Effect

Photovoltaic technology is essentially about converting sunlight (photons) to electric current (drifting electrons) in a circuit. In a quick overview, the photons need to first enter the semiconductor absorber, after reflection and absorption from other layers preceding the absorber layer. Subsequently, some of the above-bandgap photons are absorbed by the semiconductor and excite electrons from the valence band (creating a hole) to the conduction band, creating electron-hole pairs (EHPs). Typically, the commercial PV cell is made of a PN junction, which separates the EHPs towards opposite electrodes. The charge carriers are finally collected at the electrodes, which can produce a photocurrent at short-circuit condition, an open-circuit voltage at open-circuit condition, or a current (smaller than photocurrent) at a working voltage (smaller than open-circuit voltage).

2.2.1. Dark current in a PN junction

Using Si PN junction PV cell as the example, PN junction is formed when n-type Si (typically doped with phosphorous atoms and with electrons as the majority charge carriers) and p-type Si (typically doped with boron atoms and with holes as the majority charge carriers) are in contact, where the Fermi level in n-Si, E_{Fn}, and that in p-Si, E_{Fp}, reach equilibrium. At room temperature, the number density (concentration) of majority charge carriers are mostly controlled by the dopant concentrations (**Eqs. 2.17&2.18**).

$$n \approx N_d$$

Equation 2.17

$$p \approx N_a$$

Equation 2.18

The majority carrier concentrations in n-Si and p-Si also follows **Eq. 2.19** and **Eq. 2.20**, respectively. In the derivation, the Fermi-Dirac statistics is approximated to Boltzmann statistics (**Eq. 2.21**). The free carrier concentration of intrinsic Si follows **Eq. 2.22**, which is also called the Mass Action Law.

$$n = \int_{E_c}^{\infty} g_c(E) f_0(E,T) dE = N_c \exp\left(-\frac{E_c - E_{Fn}}{k_B T}\right)$$

Equation 2.19

$$p = \int_{-\infty}^{E_v} g_v(E)(1 - f_0(E,T)) dE = N_v \exp\left(-\frac{E_{Fp} - E_v}{k_B T}\right)$$

Equation 2.20

$$f_0(E,T) = \frac{1}{\exp\left(\frac{(E - E_F)}{k_B T}\right) + 1} \approx \exp\left(-\frac{E - E_F}{k_B T}\right) \text{ for } E \gg E_F$$

Equation 2.21

$$np = N_c N_v \exp\left(-\frac{E_c - E_v}{k_B T}\right) = N_c N_v \exp\left(-\frac{E_g}{k_B T}\right) = n_i^2 \text{ for } E_{Fn} = E_{Fp}$$

Equation 2.22

For a PV cell working at zero applied bias ($V = 0$) (**Fig. 2.3**), the built-in voltage V_{Bi} is related to the doping level in n-Si (p-Si), N_d (N_a), as **Eq. 2.23**. The electric field from the built-in voltage V_{Bi} in the depletion region is the primary mechanism separate the charge carriers towards opposite electrodes. The current comprises 3 components [13]: the diffusion current of electrons from the n-side to the p-side, overcoming a potential barrier of $V_{Bi} - V$ (**Eq. 2.24**); the diffusion current of holes from the p-side to the n-side, overcoming a potential barrier of $V_{Bi} - V$ (**Eq. 2.25**); the drifting current near the PN junction of the EHPs being separated by the built-in electric field. The drift current, which is assumed to remains the same under forward bias, can be obtained from the condition that net current is zero under zero bias (**Eq. 2.26**). Finally, the IV characteristic curve for the dark current can be derived as **Eq. 2.27**.

$$qV_{Bi} = k_B T\left(\ln\left(N_c/n_0^p\right) - \ln(N_c/N_d)\right) = k_B T \ln\left(\frac{N_d N_a}{n_i^2}\right)$$

Equation 2.23
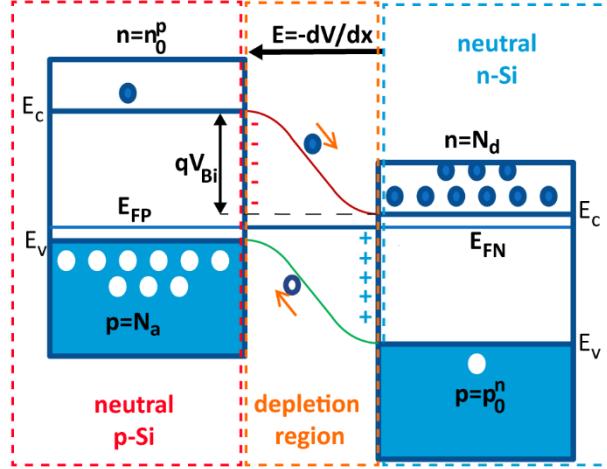
Figure 2.3. Band diagram of PN junction PV cell operating at zero applied bias. Near the contact between n-Si and p-Si, there is net diffusion of electrons from n-Si to p-Si and holes from p-Si to n-Si, due to concentration differences, until the electric field built up in this region can counter the diffusion current with a drifting current. This region near the contact is the primary mechanism for separating charge carriers in a PV cell, and is commonly referred as the depletion region.

$$J_n(V) = B_n \exp\left(-q\frac{V_{Bi}-V}{k_B T}\right)$$ **Equation 2.24**

$$J_p(V) = B_p \exp\left(-q\frac{V_{Bi}-V}{k_B T}\right)$$ **Equation 2.25**

$$J_{diff}(V=0) + J_{drift} = 0 = \left(B_n + B_p\right)\exp\left(-q\frac{V_{Bi}}{k_B T}\right) + J_{drift}$$ **Equation 2.26**

$$J_d = \left(B_n + B_p\right)\left[\exp\left(-q\frac{V_{Bi}-V}{k_B T}\right) - \exp\left(-q\frac{V_{Bi}}{k_B T}\right)\right] = J_{diff}(V=0)\left[\exp\left(q\frac{V}{k_B T}\right) - 1\right]$$

Equation 2.27

2.2.2. IV characteristics of a photovoltaic cell under illumination

Under illumination, EHPs are excited by above-bandgap photons, where a photocurrent I_{ph} is produced mainly by drifting of charge carriers (electrons and holes) under the built-in electric field, in opposite direction of the diffusion current. The EHPs generated from three regions of a PV cell are most likely to contribute to the photocurrent (**Fig. 2.3**). In the depletion region, the electrons (holes) tend to drift towards the neutral n-Si (p-Si) under the built-in electric field. Within the diffusion length of minority carriers (holes) to the depletion region in the neutral n-Si region, holes can diffuse from the neutral n-Si region to the depletion region, and then drift to the neutral p-Si region under built-in electric field. Similarly, within the diffusion length of minority carriers (electrons) to the depletion region in the neutral p-Si region, electrons can diffuse into the depletion region, and then drift to the neutral n-Si region of the PV cell [14].

The PV cell under illumination can be modeled an electric circuit with a current source (the photocurrent), a diode (the diffusion current), possible shunt paths, and series resistance (**Fig. 2.4A**), with the I-V characteristics as in **Eqs. 2.28&2.29**. The ideal PV cell has zero series resistance R_s and infinite shunt resistance R_p, with simplified I-V characteristics (**Eq. 2.30**). The ideal I-V curve graphically matches the $I_{sc} \cdot V_{oc}$ square the best, and results in the highest fill factor (FF). FF is the ratio between the maximum deliverable power and the product of I_{sc} and V_{oc} (**Eq. 2.31**). However, the real PV cell has inevitable series resistance, which decrease the steepness of the IV curve around the open-circuit voltage point and results in a lower FF. If shunt paths are present in the PV cell, the short-circuit current will suffer as some portion of the photo-generated charge carriers will flow through these paths rather than across the external load.
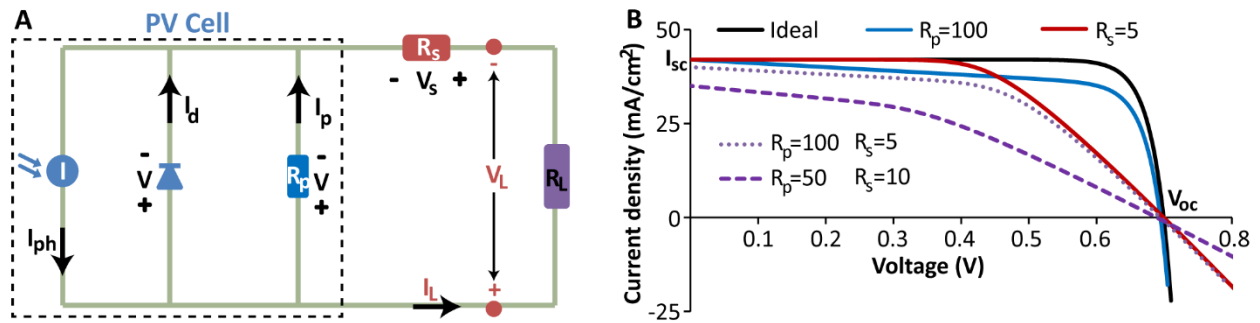
Figure 2.4. The effect of series resistance and shunt resistance on the IV characteristics of a PV cell. The photovoltaic cell can be modeled as a package (A) of a current source (I_{ph}) and a diode (I_d), with possible shunt paths (R_p). The series resistance (R_p) represents the electrical resistance both in the cell and at the contact. The I-V curve (B) plots the possible combinations of current (I_L) and voltage (V_L) that can be delivered to the load (R_L). Increasing series resistance changes the slope around the open-circuit voltage (V_{oc}) point to less ideal, while decreasing shunt resistance changes both the slope and current values around the short-circuit (I_{sc}) point to less ideal.

$$I_L = I_{ph} - I_0 \left(\exp\left(\frac{qV}{k_B T} \right) - 1 \right) - \frac{V}{R_p}$$

Equation 2.28

$$V_L = V - I_L R_s$$

Equation 2.29

$$I_L = I_{ph} - I_0 \left(\exp\left(\frac{qV}{k_B T} \right) - 1 \right)$$

Equation 2.30

$$FF = \frac{P_m}{V_{oc} I_{sc}}$$

Equation 2.31

2.3. Innovations Towards and Beyond the Efficiency Limits

The groundbreaking result of the first Si PN junction solar cell with 6% efficiency was published by researchers from Bell Labs in 1954 [15]. From then on, series of innovations have been made in laboratory to reduce efficiency losses from reflection, surface recombination,

carrier mobility, bulk resistance, and contact resistance. The cell efficiency is almost doubled from about 14% in 1977 to 24% in 1995 [16]. Only very recently in 2014, SunPower Corporation, one of the largest PV manufacturers in the United States, demonstrated a large-area PV cell with a slightly improved efficiency of 25.0%. As the record efficiencies of laboratory cells are approaching the theoretical efficiency limits, further efficiency gains could become even more difficult, and marginally significant in terms of cost-effectiveness.
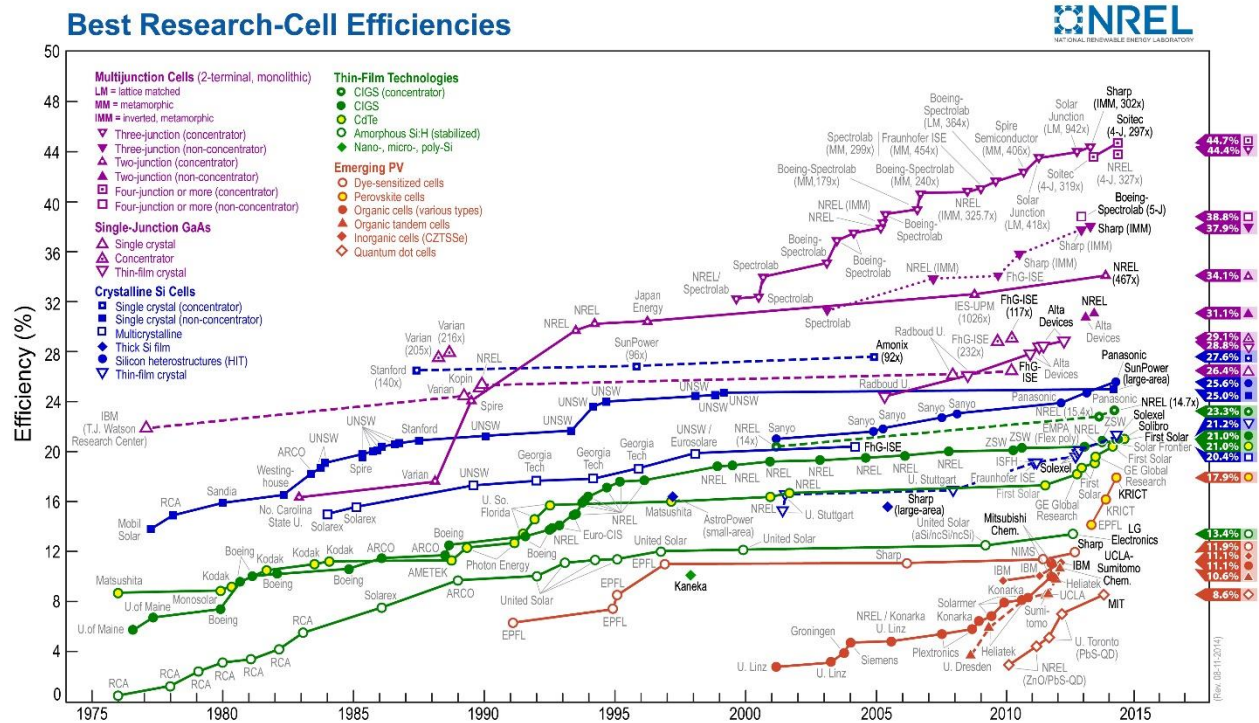
Figure 2.5. Research solar cell efficiency record. The latest record efficiency of PV cells, based on single-crystalline Si wafers, has evolved to 25.0% ad developed by SunPower Corporation in 2014. Source: NREL: [17].

The Carnot efficiency limit, from the second thermodynamics law, dictates a maximum theoretical efficiency of about 95% in converting solar energy into useful work, assuming 6000 K and 300 K for the temperature of sun and earth, respectively.

For the efficiency of a single junction PV cell, the guiding theoretical upper limit has been the Shockley-Queisser efficiency limit proposed in 1961, which is based on the detailed balance of blackbody radiation from the sun at 6000 K. The PV cell is assumed to be a perfect absorber, and each above-bandgap photon could lead to collection of one EHP. With these assumptions, the maximum efficiency is about 30% for a semiconductor with a bandgap of 1.1 eV [18], or 20% above the current best efficiency for c-Si PV cell (25.0%). There have been constant efforts for scientific research to improve the efficiency towards and even beyond the Shockley-Queisser efficiency limit.

15

2.3.1. Optical management

Not all of the incident photons can participate in the optoelectronic conversion, as some are first reflected away at the interfaces between the air and the semiconductor absorber and some entering photons lack the adequate light path to be absorbed by the absorber. These "optical" losses can be reduced by engineering the solar cell with antireflection and light trapping schemes. Recent studies have found nanostructures such as array of nanocones or nanowires demonstrating promising potentials for both antireflection and light trapping capabilities.

Early attempts to reduce surface reflection are focused on anti-reflective coating (ARC) [19], which is based on the destructive interference from quarter-wave thin films. High-efficiency Si PV cells in the 1980s from the University of New South Wales and the Stanford University utilized either single-layer or double-layer ARCs for good optical management [20]. To achieve broadband and omnidirectional antireflection properties, which is important for solar PV applications, an active research topic in recent years has been nanostructured thin films with graded refractive index, ranging from nanorods [21-24], nanocones [25,26], nanotips [27], nanodomes [28], to porous [29,30] or textured [31] "black silicon".

Light absorption in silicon is weak for visible light and especially for near the bandgap infrared spectrum. Therefore, various light trapping schemes are explored to increase the light path and enhance absorption in a thin layer of silicon [26,32], such as nanowire arrays [33-36], plasmonics [37,38], and photonic crystals [39-41]. Early innovations such as surface texturing [42-44] has been a common feature in today's commercial PV cells, as discussed in Chapter 3.

2.3.2. Optoelectronic conversion

As described in section 2.1, the bandgap of a single-junction PV cell needs to strike a balance between high open-circuit voltage and large short-circuit current (good optical absorption). When a photon above the bandgap of the semiconductor materials is absorbed, only one electron-hole pair or exciton is usually produced. The excess photon energy, the difference between the incident photon's energy and the absorber's bandgap, becomes heat, or phonons, in the system through thermalization of charge carriers (electrons and holes), which lowers the theoretical efficiency limits of PV cells.

Multiple exciton generation (MEG) raises the theoretical photovoltaic efficiency limit of PV cells, by generating multiple electron-hole pairs from one photon. For example, the initially excited hot charge carrier (electron, or hole) by a high-energy photon could excite another electron-hole pair while relaxing towards the band edges through impact ionization, which competes with intraband carrier relaxation through emissions of optical phonons. The MEG efficiency of PbSe and PbS in bulk (single-crystalline films of about 1 μm in thickness) has been studied both experimentally and theoretically [45]. MEG efficiency is typically measured by time-resolved spectroscopy techniques [46], and it has also been studied in other

nanostructures such as PbS quantum dots [47], PbSe quantum dots [48,49], and single-wall carbon nanotubes with axial pn junction [50].

An alternative approach to reduce the thermalization loss could be to extract these photogenerated hot charge carriers [51-53] before they relax to the band edges, through selective energy contacts [54,55].

Sub-bandgap low-energy photons in the solar spectrum normally do not generate charge carriers, which lowers the theoretical ratio of photocurrent to incident photons. One approach to reduce these "red" losses would be utilizing intermediate-band PV cells [56,57], where two sub-bandgap photons can collectively generate one electron-hole pair, by exciting the electron from the valence band to the conduction band through an intermediate energy band within the otherwise forbidden bandgap. The maximum efficiency of such intermediate-band PV cells can reach 63% at the bandgap of 1.95 eV, which is split by the intermediate energy band into two subbands of 0.71 eV and 1.24 eV [56,58].

By optimizing separately on the short-circuit current and the open-circuit voltage, multijunction PV cells with absorbers of different bandgaps can raise the efficiency limit [59]. The efficiency limit for multijunction PV cells can increase from 50%, 56% to 72% at 1000 suns concentration for 2 bandgaps, 3 bandgaps to 36 bandgaps, respectively [60]. As these high-efficiency PV cells are costly to manufacture, they are typically used in concentrator PV (CPV) systems. For example, a tandem PV cell [61] with InGaP top cell (with a bandgap of 1.9 eV) and GaAs bottom cell (with a bandgap of 1.43 eV) has attained 30.3% efficiency under the AM1.5G spectrum [62]. Recently, a 8.6% efficient polymer tandem PV cell have also been demonstrated with a new low-bandgap (1.44 eV) conjugated polymer [63]. Triple-junction PV cells with over 40% efficiency, utilizing three bandgaps, have also been fabricated by Spectrolab Inc. measured at 1 sun [64], by NREL at 326 suns' concentration [65], and by Fraunhofer ISE at 454 suns' concentration [66].

Another approach to fully utilizing the solar spectrum could be the spectrum splitting concept [67,68], where different portions of the solar spectrum are split and irradiated on different absorbers of matched bandgaps [69-72].

3. Manufacturing Innovation for More Affordable Photovoltaic Modules

3.1. Manufacturing Solar PV Modules

The global solar PV industry has reached 38 GW of installation in 2013 [10], or an annual market size on the order of 100 billion U.S. dollars. Majority of these solar PV modules are based on the c-Si wafer technology. A typical c-Si PV cell in commercial manufacturing has key features as highlighted in **Fig. 3.1**.
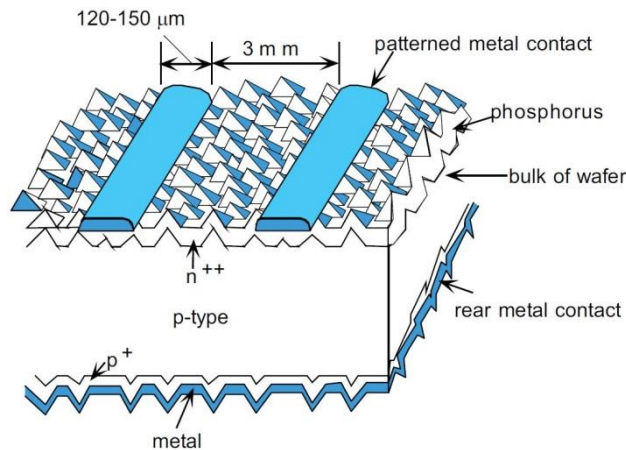
Figure 3.1. Standard PV cell based on c-Si wafers. The key features of a commercial PV cell include the surface texturing and antireflection layer for light trapping and reduced surface reflection, and screen-printing of metal line front contact. Image courtesy: UNSW [73].

The process flow (**Fig. 3.2**) for commercially manufacturing these c-Si PV modules [74,75] starts with cleaning, etching and rinsing wafers in wet baths, from which the pyramid-texturing proves to enhance light absorption. The n^+ emitter layer is then formed by doping the cleaned p-type wafers by phosphorous diffusion in furnace near 900 ^{0}C, after which edge isolation is necessary to prevent shunt paths between the front and back contacts through these n^+ layers on the wafer edges. Phosphorus silicate glass (PSG), the by-product from furnace doping with phosphorus oxide trichloride (POCl$_3$), is typically cleaned off by wet etching [76]. To reduce surface recombination and improve the optical performance, a passivation and anti-reflection layer is coated on top of the furnace doped n^+ emitter layer. The last few steps in manufacturing PV cells involve screen-printing narrow (large height/width ratio) silver lines as the front contact [77] and printing the aluminum back contact, which are then fired in furnace to improve electrical contact.

To assemble the PV cells into modules, PV cells' efficiency needs to be individually tested and binned, so that each PV module is made of PV cells of close efficiencies. The stringed PV cells are then laminated with encapsulant and sandwiched between glasses for protection against environment.

Manufacture the PV cells: A-F
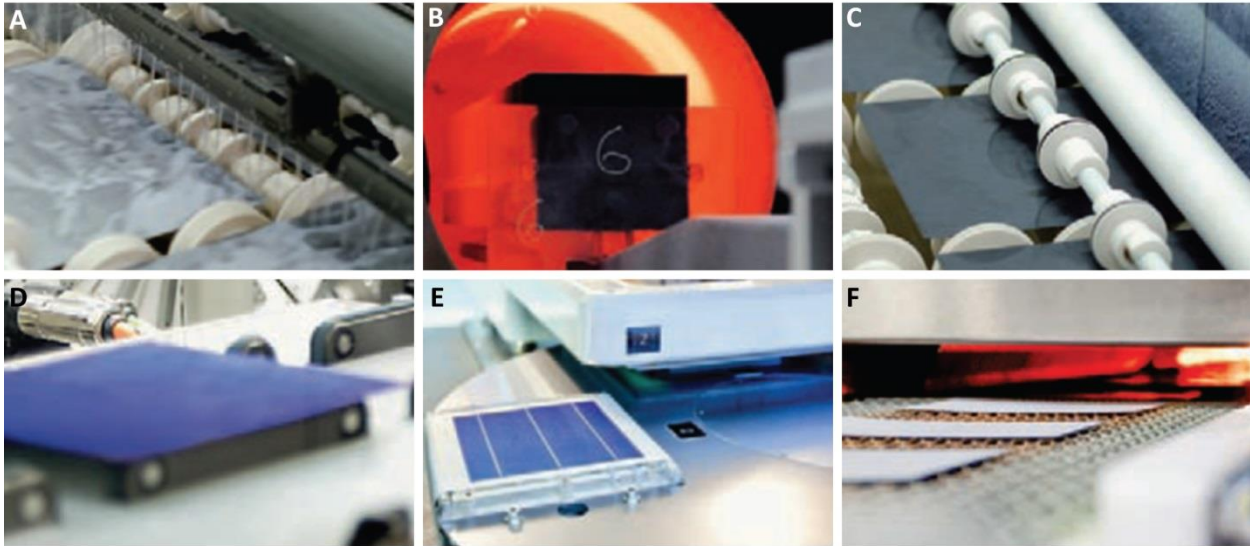
Assemble the cells into modules: G-I

Figure 3.2. Process flow of making c-Si PV modules. The images in A-I are representative for key steps in the process flow: surface texturing (A), furnace doping (B), edge isolation and PSG removal (C), passivation and anti-reflection coating (D), screen printing (E), contact firing (F), testing and binning (G), stringing cells (H), and lamination (I). Image courtesy: Q-Cells [74] and Suntech [75].

Besides the mainstream PV modules made from c-Si wafers, thin-film PV modules, championed by First Solar Inc's CdTe technology, are another category of commercially available PV modules at the GW scale. 15.8% efficient CdTe PV cells were demonstrated in 1993 [78]. Since then series of innovations have been made to improve the efficiency [79,80] and reduce the manufacturing cost [81]. To date, the highest efficiency for CdTe PV cells is 21.0%, set by First Solar in Aug 2014 [82]. First Solar also holds the record efficiency for CdTe PV modules at 17.5% [83].

The manufacturing process flow (**Fig. 3.3**) of First Solar's CdTe PV modules [84,85] starts with depositing the n-type CdS (n-CdS) window layer and the p-type CdTe (p-CdTe) absorber layer on the superstrate glass, which is typically pre-coated with TCO (SnO_2 in the First Solar's process) by the glass supplier. Laser scribing [86] is then applied to ablate across the CdTe, CdS, and TCO layers (P1) to define individual PV cells, and the laser-scribed openings are subsequently filled by photoresist plug. The second laser scribing is applied to create a via across the CdTe and CdS (P2) to interconnect PV cells in series, where electrical contact is made between the TCO and the metal back contact. The third laser scribing is applied through the

19

metal back contact layer (P3) to define individual PV cells. The monolithically integrated PV module is then encapsulated with ethyl vinyl acetate (EVA) and covered by the substrate glass.
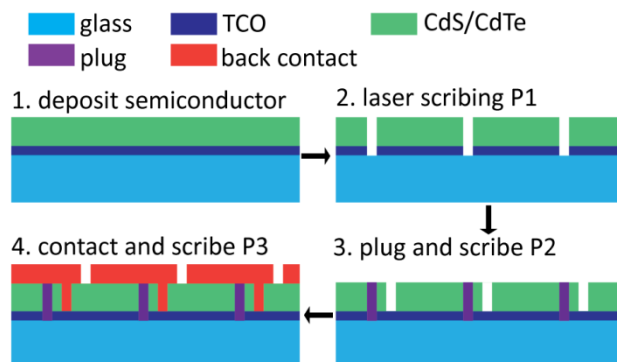
Figure 3.3. Process flow of First Solar's CdTe PV modules. The semiconductor layers (n-CdS and p-CdTe) are deposited on the TCO-coated glass by vapor transport for high throughput. Laser scribing is used to define the individual cells (P1 & P3) and create interconnects (P2). Plug is a filling with insulating materials to prevent shunting between the TCO and back contact.

3.2. Towards TW-Scale Global PV Deployment
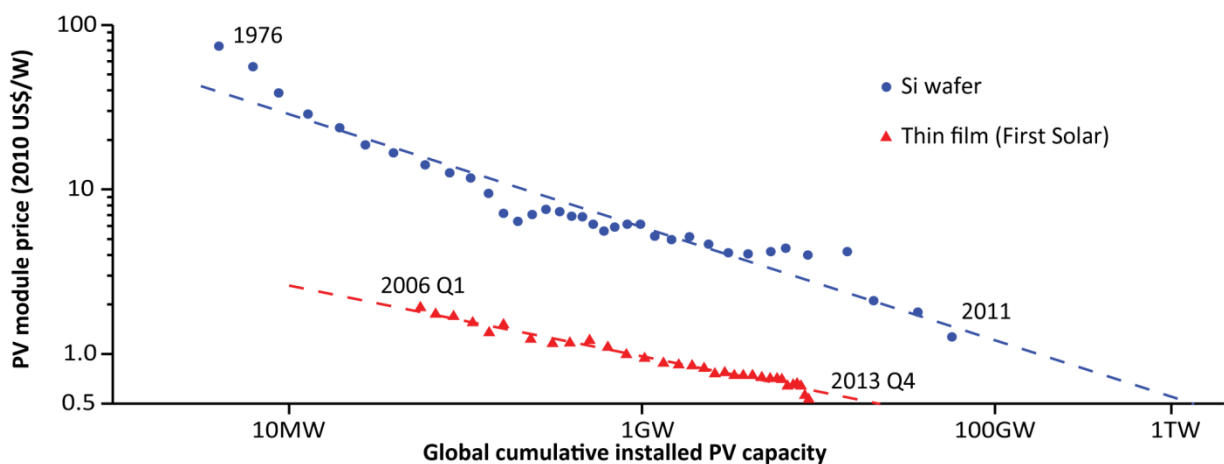
Figure 3.4. Learning curves of c-Si wafer PV modules and CdTe thin-film PV modules. All prices are inflation-adjusted to the 2010 U.S. dollars. Source: BNEF and First Solar.

The price of c-Si wafer PV modules has climbed down the learning curve (**Fig. 3.4**) steadily over the past few decades at a learning rate of 21.1%, or the module price decreases by 21.1% per doubling in cumulative installed capacity. Since 2006, the cost of First Solar's CdTe thin-film has enjoyed a learning rate of 13.8%, decreasing from $1.92/W in the first quarter (Q1) of 2006 to $0.53/W in the fourth quarter (Q4) of 2013. Aiming to reach "grid parity" [*87*], the United States has established the SunShot goal and an entire federal office within the Department of

20

Energy, to reduce the PV system cost to $1/watt (approximately $0.05/kWh for the levelized cost of PV electricity and $0.5/W for the PV module) by 2020 [88] that is aiming to make PV electricity cost-competitive with grid electricity rates across the United States.

To meet the long-term greenhouse gas (GHG) mitigation targets of 80% reductions from the 1990 baseline by 2050, solar energy can play a key role in decarbonizing electricity generation [89,90]. Solar PV technology with terawatt (TW)-scale deployment has long been recognized as an effective tool to mitigate climate change [91-93]. The cost of both c-Si PV and CdTe thin-film PV modules has to decline further to reach the SunShot goal of a sustainable selling price at $0.5/W for PV modules, so that PV technology becomes fully competitive with fossil fuel electricity generation in the United States without subsidies and more likely to be deployed in developing nations.

Sustainable materials supply for the TW-scale PV deployment could be a long-term challenge for Tellurium used in CdTe thin-film PV modules [94-98]. Notably in April 2013, First Solar acquired a Silicon Valley startup TetraSun for its promising c-Si PV technology [99], to expand or diversity into the silicon-based PV technologies [100]. Therefore, research and innovation in further reducing the cost of c-Si PV technology are of commercial importance for the TW-scale global PV deployment. In this context, the concept of thin silicon film PV cells, with only 1% of the silicon usage in the conventional c-Si wafer PV technology, is recognized as a promising and high-value research topic for further cost reduction and improved energy payback period.

3.3. The Concept of Thin Silicon Film PV Cells

3.3.1. Optical absorption in thin silicon film

Using less light absorber materials (c-Si) is one strategy to both further reduce cost of the photovoltaic (PV) cells and improve the energy payback period as c-Si is energy intensive to produce. Moreover, thin film PV cells can be manufactured on flexible substrates and open up new energy applications.

For thin film as the light absorber, the materials thickness needs to be optimized to balance the efficiency in optical absorption and materials usage. **Fig. 3.5** highlights the optical performance for c-Si film with a range of thickness under AM1.5G solar spectrum, and the underlying models for accounting the generated photocurrent is according to **Eqs 3.1 to 3.3**.

The spectral photocurrent I_λ for a given wavelength λ is a function of the spectral AM1.5G solar spectrum $I_{\lambda 0}$, the spectral absorption coefficient of c-Si α_λ, and the film thickness L, following the Beer's law:

$$I_\lambda = I_{\lambda 0}[1 - \exp(-\alpha_\lambda L)]$$ <div align="right">**Equation 3.1**</div>

The spectral photocurrent under the $4n^2$ limit or the Yablonovitch limit [101-103] also incorporates the light path enhancement using refraction index n_λ:

$$I_\lambda = \mathrm{I}_{\lambda 0}\big[1 - \exp\big(-\alpha_\lambda L \cdot 4n_\lambda^2\big)\big] \qquad\qquad \textbf{Equation 3.2}$$

The total generated photocurrent is obtained from integrating the spectral photocurrent with wavelength from 280 nm (the shortest wavelength in AM1.5G solar spectrum data) to 1100 nm (the near-bandgap wavelength for c-Si):

$$I_{p\mathrm{h}} = \int_{280}^{1100} I_\lambda \, d\lambda \qquad\qquad \textbf{Equation 3.3}$$
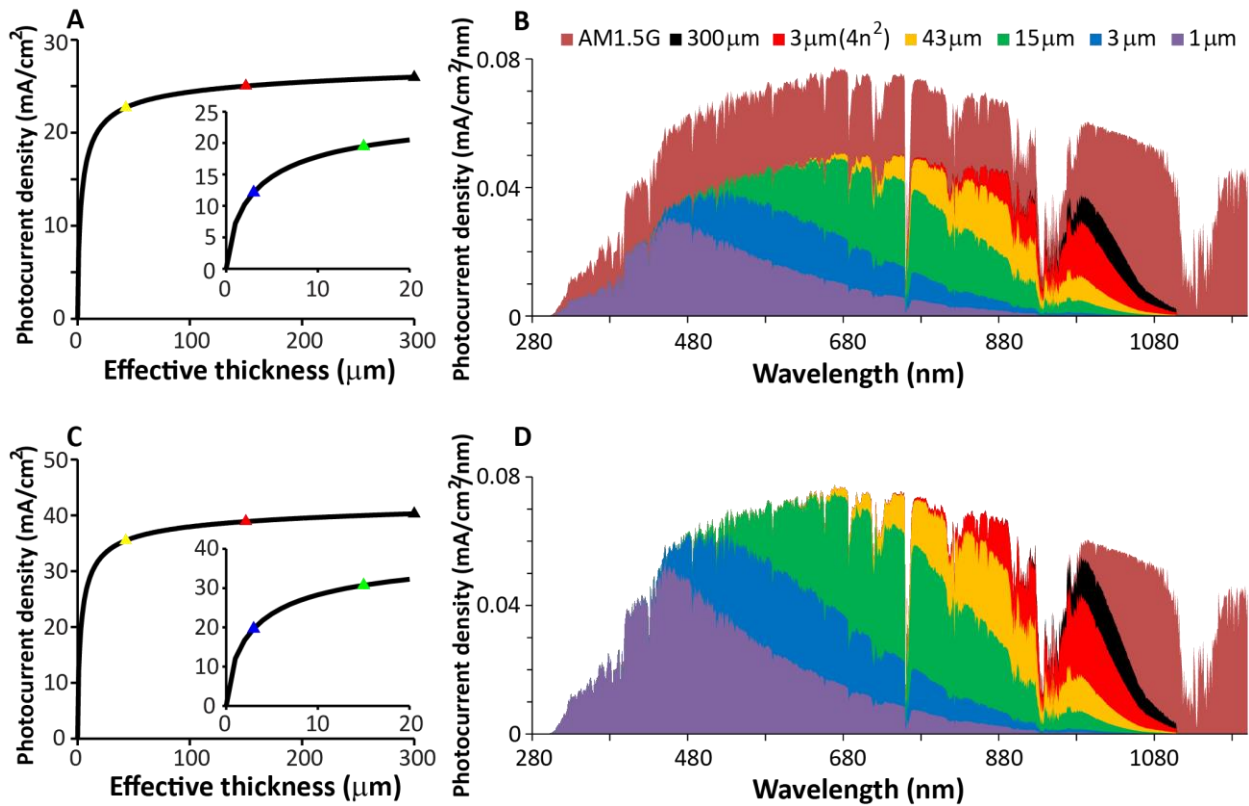
Figure 3.5. The effect of light trapping and antireflection on the optical absorption of c-Si film under AM1.5G solar spectrum. The photocurrent generation increases at a smaller rate with increasing thickness (A, C), highlighting the optical performance of 5 cases of selected c-Si film thickness. The insets in subplots A and C zoom in for the thickness ranging from 0 to 20 μm for clarity. The spectral optical absorption for the corresponding cases (B, D) shows that photocurrent improvement from thicker film is mainly from better absorbing the near-bandgap (λ = 1100 nm) infrared photons in the AM1.5G solar spectrum. About 40% of the photons could be reflected (A, B), assuming normal incidence of light, and leads to significant efficiency loss as compared to zero reflection loss (C, D).

Conventional c-Si PV cells are based on Si wafers of about 300 μm in thickness. With light trapping schemes [25,26,28,32] approaching the $4n^2$ limit or the Yablonovitch limit, a 3-μm-thick c-Si film could generate almost the same amount (only about 3% less) of photocurrent as a 300-μm-thick Si wafer (**Fig. 3.5**). This modelling result suggests that thin c-Si film PV concept in theory could deliver the same amount of photocurrent with only 1% of materials usage.

3.3.2. Light trapping and the Yablonovitch limit in thin film PV materials

For thin semiconductor film in the weak-absorption wavelengths, such as c-Si in the infrared range, light trapping becomes the enabling physics and the engineering goal to realize thin c-Si film PV concept with performance on par with the c-Si wafer-based PV cells. The light trapping effect is the enhancement in effective light path length due to total internal reflection inside the semiconductor film at the Lambertian surface [43] between the air and the semiconductor film, where the light rays outside of the escape cone (defined by the critical angle θ_C) is trapped inside the semiconductor film:

$$n_\lambda \cdot \sin \theta_C = 1 \cdot \sin 90^0 \qquad \qquad \textbf{Equation 3.4}$$

Due to light trapping, there is light concentrated inside the semiconductor film with intensity I_λ with units $\#/(s \cdot m^2 \cdot sr \cdot nm)$, which leads to the $4n_\lambda^2$ enhancement of light absorption. The escaping rate of photons q_λ^{out} is a function of the escaping cone per unit area dA:

$$q_\lambda^{out} = \int_{\phi=0}^{2\pi} \int_{\theta=0}^{\theta_C} I_\lambda \cos \theta \sin \theta \, d\theta \, d\phi = 2\pi I_\lambda \left(\frac{\sin^2 \theta_C}{2} - 0 \right) = \pi I_\lambda \frac{1}{n_\lambda^2} \qquad \textbf{Equation 3.5}$$

The absorption rate of photons per unit volume dAdL:

$$\dot{g}_\lambda = \int_{\phi=0}^{2\pi} \int_{\theta=0}^{\pi} \alpha_\lambda \cdot I_\lambda \sin \theta \, d\theta \, d\phi = 4\pi I_\lambda \alpha_\lambda \qquad \qquad \textbf{Equation 3.6}$$

Using the approach of detailed balance for the incoming rate of photons:

$$q_\lambda^{in} = q_\lambda^{out} A + \dot{g}_\lambda(AL) \qquad \qquad \textbf{Equation 3.7}$$

Therefore the ratio between the absorption rate and the incoming rate is:

$$\frac{4\pi I_\lambda \alpha_\lambda AL}{\pi I_\lambda \frac{1}{n_\lambda^2} A + 4\pi I_\lambda \alpha_\lambda AL} = \frac{\alpha_\lambda \cdot 4n_\lambda^2 L}{1 + \alpha_\lambda \cdot 4n_\lambda^2 L} \qquad \qquad \textbf{Equation 3.8}$$

The $4n_\lambda^2$ limit or the Yablonovitch limit states that:

$$\dot{g}_\lambda L = q_\lambda^{in}\left(1 - \exp\left(-\alpha_\lambda \cdot 4n_\lambda^2 L\right)\right) \qquad \qquad \textbf{Equation 3.9}$$

Hence, the ratio between the absorption rate and the incoming rate is as in **Eq. 3.30**, which agrees with **Eq. 3.28** as derived from the detailed balance approach.

$$\frac{q_\lambda^{in}\left(1-\exp\left(-\alpha_\lambda \cdot 4n_\lambda^2 L\right)\right)}{q_\lambda^{in}} = 1 - \frac{1}{\exp\left(\alpha_\lambda \cdot 4n_\lambda^2 L\right)} = \frac{\exp\left(\alpha_\lambda \cdot 4n_\lambda^2 L\right)-1}{\exp\left(\alpha_\lambda \cdot 4n_\lambda^2 L\right)} \approx \frac{1+\alpha_\lambda \cdot 4n_\lambda^2 L-1}{1+\alpha_\lambda \cdot 4n_\lambda^2 L} = \frac{\alpha_\lambda \cdot 4n_\lambda^2 L}{1+\alpha_\lambda \cdot 4n_\lambda^2 L}$$

Equation 3.10

At the weak absorption limit where $\alpha_\lambda \approx 0$ and $\alpha_\lambda \cdot 4n_\lambda^2 L \ll 1$, we have expanded the exponential function with the first order of the Taylor series:

$$\exp\left(\alpha_\lambda \cdot 4n_\lambda^2 L\right) \approx 1 + \alpha_\lambda \cdot 4n_\lambda^2 L \qquad\qquad \textbf{Equation 3.11}$$

3.3.3. Fabrication of thin c-Si film PV cells

Thin c-Si film PV cells [104] have been successfully produced from both a top-down approach and a bottom-up approach. In a top-down approach, a thin layer of c-Si film is peeled off from a Si wafer. For example, using layer transfer techniques [105,106], a 43-μm-thick c-Si film can be obtained from porous Si and fabricated into a 19.1%-efficient PV cell [107]. This high-efficiency cell has incorporated laser ablation for point contact and aluminnum oxide for surface passivation. The textured front surface with 4-μm-tall pyramids leads to good light absorption, or a short-circuit current density of 37.8 mA/cm^2, which is more than 35.5 mA/cm^2 or the theoretical photocurrent for a single-pass 43-μm-thick c-Si film (**Fig. 3.5C**).

In a bottom-up approach, the c-Si film is grown directly on a substrate, for example, by hot-wire chemical vapor deposition (HWCVD) [108-110]. The c-Si film can be grown epitaxially from a seed layer and fabricated into a PV cell [111-114]. A variety of techniques have been explored to produce the essential seed layer with good quality (μm-large crystal grains with low-angle grain boundaries). For example, the Stanford group uses ion beam to selectively remove unwanted crystal orientations during deposition of CaF$_2$ [112], which is then used as the seed layer. Another Stanford group uses arrays of patterned Si microwires as the seeds for growing the thin film absorber [113]. James Im from the Columbia University produced about 2-μm-large c-Si grains from mixed phase solidification [111] by multiple laser scannings of a Si film. In the next chapter, laser crystallization of Si nanostructures (thin film, suspended membrane, and nanoparticle) is carried out to explore new ways to produce large c-Si grains and understand the disbribution of crystal orientations from nucleation events.

4. Laser Crystallization of Si Nanostructures: High-Quality Seed Crystals

Preparation of high-quality crystalline silicon (c-Si) thin film on non-epitaxial substrate has important applications for more affordable photovoltaics [110,112,113] and higher performance thin film transistors [115,116]. This materials platform is desirable for crystalline silicon on insulators (SOI) applications [117-119]. Seeded crystallization by either laser scanning [120] or melt-mediated growth [121] has been previously applied to produce Si crystals of micrometers in size from their amorphous phase. Instead of relying on a single-crystalline silicon substrate, this chapter demonstrates production of such seeds from optimizing the laser fluence of Gaussian beam profile in different lateral growth regimes [122,123], where the lateral grain growth is largely enabled by the fluence gradient [115,124]. With optimized fluences, lateral grains are merged laterally into larger grains of several micrometers in size by sequentially scanning the pulsed laser beam, or sequential lateral growth (SLG) [125].

Spontaneous nucleation in the center of the bulk liquid Si is a limiting factor for the duration and thus the length of lateral growth length [123], several strategies have been previously employed to delay the nucleation in the bulk liquid Si, such as heating the substrate [122], increasing the thickness (thermal capacity) of a-Si film [126], and heating the film by a second background laser [127-129]. This chapter explores a new strategy to suppress the nucleation in the bulk liquid Si by crystallizing a suspended a-Si membrane, where the heat losses are forced to transport only in lateral dimensions.

Since the crystallinity of laser crystallized films is determined by the nucleation process, understanding the microscopic behavior of nucleation and crystal growth of a single-crystal nanodomain is a prerequisite to engineering the films' crystallinity. The third experiment in this chapter describes laser crystallizing Si nanoparticles, which are confined on oxide nanostructures during repetitive pulses of laser crystallization.

4.1. Fundamental Thermophysics of Nucleation and Crystal Growth

4.1.1. Fundamental driving force of phase change

The driving force for phase change among crystalline silicon (c-Si), amorphous silicon (a-Si), and liquid silicon melt (l-Si) is the second law of thermodynamics, or minimization of the Gibbs free energy in a thermodynamic system (with constant number of species, pressure, and temperature), as defined in **Table 4.1**. Moreover, the second law of thermodynamics can be also expressed as the extremum principles of the entropy, the internal energy, the Helmholtz free energy, and the enthalpy for various thermodynamic systems [130].

First law of thermodynamics: $dU = \delta Q - \delta W$
Second law of thermodynamics: $dS \geq \frac{\delta Q}{T}$

Table 4.1. Second law of thermodynamics applied for various systems.

Thermodynamic property (for a system with constant ...)	Definition	Extremum principles
Entropy S (N, V, U)	S	$dS = 0$; $d^2S < 0$
Internal energy U (N, V, S)	U; $dU = \delta Q - \delta W = \delta Q \leq TdS$	$dU = 0$; $d^2S > 0$
Helmholtz free energy F (N, V, T)	$F = U - TS$; $dU = \delta Q \leq TdS$; $dF = dU - TdS - SdT \leq SdT$	$dF = 0$; $d^2F > 0$
Enthalpy H (N, P, S)	$H = U + PV$; $dU + PdV = \delta Q \leq TdS$; $dH = dU + PdV \leq TdS$	$dH = 0$; $d^2H > 0$
Gibbs free energy G (N, P, T)	$G = U + PV - TS$; $dU + PdV = \delta Q \leq TdS$; $dG = dU + PdV - TdS \leq 0$	$dG = 0$; $d^2G > 0$

For example, melting of c-Si or crystallization of l-Si (such as the Czochralski process) can be modeled as a system with constant number of species and pressure at the melting temperature (T_m). Therefore, minimization of the Gibbs free energy will determine the thermodynamically favorable phase and is visualized in a phase diagram (**Fig. 4.1**).
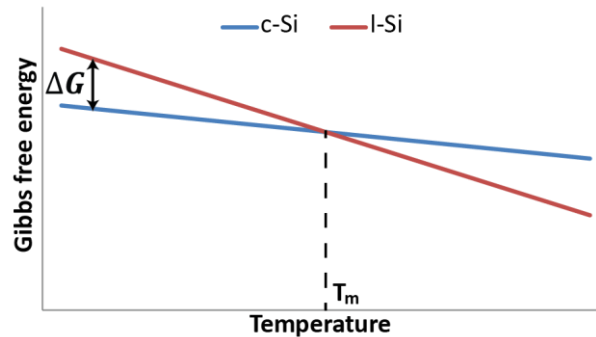
Figure 4.1. Phase diagram of Si near the melting temperature. The difference in the Gibbs free energy ΔG is the driving force of phase change.

At the melting temperature or 1685K, both the c-Si and l-Si phases can co-exist; in other words, the difference in the Gibbs free energy for the two phases is zero at T_m. Departure from the melting temperature will either favor the c-Si phase or the l-Si phase, driving either crystallization or melting, respectively. At small deviations from the equilibrium melting temperature, we can approximate the difference in enthalpy (or latent heat) ΔH and entropy ΔS between the two phases in **Eq. 4.1** as constant. And the driving force at temperature T, $\Delta G(T)$, is expressed as in **Eq. 4.2**.

$$\Delta G = \Delta U + P\Delta V - T_m\Delta S = \Delta H - T_m\Delta S = 0 \qquad \textbf{Equation 4.1}$$

$$\Delta G(T) = G_{l-Si} - G_{c-Si} = \Delta H - T\Delta S = \Delta H\frac{T_m-T}{T_m} \qquad \textbf{Equation 4.2}$$

As illustrated in **Fig. 4.1**, when the temperature is below T_m, $\Delta G > 0$ favors the c-Si phase and leads to crystallization of the l-Si. Likewise when the temperature is above T_m, $\Delta G < 0$ favors the l-Si phase and leads to melting of the c-Si.

4.1.2. Kinetics of crystallization: Nucleation rates and crystal growth velocity

Phase change, either crystallization or melting, is driven by minimization of the Gibbs free energy and normally involves a departure from the equilibrium melting temperature as in **Eq. 4.2**, in terms of supercooling or superheating. The study on kinetics of crystallization has formed a series of models [*131*] to describe the rate of forming the crystalline nuclei and interface velocity between the crystalline phase and the liquid phase.

For crystallization, supercooling favors the c-Si phase, which has a lower Gibbs free energy; however, forming a nucleus requires creating a new interface between the c-Si and the l-Si, and this interfacial energy acts as an energy barrier for nucleation (**Eq. 4.3**). $\Delta G^*(r)$ is the change in total free energy, comprising both the change in the Gibbs free energy [*132*] as a function of temperature $\Delta G(T)$ and the increase in the interfacial energy γ [*133-135*].

$$\Delta G^*(\mathrm{r}) = \frac{4}{3}\pi\mathrm{r}^3\rho\Delta G(T) + 4\pi\mathrm{r}^2\gamma \qquad \text{Equation 4.3}$$

$$r^*(T) = \frac{2\gamma}{-\Delta G(T)} \qquad \text{Equation 4.4}$$

$$\Delta G^*(T) = \frac{16\pi}{3}\frac{\gamma^3}{\Delta G(T)^2} \qquad \text{Equation 4.5}$$

Figure 4.2 plots the free energy barrier ΔG^* as a function of nucleus radius for 4 temperatures. The values for density ρ, latent heat, and γ are 2328 kg/m^3, 1.80×10^6 J/kg, and 0.34 J/m^2, respectively. And the critical nucleus radius r^* is the minimum size of the crystalline nucleus to be thermodynamically stable in the l-Si. If the size of nucleus from thermal fluctuation is below the critical radius, it is thermodynamically favorable for the nucleus to shrink and re-melt. On the other hand, if the nucleus size is above the critical radius for the system temperature, the nucleus will be able to survive and grow in size (crystal growth). The critical nucleus radius r* in **Eq. 4.4** is obtained from finding the local maximum in **Eq. 4.3,** and the free energy barrier ΔG* is shown in **Eq. 4.5**.
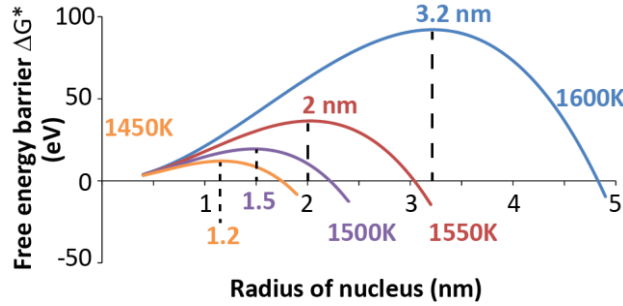
Figure 4.2. Free energy barrier for nucleation of c-Si in undercooled l-Si at 1600K, 1550K, 1500K and 1450K. The increased supercooling requires smaller critical radius [136].

Forming crystalline nuclei in the supercooled liquid is a result of statistical thermal fluctuation at the local volume, and a smaller volume tends to have fluctuations of greater relative amplitude [137]. For any additive thermodynamic quantity, such as the internal energy U, the relative fluctuation decreases inversely as the square root of the number of particles N. If we assume the number density of particles ρ_N to be constant across the system, the relative fluctuation of a thermodynamic property f is proportional to the inverse of the square root of the volume V (**Eq. 4.6**). Therefore, although the thermodynamic properties of a daily object is practically constant (enormous number of particles results in negligible fluctuations on the macroscopic scale), thermal fluctuation at the nanometer scale can be significant and enables nucleation events to happen at an observable time scale in experiment.

$$\frac{SD_f}{\bar{f}} \propto \frac{1}{\sqrt{N}} = \frac{1}{\sqrt{\rho_N}\sqrt{V}}$$

Equation 4.6

Combining the models for the free energy barrier and thermal fluctuation, the rates of successful nucleation events can be modeled [138,139] as a function of diffusivity of Si atoms in l-Si [140] and the Boltzmann factor of the free energy barrier (**Eq. 4.7**). The prefactor f is a model constant. For example, when $f = (4.18 \times 10^{10})^5/m^5$, the nucleation temperature in numerical simulation can be defined as $T_n = 1200\,K$, where the nucleation probability approaches 1 for a volume of $(10\,nm)^3$ and a duration of 1 nanosecond (**Fig. 4.3**).

$$\dot{N} = f\left[D_0 \exp\left(-\frac{E_d}{k_B T}\right)\right] \exp\left(-\frac{\Delta G^*(T)}{k_B T}\right)$$

Equation 4.7

A simpler model for nucleation rates [141,142] (**Eq. 4.8**) has also been used in literature, with the prefactor $\dot{N}_0 = 10^{39}/(\mathrm{m}^3.\mathrm{s})$ [134].

$$\dot{N} = \dot{N}_0 \exp\left(-\frac{\Delta G^*(T)}{k_B T}\right)$$

Equation 4.8

28
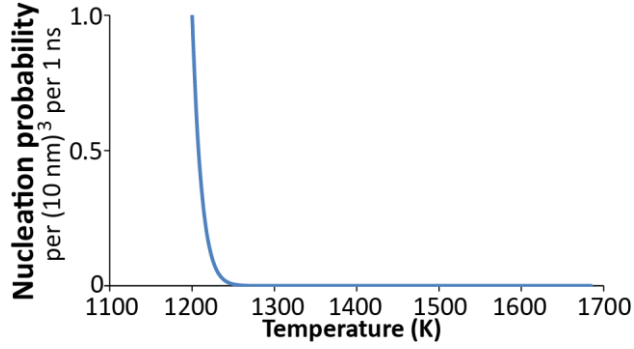
Figure 4.3. Nucleation probability as a function of temperature. The nucleation temperature in a simulation can be defined at unit nucleation probability per 1000 nm^3 volume and per 1 nanosecond.

Upon successful nucleation events (with the formed nucleus size larger than the critical nucleus radius), crystalline nuclei grow in size and further reduces the total free energy. The interfacial growth velocity has been experimentally studied [*143-148*]. And the interfacial kinetics can be modeled [*142,149*] based on the transition state theory (**Fig. 4.4**), which assumes that there is an intermediate state for transition between the l-Si and c-Si phases. The interface response function is expressed as in **Eq. 4.9**, where the prefactor g is again a model constant.
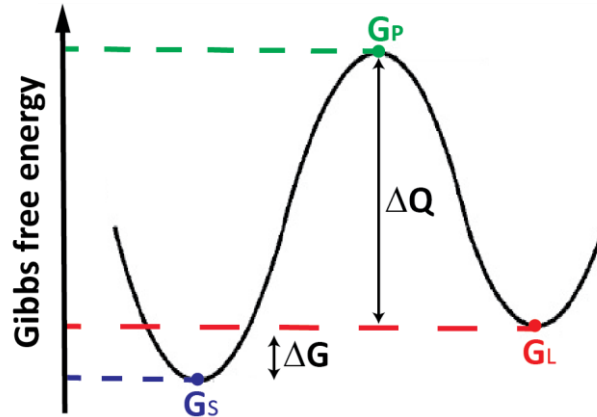
Figure 4.4. Illustration of the transition state theory for interfacial growth velocity. The difference in the Gibbs free energy ΔG between the crystalline phase G_S and the liquid phase G_L is the driving force, but the kinetics needs to overcome an activation barrier ΔQ imposed by the intermediate state G_P.

$$v_g = g \exp\left(-\frac{\Delta Q}{k_B T}\right)\left(1 - \exp\left(-\frac{\Delta G}{k_B T}\right)\right)$$

Equation 4.9

In the case of diffusion-limited crystal growth, the Wilson-Frenkel expression (**Eq. 4.10**) should be applied. Although the expression from the diffusion-limited Wilson-Frenkel model is similar to that from the transition state theory, the underlying kinetic model is different. E_d is the activation energy for self-diffusion of Si atoms in l-Si, and Δg is the difference in the Gibbs

free energy per atom. $g_{WF} = 1000$ m/s will give a maximum crystal growth rate of about 15 m/s (**Fig. 4.5**), consistent with the literature.

$$v_g = g_{WF} \exp\left(-\frac{E_d}{k_B T}\right)\left(1 - \exp\left(-\frac{\Delta g}{k_B T}\right)\right) \qquad \textbf{Equation 4.10}$$
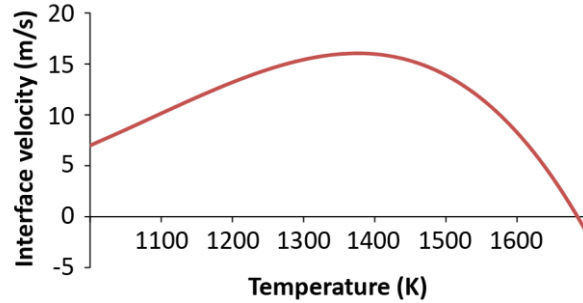
Figure 4.5. Crystal growth velocity for c-Si/l-Si interface. The shown interface response function is according to the diffusion-limited theory or the Wilson-Frenkel equation.

4.2. Lateral Growth of c-Si Grains by Pulsed Laser Crystallization

In laser-induced crystallization, complete melting of the thin Si film across its thickness is found necessary to launch lateral growth of c-Si grains, whereas partial melting, melting depth smaller than the film thickness, tends to produce fine grains mostly below 100 nanometers in size upon solidification [124,146]. Laser fluence, in the units of mJ/cm², measures the pulse energy normalized by the laser beam area. When the laser fluence is above the complete-melting threshold, the Gaussian profile of the laser irradiatiosn produces a temperature gradient in the molten Si. Solidification first happens in the cooler peripheral region, which is in the partial-melting regime, and the crystal grains are extended towards the center region by lateral growth (LG) [123]. Larger temperature gradient from a steeper fluence gradient delays the spontaneous nucleation in the center of the bulk liquid Si, and therefore leads to a longer duration (the melt duration is on the order of 100 nanoseconds) for lateral grain growth [124]. By controlling the laser fluence of the Gaussian beam, the temperature gradient in the molten Si are varied to tune the dynamics of nucleation and crystal growth during the pulsed laser crystallization process, resulting in different characteristics of crystal growth.

In this experiment, a-Si film of about 60 nm in thickness on a quartz substrate is prepared by standard low-pressure chemical vapor deposition (LPCVD) from silane (SiH₄) precursor at a deposition temperature of 550ºC (**Appendix A1.1**). This a-Si sample is subsequently irradiated with nanosecond laser pulses in the laser crystallization experiment using the same experimental setup as detailed in our previous report [150]. Laser power (**Appendix A1.2**) and beam spot size (**Appendix A1.3**) are measured to compute the laser fluence (mJ/cm^2).

The surface topology of the laser crystallized sample is characterized by Atomic Force Microscopy (AFM). After coating the sample's top surface of a few nanometers' gold, laser confocal microscopy by an Olympus LEXT OLS4000 model is also used to characterize the surface topology and compare with the AFM data. The sample's microstructure such as grain size is characterized by Scanning Electron Microscope (SEM) images of the delineated grain boundaries after Secco etching (**Appendix A1.4**).

4.2.1. Regimes of crystal growth

For laser fluences above the complete-melting threshold of a-Si film, 3 regimes of crystal growth have been observed (**Fig. 4.6**), characterized by the relative volume of fine c-Si grains and lateral c-Si grains, and by the presence of thermocapillary dewetting [*151-153*]. A set of 3 images (by AFM, laser confocal microscope, and SEM) of the crystallized disk after single laser pulse irradiation is obtained for a given fluence. The AFM characterization helps understanding the surface topology of the laser crystallized region, and check for any significant loss of Si material under high laser fluences. Laser confocal microscopy is a facile optical approach to obtain surface topology. The thin film's surface topology from laser confocal microscope is compared with the AFM data of the identical spot of interest, although our quantitative volume analysis is based on AFM height data. SEM images of heavily Secco etched samples offer the required high resolution to observe the characteristics of crystal grains, such as the length of lateral c-Si grains and the total area of fine c-Si grains.

For relatively low fluences (**Fig. 4.7**) no apparent lateral growth (LG) of c-Si grains is observable; instead the center of the circular crystallized disk is dominated by fine (less than 100 nanometers in lateral dimensions) c-Si grains, which results from a high density of spontaneous nucleation from the undercooled liquid Si. Here we refer to this range of laser fluences as the sub-LG regime.

When the laser fluence is gradually increased (**Figs. 4.6 A, D, & G**), the increased fluence gradient delays the spontaneous nucleation in the center and allows more time for lateral growth. Inward lateral grain growth starts to be observable near the center of the crystallized disk, and the impingement of grains creates a bump in the center. This range of laser fluences is referred to as the partial-LG regime.

Further increase in the laser fluence leads to a longer lateral growth duration and about 2 μm in lateral growth length (**Figs. 4.6 B, E, & H**). A distinct feature in this crystal growth regime is the spontaneous nucleation in the center, which leads to another lateral growth front outwards from the center. The lateral growth is completed by the impingement of the two growth fronts, inward from the cold boundary of the crystallized disk and outward from the central spontaneous nucleation. This range of laser fluences produces lateral grains of the maximum lengths and is used in this work for sequential lateral growth by pulsed laser crystallization, which is referred to as the super-LG regime.

Note that, however, further fluence increase above the super-LG regime leads to significant evaporation of Si material in the hottest center, and molten Si near the center moves outwards, forming a circular ring upon solidification. Volume analysis of the AFM measurement (**Fig. 4.6C**) shows that about 12% of the volume deficit in the center is due to evaporation and about 88% is pulled outwards to form the circular ring. We refer to this range of high laser fluences as the microring regime (**Fig. 4.6I**).
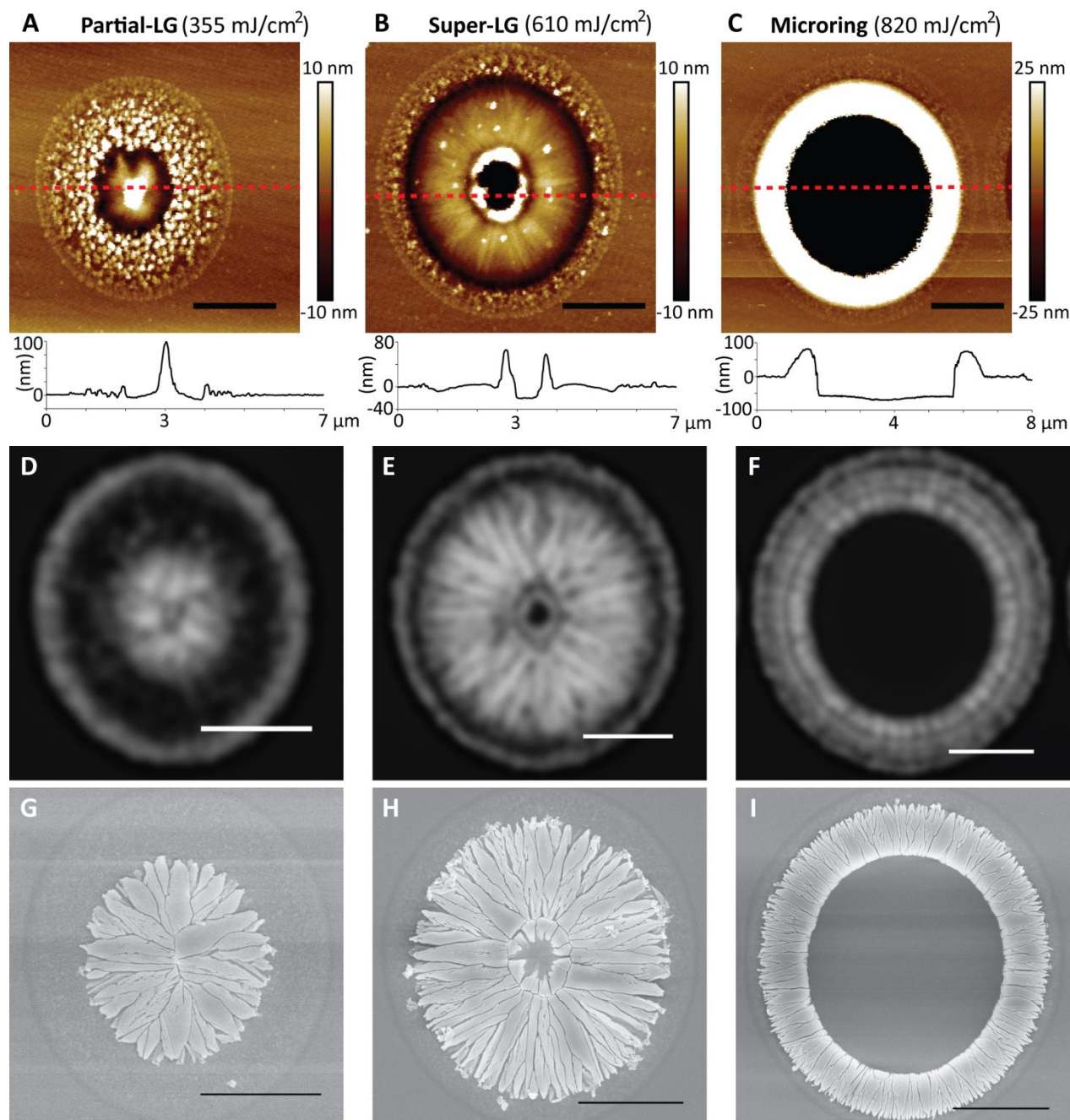
Figure 4.6. Regimes of crystal growth by pulsed laser crystallization using a 10x objective lens. The surface topology is examined by AFM before Secco etching (A-C), by laser confocal microscope after

0.75-minute Secco etching (D-F), and by SEM after 2-minute Secco etching (G-I). The height profiles are based on the the red dashed line in the AFM images (A-C). Images in the same column, for example A, D, and G, are from the same laser fluence of 355 mJ/cm^2. The scale bars are 2 μm.

2 μm
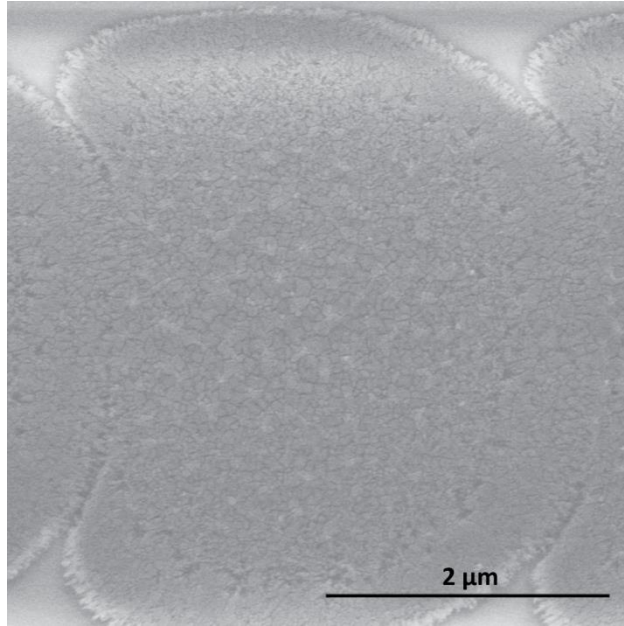
Figure 4.7. Fine c-Si grains by pulsed laser crystallization at laser fluences in the sub-LG regime. The imaged sample undergoes moderate Secco etching for only 0.75 minute to protect the fine c-Si grains from lift-off.

The onset of spontaneous nucleation in the center in the super-LG regime leads to an outward lateral growth front and consumes liquid Si, which could otherwise remain available for the desired inward lateral growth. The driving force for this spontaneous nucleation is a supercooled temperature, which is lower in the center than that in the surrounding adjacent liquid Si region. Due to the Gaussian profile of the laser beam, the center of the liquid Si region had the maximum global temperature. But the center became the preferred location for spontaneous nucleation by cooling faster than the surrounding adjacent liquid region, which had a lower temperature initially. One possible reason for this "unconventional" temperature profile is the latent heat released at the solid-liquid interface of the lateral grain growth, which is located about 1 micrometer away from the center (cf. the data in **Fig. 4.6H & 4.16A**). The solidification from l-Si to c-Si will lead to a local increase in temperature at the solid-liquid interface, which drives the lateral heat away from this phase-change interface, both outwards into the solid region and inwards into the liquid region in the center. (The characteristic length of the heat diffusion in liquid Si, $l_{th} = \sqrt{\alpha_l \tau}$, for a duration of 100 nanoseconds is about 1.6 μm, which is comparable to the distance between the center and the solid-liquid interface.) As the heat loss from the liquid film to the substrate continues, the temperature in the center of the liquid region, which is far from the latent-heat-releasing solid-liquid interface, can become the new global minimum within the liquid region.

33

It is reasonable to expect that an initial temperature profile with a flatter gradient will be subject to a more pronounced effect from the latent heat released at the solid-liquid interface than an initial temperature profile with a steeper gradient. Thus with a flatter initial temperature profile, the center of the liquid region is more likely to evolve to be the minimum local temperature and initiate spontaneous nucleation. Note that when the fluence of the Gaussian beam is lower, the temperature gradient in the center is also lower (flatter) (**Fig. 4.8B**). Therefore, spontaneous nucleation should also be expected for laser fluences in the partial-LG regime. However, in some cases with lower laser fluences such as in the partial-LG regime (**Fig. 4.6G**), spontaneous nucleation is absent in the center.

Another factor in explaining the spontaneous nucleation in the center is the coupled mass transfer during the pulsed laser crystallization. Comparing the final height profile of the crystallized regions between the partial-LG regime (**Fig. 4.6A**) and the super-LG regime (**Fig. 4.6B**), a notable difference is a significant mass deficit of Si material in the center for the super-LG regime. For a given heat flux to the substrate, a reduced thermal capacity (mC_p) due to less mass of the l-Si in the center (**Fig. 4.6B**) will result in a higher cooling rate, which contributes to a minimum local temperature in the center, leading to the observed spontaneous nucleation in the center. In **Section 4.3**, a suspended a-Si membrane is designed to minimize the heat loss to the substrate, where the primary driver for the occurrence of spontaneous nucleation in the center will be due to the latent heat released at the solid-liquid interface as previously discussed.

The underlying mechanism of this observed mass transfer in liquid Si may be due to the thermocapillary effect, where the surface tension of the liquid Si is smaller in the hotter center due to a negative temperature coefficient in the surface tension relation [*154*,*155*] and the Si material is pulled outwards from the hotter, smaller surface tension region in the center. The amount of the mass transfer even at the ultrafast time scale of hundreds of nanoseconds is still significant: about only 2/3 of the Si material remains in the center (**Fig. 4.6H**).

4.2.2. Radius of phase-change area

Quantitative study of the size of crystalized disk and the laser fluence is performed for optimizing the lateral grain growth. **Fig. 4.8A** summarizes the nonlinear relationship between laser fluence and the average size of the crystalized disks, which are defined by the boundary between the a-Si and fine c-Si regions. Higher laser fluence F leads to larger radius of the crystallized disks r, but that effect is diminishing in the high fluence range approaching the microring regime. The dotted curve in **Fig. 4.8A**, from the regression analysis, suggests that the maximum size of the crystallized disk is obtainable with high laser fluences close to the microring regime.
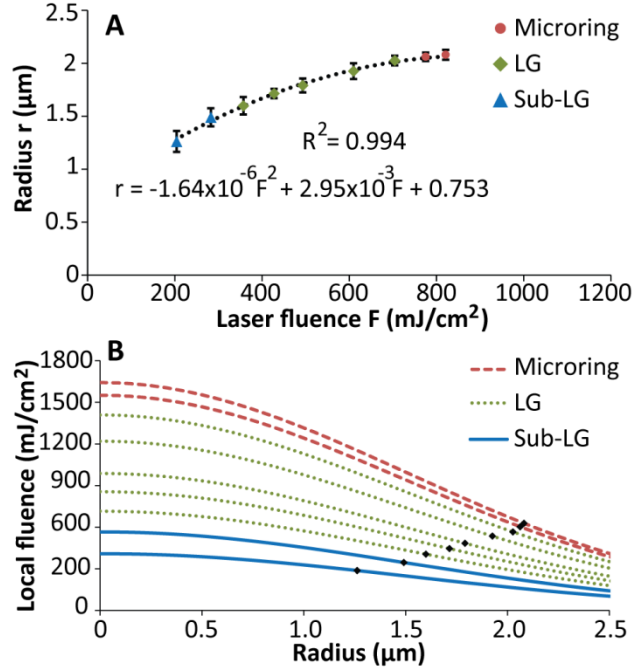
Figure 4.8. The effect of laser fluence on the average size of the crystallized disks. Second-order polynomial fit (the dotted curves) for the data in the sub-LG (blue triangle) and LG (green diamond) laser fluence regimes has an r-squared (R^2) value of 0.994 (A). The error bars are from 10 observations per data point. The fluence gradient at the phase-change boundary increases, as highlighted by the dots on the Gaussian profiles of incident laser energy density (B).

The incident laser energy density locally at the circular phase-change boundary between the a-Si and fine c-Si regions, based on the Gaussian profile (**Eq. 4.11**), rises with increasing laser fluence (**Fig. 4.8B**). F(r) is laser fluence as a function of r, the distance from the Gaussian laser beam center, w, the $1/e^2$ beam radius, and F_0. And F_0 is a coefficient relating E, the total laser beam energy, and F, the irradiated laser fluence, as in **Eq. 4.12**. Higher intensity of local laser irradiation at the phase-change boundary is needed for higher laser fluences (**Fig. 4.8B**). Steeper fluence gradient leads to a higher rate of lateral heat transport outwards and therefore requires higher laser energy input for local melting.

$$F(r) = F_0 \exp\left(-\frac{2r^2}{w^2}\right)$$
<div align="right">**Equation 4.11**</div>

$$E = F\pi w^2 = \frac{F_0}{2}\pi w^2$$
<div align="right">**Equation 4.12**</div>

4.2.3. Large-scale laser processing of a-Si films

The super-LG regime is found to be the optimum range of laser fluences for sequential lateral growth. Both the sub-LG and microring regimes are not suitable for sequential lateral growth: the sub-LG regime produces mostly fine c-Si grains (< 100 nm), and the dramatic mass

transfer in the microring regime creates features of removed Si material. Moreover, the super-LG regime is found to produce longer c-Si grains than the partial-LG regime (**Fig. 4.9**). In sequential lateral growth of c-Si grains by overlapping laser pulses, the subsequent laser pulse needs to completely melt the undesirable c-Si grains produced by the previous laser pulse, and extend the desired lateral c-Si grains. Therefore, the irradiated laser fluence in the beam center of the subsequent pulse needs to be above the complete-melting threshold of the c-Si grains, which is much higher than the complete-melting threshold of the a-Si film primarily due to order-of-magnitude lower absorption coefficient of c-Si at the 532-nm wavelength (see **Appendix A1.5** for FDTD simulation of optical absorption in thin films).
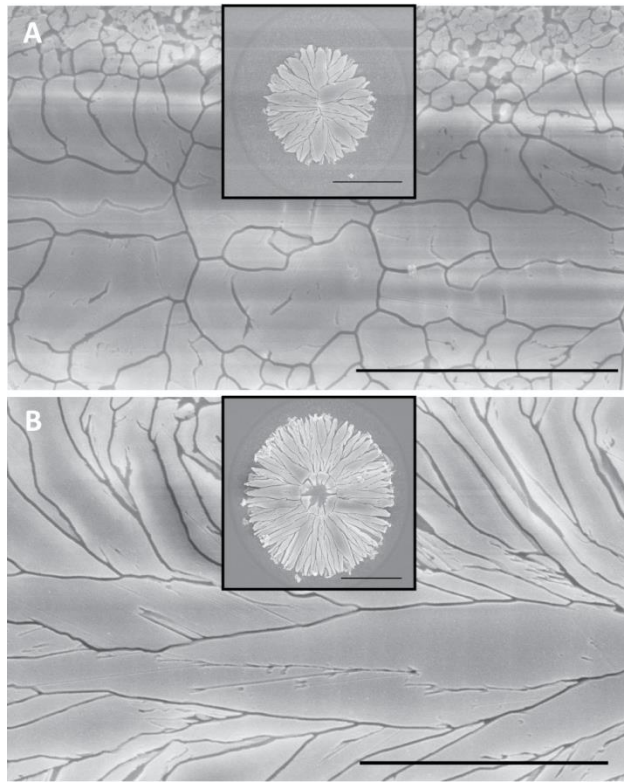
Figure 4.9. The optimum regime of laser fluences for sequential lateral growth. Scanning with overlapping laser pulses (from left to right in the images) with a repetition rate of 10 kHz and at a stage speed of 1 mm/s in the partial-LG regime yields sub-micrometer grains (A) while the super-LG regime yields grains with longest dimension beyond several micrometers (B). The insets show the SEM images of the corresponding single-pulse laser crystallization. The scale bars are 2 μm.

With laser fluences in the super-LG regime, large-grain thin c-Si film can be produced by sequential lateral growth. Scanning the laser pulses on the a-Si film leads to the elongation of c-Si grains in lateral directions (**Fig. 4.10**), resulting in either arrays of longitudinal c-Si stripes or large-area c-Si film. The location of c-Si stripes can be conveniently patterned by the pulsed laser crystallization process according to subsequent device fabrication processes for thin film transistors. The c-Si film can be potentially used as a seed layer for fabricating thin film solar cells [*112*].
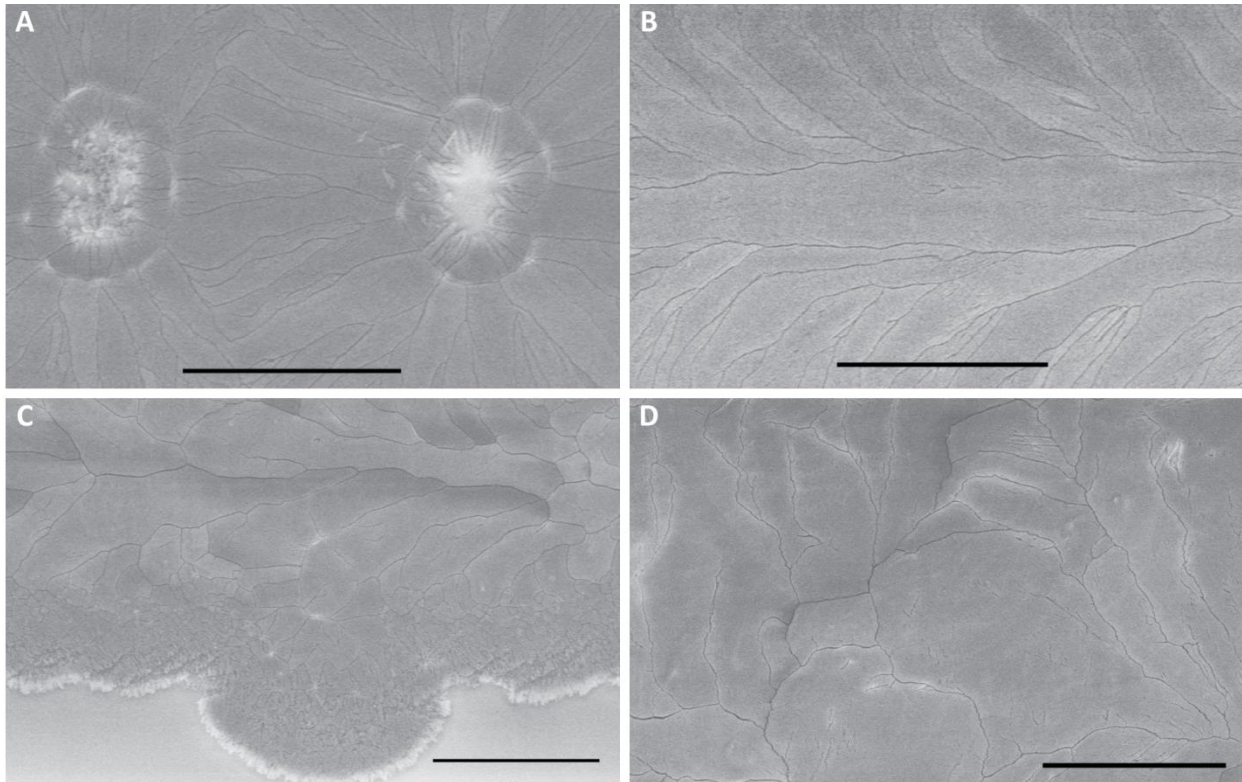
Figure 4.10. SEM images of sequential lateral growth of c-Si grains during successive laser pulses. Lines of pulsed laser scanning (in the x-direction, or from left to right) are placed by a pitch of 1 μm in the y-direction. Merging grains in the x-direction (A) yields longitudinal c-Si grains (B). Merging grains in the y-direction (C) yields a film of c-Si grains of up to 3 μm in size (D). The scale bars are 2 μm.

Laser fluences in the microring regime are useful in producing arrays of c-Si microrings with adjustable spacings and sizes, from the simultaneous patterning and crystallization capabilities of pulsed laser crystallization. Standard reactive ion etching (RIE) process is used to remove the a-Si film in the background and results in c-Si microrings on the transparent quartz substrate (**Fig. 4.11**).
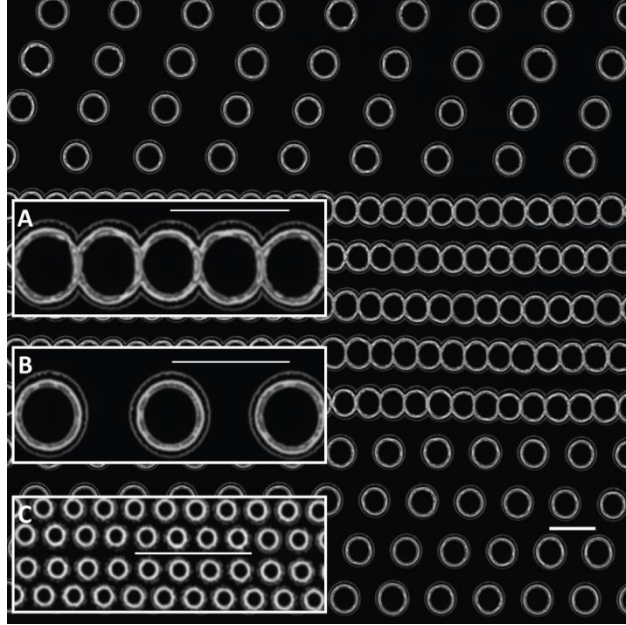
Figure 4.11. Optical images of c-Si microring arrays on a transparent substrate. Microrings are connected when spaced by 5 μm (middle of the image, or inset A), or remain as individual structures when spaced by 10 μm (lower part of the image, or inset B). The size of the microring is reduced to an outer diameter of about 1.7 μm using a 50x objective lens (inset C). The scale bars are 10 μm.

4.3. Laser Crystallization of Suspended and Laterally Confined a-Si Membranes

The length of lateral c-Si grains in the previous experiment shows a maximum of about 2 μm, which is mostly related to the maximum time available for lateral grain growth. The upper limit in lateral grain growth is influenced by a second lateral growth front originating from spontaneous nucleation in the center (**Fig. 4.6H**). The length of lateral c-Si grains has been enhanced in previous studies by reducing the cooling rate in the Si film with substrate heating [*122*], increasing the thermal capacity with thicker a-Si film [*126*], or pre-heating the a-Si film with a second laser in the background [*127*]. Here we explore a new approach of drastically reducing the heat loss to the substrate by suspending the a-Si film (**Fig. 4.12**).

4.3.1. One-dimensional heat transport

In the conventional thin film structure, the heat in the molten Si liquid is transported away laterally (in the x and y directions in **Fig. 4.12A**), as well as into the substrate (in the z direction in **Fig. 4.12C**). The heat loss from the liquid Si into the substrate is an enabling factor for the spontaneous nucleation in the supercooled center (**Section 4.2**), instead of the liquid remaining hot until the lateral growth front approaches. The governing heat conduction equation is shown in **Eq. 4.13**, where $\dot{g}$ is the volumetric heat generation rate term, accounting for the heat

absorption from the laser pulse and also the latent heat during the phase change. The boundary conditions are shown in **Eqs. 4.13A-13C**, where the adiabatic boundary condition is assumed at the air/film interface (z=0). The initial condition is a uniform temperature at T_i.

$$\rho C_p \frac{\partial T(x,y,z,t)}{\partial t} = k\left(\frac{\partial^2 T(x,y,z,t)}{\partial x^2} + \frac{\partial^2 T(x,y,z,t)}{\partial y^2} + \frac{\partial^2 T(x,y,z,t)}{\partial z^2}\right) + \dot{g} \qquad \text{Equation 4.13}$$

$$T(x = -\infty) = T(x = \infty) = T_i \qquad \text{Equation 4.13A}$$

$$T(y = -\infty) = T(y = \infty) = T_i \qquad \text{Equation 4.13B}$$

$$T(z = -\infty) = T_i \text{ and } q(z = 0) = 0 \qquad \text{Equation 4.13C}$$
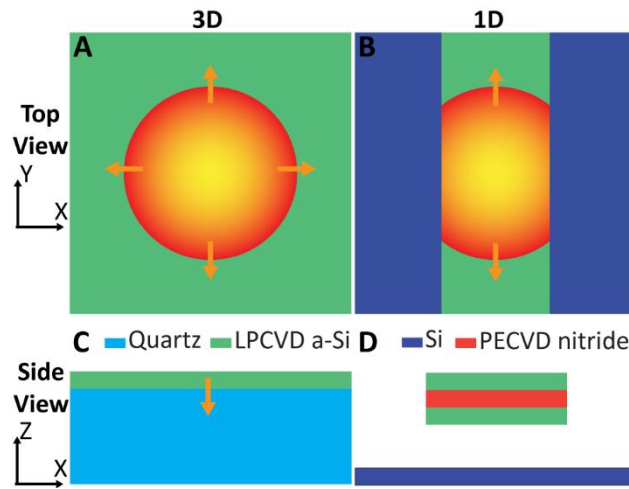
Figure 4.12. Characteristic heat transport in the conventional thin film structure and in the suspended a-Si membranes. The thick arrows (in golden color) in the top view (A) and side view (C) of the conventional thin film structure indicate the direction of major heat transport during the pulsed laser crystallization. In the a-Si membrane design, the top view (B) shows 1D heat transport in the y direction only, and the side view (D) shows adiabatic boundary conditions in the x and z directions.

In the suspended a-Si membrane (no substrate) of length L, additional adiabatic boundary conditions are applied to the x and z directions (**Fig. 4.12D**), and the heat transport is approximated as one-dimensional (1D) in the y direction (**Fig. 4.12B**). The governing equation, boundary conditions, and initial condition are simplified to **Eqs. 4.14, 14A, and 14B**, respectively.

$$\rho C_p \frac{\partial T(y,t)}{\partial t} = k\left(\frac{\partial^2 T(y,t)}{\partial y^2}\right) + \dot{g} \qquad \text{Equation 4.14}$$

$$T\left(y = -\frac{L}{2}\right) = T\left(y = \frac{L}{2}\right) = T_i \qquad \text{Equation 4.14A}$$

$$T(t = 0) = T_i \qquad \text{Equation 4.14B}$$

4.3.2. Sample fabrication
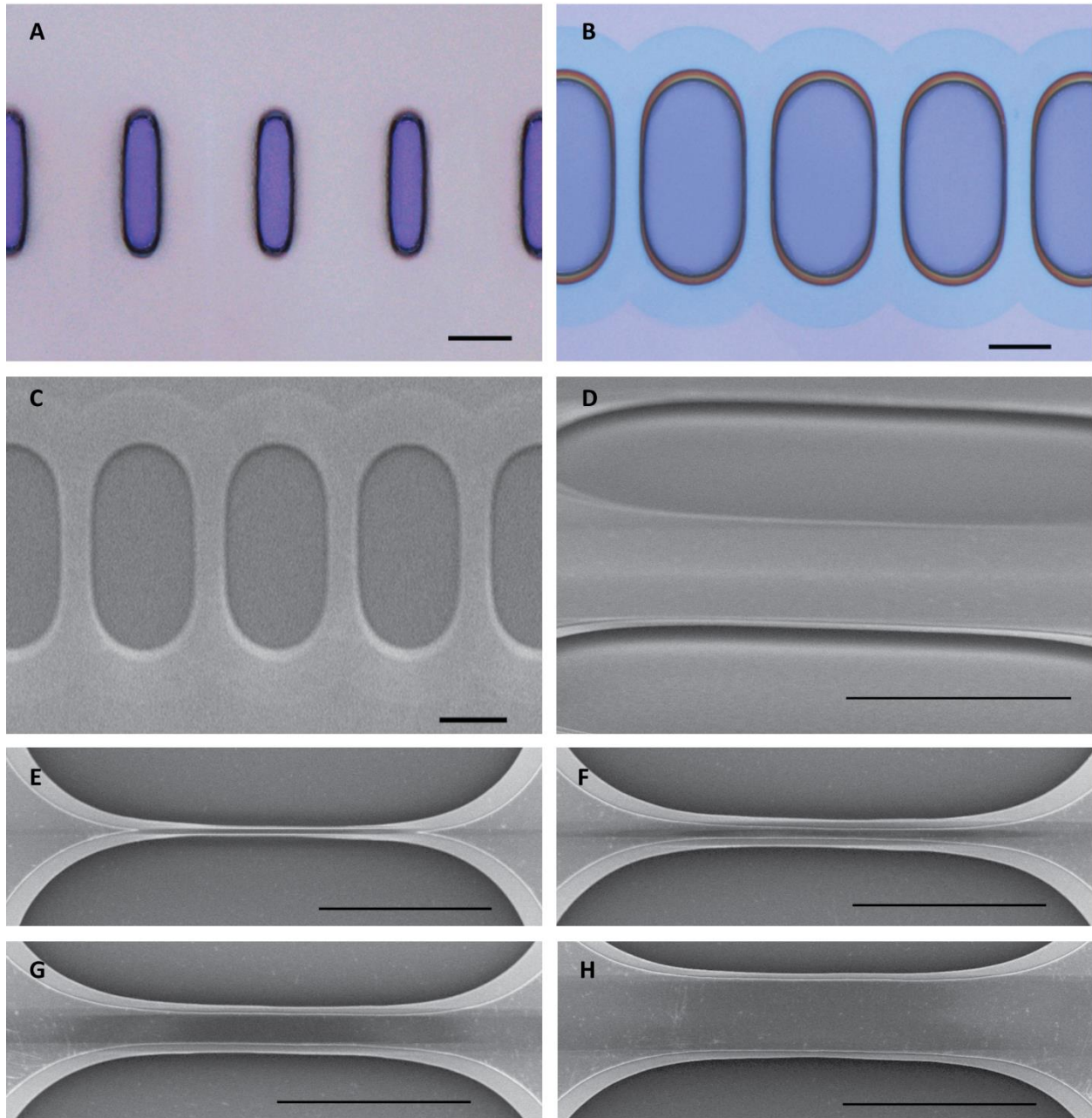
Figure 4.13. Fabrication of the suspended and laterally confined a-Si membranes. Laser lithography on the photoresist layer writes an opening between two membranes (A), and subsequent dry etching and BHF wet etching lead to suspended a-Si membranes. The suspended membranes have a color contrast in the optical image (B) and in the SEM image (C). The tilted SEM image (D) verifies a gap between the bridge and the Si substrate. The width of the a-Si layer is controlled by the pitch in the laser-defined openings (E-H). The scale bars are 10 μm.

Laser lithography and dry etching are applied to fabricate the suspended and laterally confined a-Si membranes (**Appendix A1.6 & A1.7**). The optical and SEM images in **Fig. 4.13** show the fabricated a-Si membranes. The a-Si membranes are verified to be fully suspended

from the Si substrate, by the color contrast in the optical (**Fig. 4.13B**) and SEM (**Fig. 4.13C**) images, and direct observation in the tilted SEM image (**Fig. 4.13D**). Laterally confined a-Si membranes with different widths have been successfully prepared by controlling the line pitch in the laser lithography step.

4.3.3. The lateral confinement and heat-transport-limited crystal growth

It has been shown that the grain boundaries tend to be normal to the advancing solidification front [*115*], thus along the heat transport direction. As the width decreases, the grain boundaries become parallel to the length of the a-Si membranes (**Fig. 4.14**), suggesting that 1D heat transport during solidification after pulsed laser irradiation has been successfully achieved for the narrow (width $\leq 2.5\ \mu m$) a-Si membranes.

Dewetting of the molten Si liquid causes the width of the membranes to shrink, resulting in the "neckings" observable in **Fig. 4.14**. As lateral c-Si grain growth initiates from the cooler side of the Si liquid and extends towards the hotter region in the center, the "neckings" also highlight part of this lateral growth region. The "neckings" also increase the growth competition among different grains especially at narrow widths (**Fig. 4.14**). At a width below 1 μm at the "necking" (**Fig. 4.14 C & D**), lateral growth of a single c-Si grain is observed.
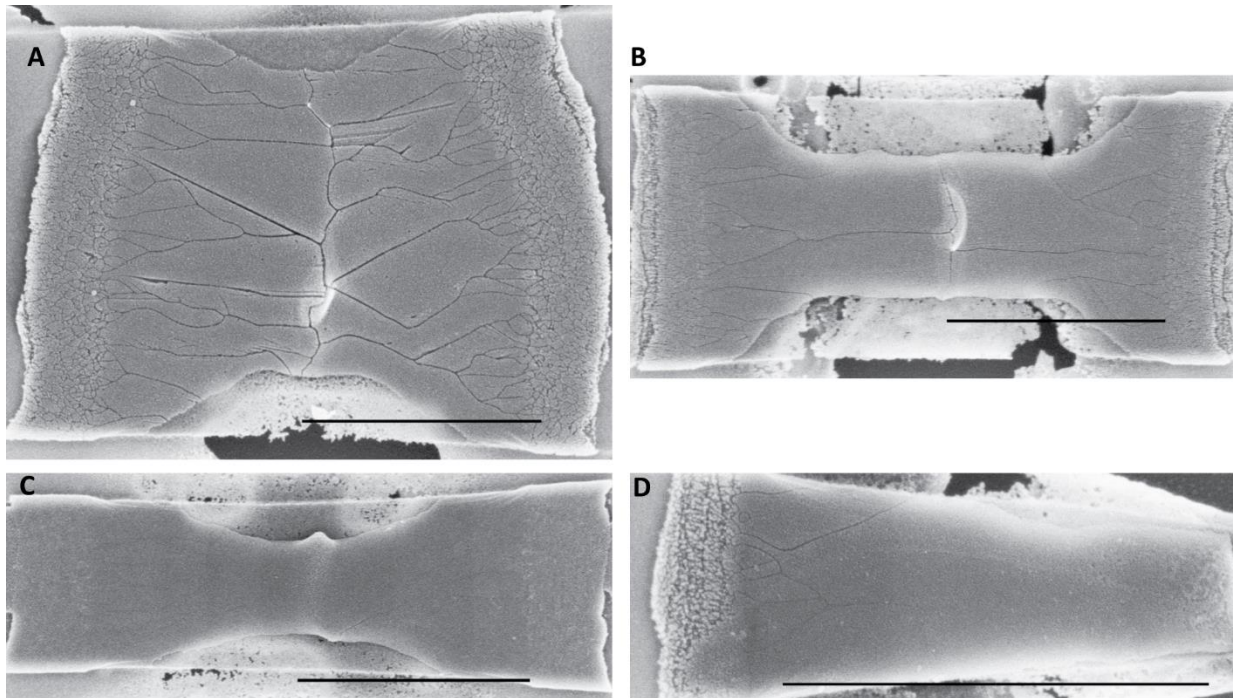
Figure 4.14. Lateral growth of c-Si grains in the a-Si membranes with different widths. Competition among different grains during lateral growth increases as the width decreases from 3.5 μm (A) and 2.5 μm (B) to 1.5 μm (C) and 0.5 μm (D), resulting in a single grain. The scale bars are 2 μm.

41

Evidence of heat-transport-limited crystal growth is also observed on this suspended a-Si platform, where the lateral confinement from narrow widths reduces the heat transport rate and thus the lateral growth rate. For the laser crystallized area near the end of the patterned suspended a-Si membrane (**Fig. 4.15**), the morphology of the c-Si grains becomes asymmetric: the length of the lateral growth on the right (in the patterned a-Si membrane) is about 1 μm, significantly shorter than that (at about 3.3 μm) on the left (in the un-patterned a-Si membrane). Given the same melting duration, this difference in lateral growth length is mainly due to the different crystal growth rates, which can be limited by how quickly the generated latent heat is removed from the solidification interface. In **Fig. 4.15**, the arc length on the left at the boundary between the a-Si (removed by Secco etching) and c-Si regions is about 8.4 μm, or 3 times the length of the phase-change boundary (or the width of the a-Si membrane) on the right. Thus, the cross-section area of lateral heat transport on the left is significantly larger, contributing to a larger heat removal rate from the solidification interface and a faster crystal growth rate.
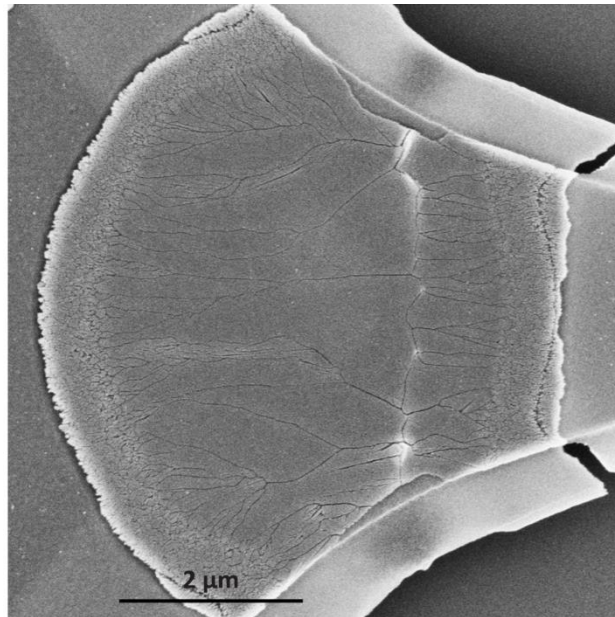
Figure 4.15. Heat-transport-limited crystal growth rate. Latent heat is released during the phase change (solidification) of Si from the liquid phase to crystalline phase, and needs to be conducted away from the solidification interface for the crystal growth to proceed.

4.3.4. Suppression of spontaneous nucleation

The suspension of a-Si film (removing the underlying substrate) eliminates heat loss to the substrate (**Fig. 4.12**), which could effectively minimize or indeed suppress spontaneous nucleation in the center of the molten Si liquid. For laser crystallization of the a-Si film with a substrate (**Fig. 4.16A**), heat loss to the substrate make it possible for the temperature in the center of the liquid Si to cool faster than the adjacent liquid region, which is closer to the lateral

growth front. For the suspended and laterally confined a-Si membrane (**Fig. 4.16B**), lateral heat transport dominates, and the initially hotter center only cools by lateral heat transport towards the outer region. Thus the center is at a relatively higher temperature, and impedes the probability of spontaneous nucleation.
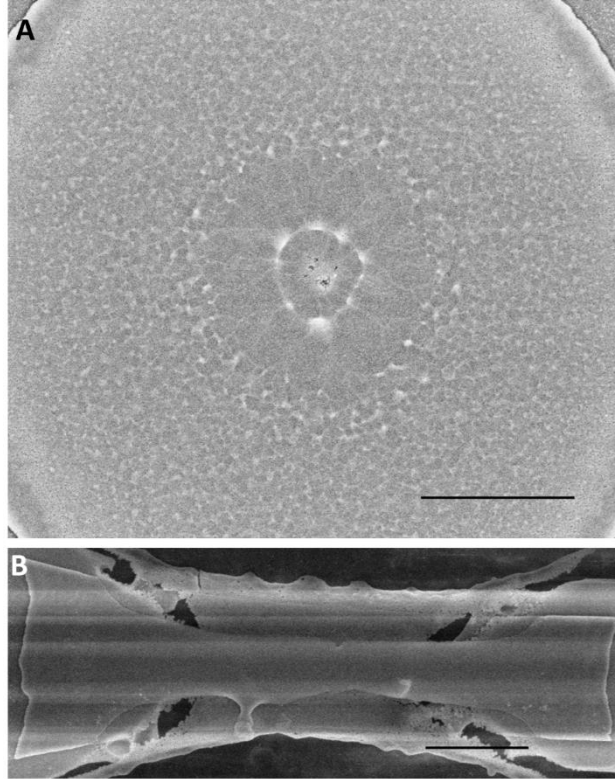
Figure 4.16. Suppression of spontaneous nucleation in the center. Spontaneous nucleation is observed for laser crystallization of a-Si film with a substrate (A). For laser crystallization of the suspended a-Si membrane with the same fluence, spontaneous nucleation in the center of laser beam spot is successfully suppressed due to absence of substrate cooling (B). The samples are treated with 1-minute Secco etching before SEM. The scale bars are 2 μm.

4.4. Laser Crystallization of Self-Confined Nanoparticles

In the complete-melting regime of pulsed laser crystallization of a-Si films, the nuclei initiated from the nucleation events serve as the seeds for crystal growth. Therefore, the quality of the crystallized c-Si film will be strongly influenced by the crystallographic orientations and the number density of these nuclei. Earlier experiments on laser crystallization of a-Si films have shown the possibility of preferred crystallographic orientation in either <1 0 0> [111] or <1 1 1> [156,157]. Similar preferred orientations, driven by minimization of surface free energy, have also been observed in growing Si nanowires of different diameters [158]. In this experiment, laser crystallization of self-confined Si nanoparticles, which are thermally connected to the substrate by a narrow oxide nanostructure

(**Fig. 4.17**), is carried out to understand the nucleation and crystal growth behaviors on the nanoscale domain. The oxide nanostructure "confines" the Si nanoparticle by limiting the interfacial area for nucleation and fixing the position of the Si nanoparticle (on the top of the oxide nanostructure) after laser crystallization.

Arrays of Si nanoparticles on a quartz substrate are first produced from thin a-Si film by pulsed laser irradiation with a donut-shape intensity profile. Subsequent timed buffered-HF (BHF) isotropic etching undercuts the Si nanoparticles and forms the oxide nanostructures underneath (**Fig. 4.17**). The radius of the oxide nanostructures is controlled by both the size of the Si nanoparticles and the BHF etching duration.
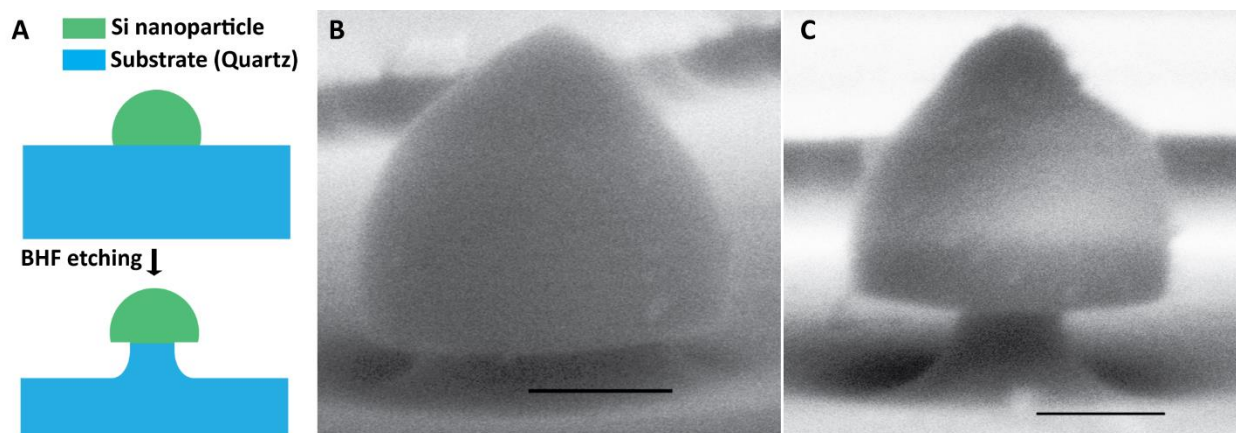
Figure 4.17. Si nanoparticles confined on top of the oxide nanostructures. The oxide nanostructure is formed by isotropic wet etching in 10:1 BHF (A), and the interfacial area between the Si nanoparticle and the oxide nanostructure is controlled by the BHF etching duration from 2 minutes (B) to 4 minutes (C). The scale bars are 200 nm.

The prepared Si nanoparticle arrays are then irradiated with a number of laser pulses (from 100 to 1000), which are controlled by the shutter time. The 532-nm laser beam is focused on the sample using a 10x objective lens. In the experiment, a matrix of conditions is used to study the effects of the laser pulse energy and the number of pulses on the crystallization behavior. Each condition is applied to 5 nanoparticles (**Fig. 4.18**) to observe the typical behavior.
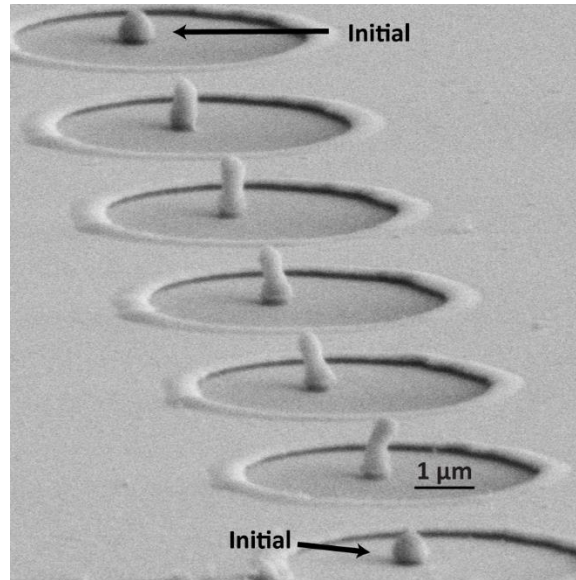
Figure 4.18. **Crystallization of self-confined Si nanoparticles on the oxide nanostructures.** 5 observations are generated for each condition (laser pulse energy and number of pulses).

Laser pulse energy strongly influences the final shape of the crystallized Si nanoparticles (**Fig. 4.19**). At low pulse energy (35 nJ), the final shape of the crystallized Si nanoparticle resembles a cone, without significant reduction in the width of the bottom portion (compared with the initial Si nanoparticle in **Fig. 4.17C**). At moderate pulse energy (57 nJ and 77 nJ), the final shape of the crystallized Si nanoparticle resembles an elongated column on top of the oxide nanostructure. At high pulse energy (97 nJ and 116 nJ), the final shape of the crystallized Si nanoparticle resembles a droplet, and significant volume reduction is also observed.

| 35 nJ | 57 nJ | 77 nJ | 97 nJ | 116 nJ |
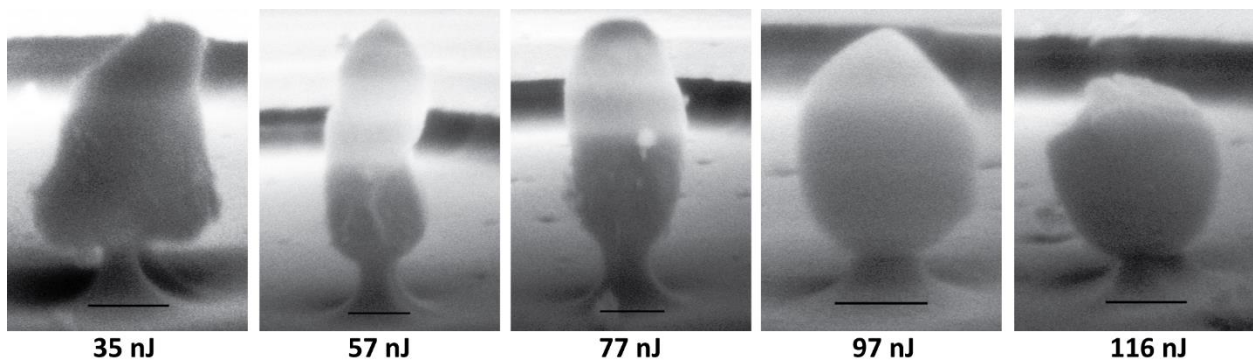
Figure 4.19. **Effect of laser pulse energy on the shape evolution of self-confined crystalized nanoparticles.** These 5 different samples are produced from nanoparticles of the same size after 4-minute 10:1 BHF etching, after 100 repetitive pulses with increasing pulse energy. The scale bars are 200 nm.

At high pulse energy, the nanoparticle fully melts by each of the 100 repetitive pulses and a droplet shape is formed by the molten Si liquid on the oxide nanostructure. The volume reduction (noted above) most likely arises from evaporation of Si material accompanying full

45

melting of the Si nanoparticle. At low and moderate pulse energy, each of the 100 repetitive pulses only partially melts the Si nanoparticle, and the liquid Si atoms diffuse next to the un-melted solid portion of the Si nanoparticle, causing an incremental shape change. The cumulative effect of the liquid Si movement induced by each laser pulse causes the dramatic morphology evolutions under repetitive laser pulses.

Repetitive laser pulses accumulate the incremental shape change by each laser pulse and "magnify" these changes into distinct morphology evolutions, which are observed with SEM inspections. The accumulation of incremental changes is referred to as the cumulative effect in this study (**Fig. 4.20**). With laser pulse energy in the complete-melting regime, the nanoparticle fully melts and the liquid Si forms a droplet on top of the oxide nanostructure, minimizing its interfacial energy. In this complete-melting regime, evaporation of Si material during each laser pulse is found to be significant, and a larger number of laser pulses leads to a greater volume reduction of the Si nanoparticle (**Fig. 4.20 A-C**). With moderate laser pulse energy in the partial-melting regime, the liquid Si tends to diffuse such that the initial hemispherical nanoparticle transforms into a column (**Fig. 4.20 D&E**), and a high-aspect-ratio Si nanostructure is obtained by a large number (1000) of laser pulses (**Fig. 4.20F**).
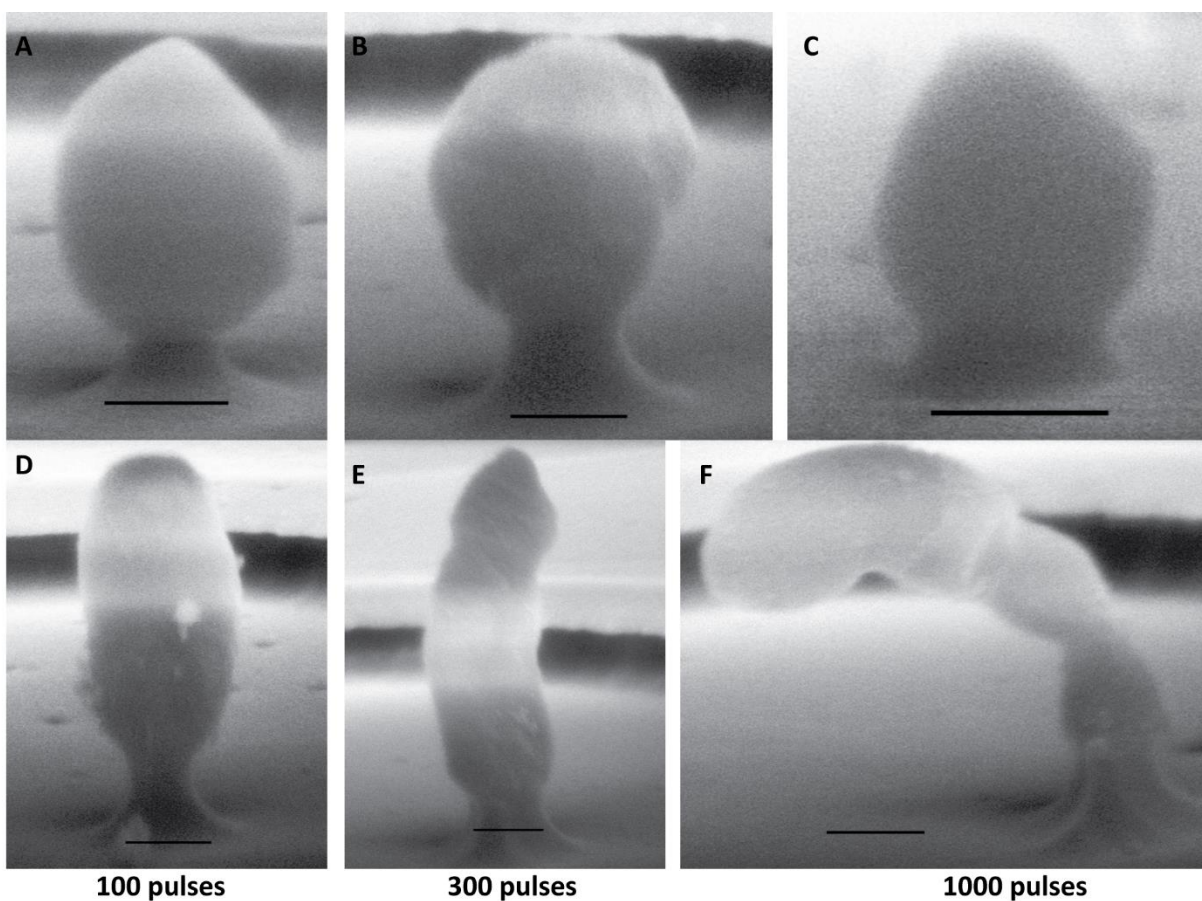
Figure 4.20. Cumulative effect of repetitive laser pulses on the shape evolutions. Surface evaporation of Si material, accompanying fully melting of the Si nanoparticle, leads to volume reduction after repetitive laser pulses (A-C). Diffusion of liquid Si on the surface of solid Si, in the partial-melting regime,

leads to elongation of the nanoparticles into columns (D-E) and high-aspect-ratio nanostructures (F). The scale bars are 200 nm.

Understanding the underlying mechanisms for the morphology evolutions in the partial-melting regime can be complicated by optical absorption in such nanostructures, where Beer's law and simple surface melting are invalid. For example, the FDTD simulation of a 300-nm-radius c-Si nanoparticle on an oxide nanostructure shows that the hot spot in optical absorption is located near the center of the nanoparticle rather than at its surface (**Fig. 4.21 A&B**). As the center of the Si nanoparticle presumably melts due to the strong optical absorption, the newly formed liquid core strongly absorbs radiation (one-order-of-magnitude stronger) and reflects radiation upwards from the solid-liquid Si interface (**Fig. 4.21 A&B**), which acts as a barrier for radiation to propagate down to the bottom of the Si nanoparticle. This optical absorption in nanoscale domain may be an important contributing factor for the bottom of the Si nanoparticle to remain intact at low laser pulse energy (**Fig. 4.19**).
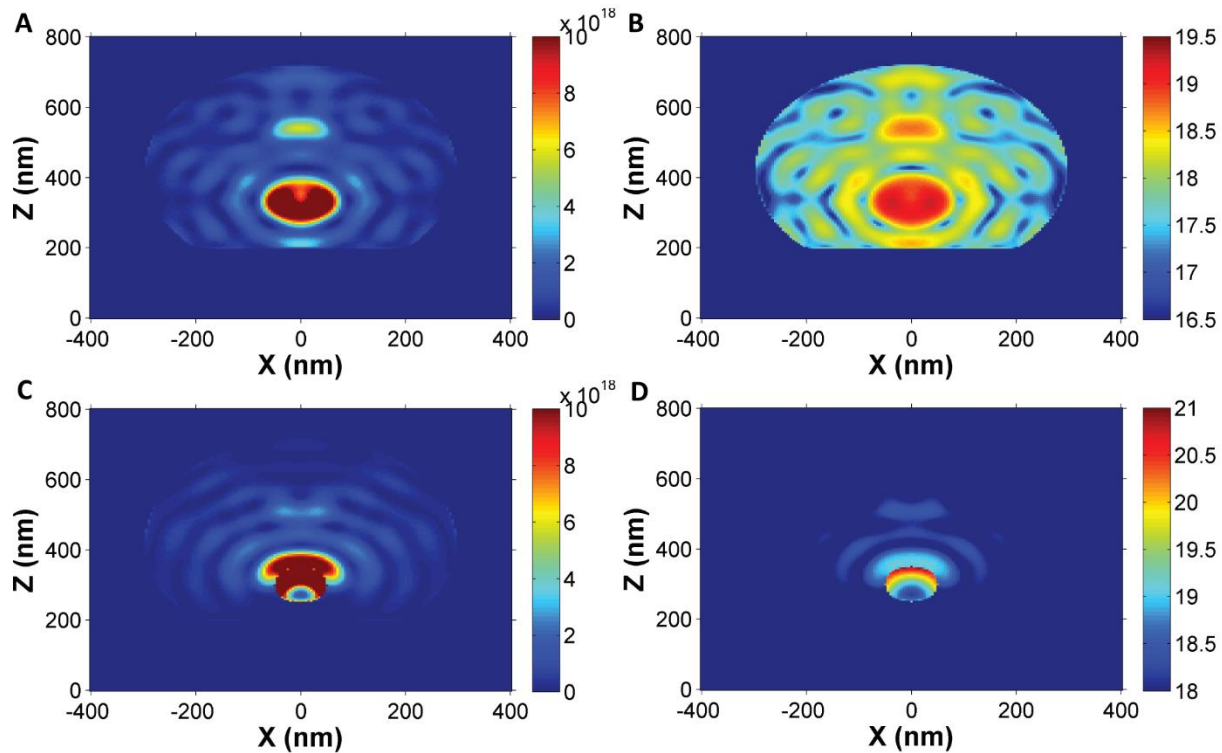
Figure 4.21. FDTD simulation of optical absorption of a 300-nm-radius c-Si spherical cap on top of a 200-nm-radius SiO₂ pillar. Strong optical absorption near the center of the nanoparticle is likely to cause melting to initiate at the center of the nanoparticle instead of at the surface (A). Placing a 50-nm-radius liquid-Si core inside the 300-nm-radius c-Si spherical cap (at Z=300 nm), the simulation (C) shows that the strongest optical absorption is located at the top of the liquid-Si core and the reflection from the top of the liquid-Si core leads to enhanced absorption in the solid-Si above the liquid-Si core. Log scale (B & D) of the optical absorption (A & C) is also shown for comparison. The simulations are carried out at the 532-nm wavelength.

47

4.5. Summary and Recommendations for Future Work

This chapter studied laser crystallization over a range of conditions from thin film, to suspended and laterally confined thin-film membrane, to self-confined nanoparticle on oxide nanostructure. In the parametric study for pulsed laser crystallization of thin-film a-Si on the quartz substrate, we used the optimum laser fluences in the super-LG regime for producing micrometer-size c-Si grains. We also investigated the effect of Si mass transfer in the liquid phase, in relation to the spontaneous nucleation in the bulk liquid. Suspended and laterally confined thin-film membranes were fabricated to study the 1D heat transport during pulsed laser crystallization, where the spontaneous nucleation was successfully suppressed by only allowing lateral heat transport. To study the nucleation and crystal growth of liquid Si on a confined interface, arrays of nanoparticles on top of oxide nanostructures were fabricated. The parametric study of pulsed laser crystallization of these Si nanoparticle arrays showed distinct morphology evolutions of these Si nanoparticles undergoing partial melting and full melting.

For future work, laser crystallization on suspended membranes may be applied to fabricate high-mobility Si devices. The configuration with arrays of Si nanoparticles on oxide nanostructures is an interesting system to study the probabilistic behavior of nucleation events in the supercooled Si liquid (with X-ray microdiffraction characterization). Compared with an earlier in-situ TEM study [*159*] of crystallizing Si nanopillars, this new configuration can reduce the complications from the partial melting of Si nanopillars and the cumulative effect from successive laser pulses and characterizations. Instead, the temporal distribution of crystallinity from the same Si nanopillar under repetitive laser pulses [*159*] can be visualized spatially over an array of crystallized Si nanocrystals on top of oxide nanostructures.

5. Engineering Innovation in Deploying Rooftop PV Systems

5.1. Geographic Distribution of Solar Resource and Retail Electricity Rates

The solar PV industry is now an important component of the global energy landscape, with the global PV market growing from 0.3 GW in 2000 to 38 GW in 2013 [10]. The top 4 economies, the United States, China, Japan, and Germany, are also the 4 major markets for PV installation (**Fig. 5.1**). This dramatic growth in PV deployment has made PV electricity a mainstream source to supply the electricity infrastructure in some nations. On 7 July 2013, a record 48% of the total peak electricity production in Germany was from solar energy (**Fig. 5.2**). With PV module prices decreasing from about $5.0/W to as low as $0.72 in 2013 [160], the global PV industry has now entered the critical phase of transitioning from being a subsidy-dependent industry to becoming cost-competitive with retail electricity in a growing number of regional markets [161-164].
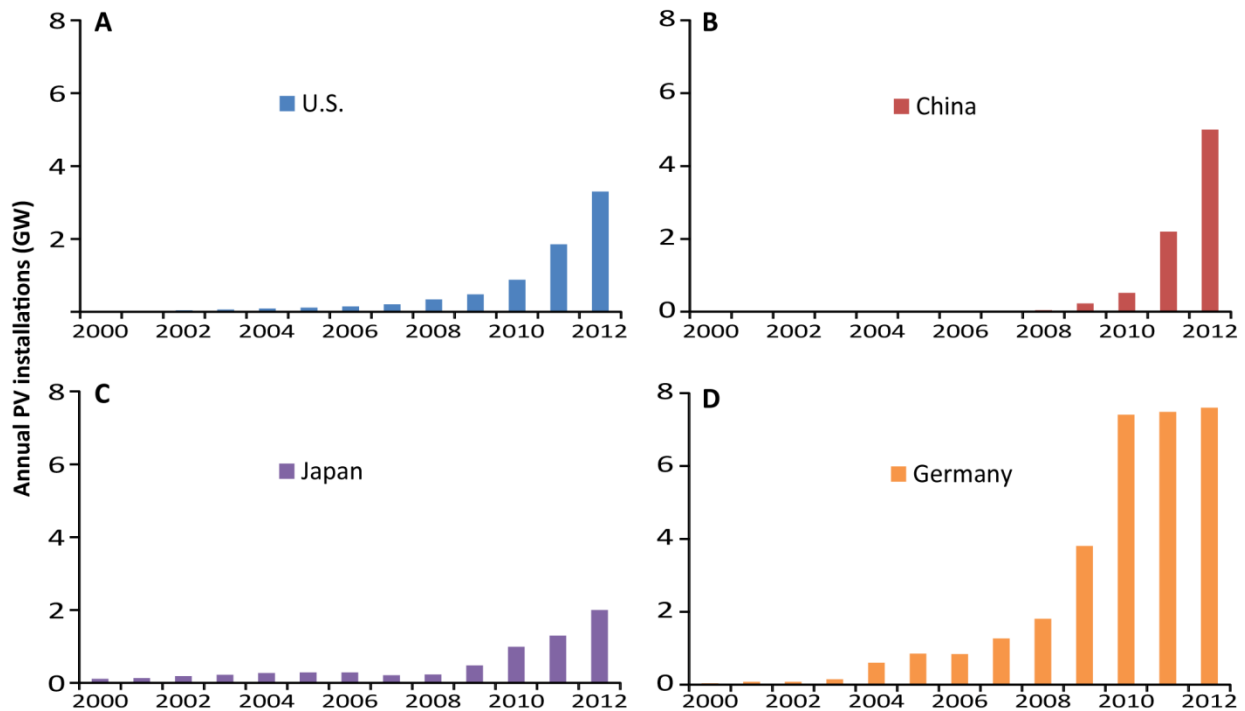
Figure 5.1. Market evolution in 4 major markets in the global PV industry. Source: EPIA.

Grid parity is when the levelized cost of electricity (LCOE) [165-167] from installed PV systems matches the retail electricity rate. There is no single "grid parity" price point but rather a price range for PV modules, due to a range of geographically varying factors including grid electricity rates (**Fig. 5.3**) and solar radiation resource (**Fig. 5.4**). A simplified LCOE formulation (**Eq. 5.1**) accounting mainly for these two factors are used in this chapter, where the LCOE is determined by the installed system cost P ($/W) and the discounted annual energy yields for a lifetime of N years at an interest rate of i. The annual energy yield per watt strongly depends

on the capacity factor (CF), which is the ratio of actual energy output to the theoretical output by operating at the rated power for 8760 hours/year. Key determinant to the capacity factor, solar radiation varies across the United States (**Fig. 5.4**), leading to a range of LCOE for the same PV system cost. The "grid parity" point varies by sector, as retail electricity rates vary across different sectors from residential, commercial, to industrial. In addition, electricity rates for the same sector also vary greatly across different states (**Fig. 5.3**).

$$P = LCOE \cdot \sum_{t=1}^{N} \frac{1 \cdot 8760 \cdot CF}{(1+i)^t}$$
Equation 5.1
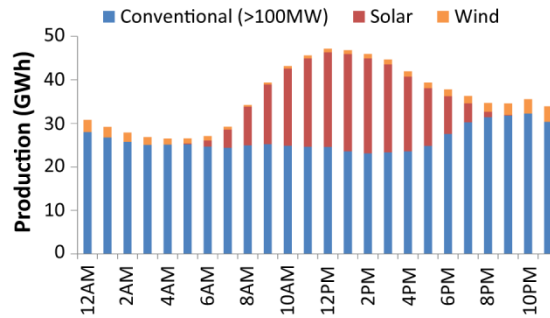
Figure 5.2. Actual power curve in Germany on 7 July 2013. About 48% of the total electricity around 1:30PM was produced from solar energy at 22.4 GW. The daily solar electricity production was 197 GWh, or 23% of the total daily production. Source: EEX.
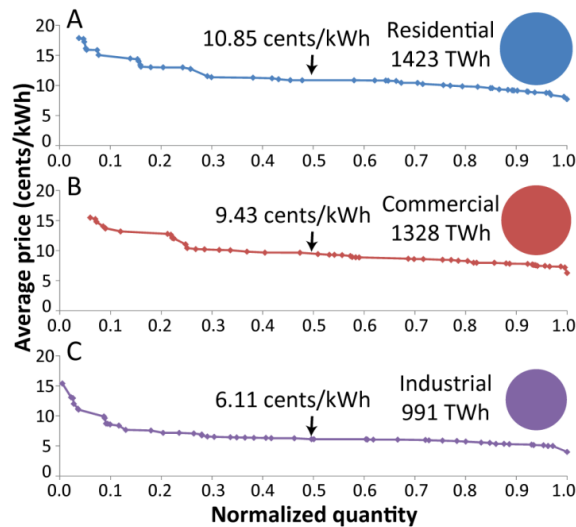
Figure 5.3. The distribution of electricity prices among the 50 U.S. states in 2011. The medium prices in the residential (A), commercial (B), and industrial (C) sectors were 10.85, 9.43, and 6.11 cents per kWh, respectively. With further cost reduction in the installed cost of solar PV system, the market size for solar PV would continue to expand, covering more states and sectors. The electricity prices in Hawaii,

ranging from 27.8-34.0 cents per kWh, are not shown in the figure. All prices are inflation-adjusted to the 2010 U.S. dollars. Source: EIA.
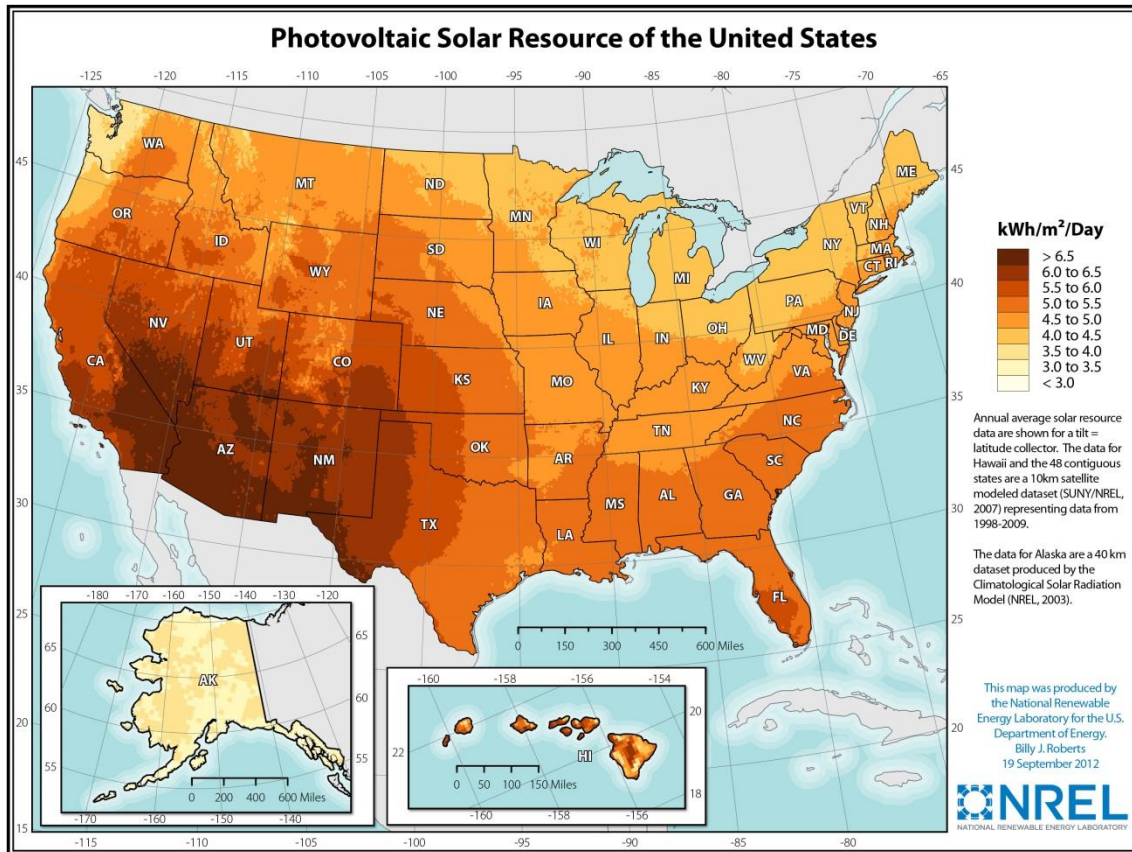
Figure 5.4. Average daily solar radiation for a surface tilted at latitude angle over a year. For a given PV system, the amount of solar radiation determines its capacity factor and affects the LCOE of PV electricity. Source: NREL.

This chapter mainly looks into two questions. First, commercial PV module efficiency testing is done at normal incidence of light of the standard AM1.5G spectra; however, during operation of installed PV systems solar irradiance is mostly neither at normal incidence nor exactly matching the AM1.5G spectra. How large would be the effect of these angular and spectral variations of solar irradiance on the system's performance? Second, the rule-of-thumb installation guideline for rooftop PV systems is to tilt at the latitude angle [168]. What is the potential for balance of system innovations to reduce the LCOE of PV electricity for a given installed cost of PV systems, by deploying these rooftop PV systems smarter?

51

5.2. Optimized Installation of Commercial Rooftop PV Systems

5.2.1. Motivations

Measured efficiency under AM1.5G spectra has been the widely accepted standard to quantify the performance of solar cells. However, the test is carried out at normal incidence of light, while the installed solar panels are subjected to solar irradiation with different angle of incidences (AOI) and spectra most of the time during actual operation. Especially when evaluating the performance improvement of different antireflection coatings on solar cells, one might need solar irradiation data including these angular and spectral variations [169] or years-long field test [170].

Optical losses from surface reflection and poor infrared absorption remain as the main bottlenecks in further improving the cost-effectiveness of today's crystalline-silicon (c-Si) solar cells, and considerable amount of research efforts have been devoted into light management for photovoltaic applications [16,19,21,22,26,27,171-173]. Solar irradiation data, which is resolved in both angle and wavelength, presents an effective and a more realistic approach to translate the measured improvement in optical properties, such as angle-resolved reflectance spectroscopy data, to gains in annual energy yield.

From the economics perspectives, installation of PV systems on residential and commercial rooftops in good sunlight locations may represent the largest PV market potential in the next 10 years, according to a 2012 McKinsey study [174]. Optimizing the installation of a given PV system can yield higher energy output and reduces the LCOE of PV electricity. To improve the energy yield under solar irradiation with daily variations in AOI, single-axis tracking [175] has been commonly used for PV power plants. While the PV systems installed on residential and commercial rooftops normally opt for fixed-tilt panel configuration, due to constrained area and maintenance concerns [176]. Simulations and observations both show that the tracking can yield 18% to 25% more in energy output and capacity factor, compared with fixed-tilt panel configurations [175,177]. Balancing between maintenance cost and energy yield, the tilt angle in a semiannually-fixed tilt configuration [178] changes twice every year, which is optimized for summer (Apr to Sep) or winter (Oct to Mar) respectively. Recognizing the necessity for regular maintenance to clean dust off solar panels [28,173,179], these infrequent changes in the tilt angle have the potential to be integrated with other regular maintenances with little increase in operating costs.

This section presents a systematic approach for optimizing commercial rooftop PV system installations, estimating energy yield using more realistic angle-and-wavelength-resolved clear sky solar irradiance data and quantifying the economic benefits. We believe that these sets of information would be important for manufacturers to assess the cost-effectiveness of a certain technological improvement, and for developers to choose the more cost-effective products for installations at a given geographic location. As the real world PV system performance will be strongly affected by geographic latitude, 3 cities varying from N30° to N45° in latitude are covered in this study to represent the typical geographic variations in the lower continental United States. The north-south difference in energy yield due to geographic locations is most

significant in winter by about 15%. In the case of rooftop installations in Berkeley, the proposed semiannually-fixed tilt configuration of solar panels is found to increase the energy yield by 5.8% over the year and up to 15.6% in peak summer days, when the electricity is typically in stronger demand and therefore of a higher value. The added value presents a market potential for such balance of systems (BOS) hardware innovations which allow semiannually-fixed tilt configuration.

5.2.2. Simulation details

The AM1.5G spectra, also known as the ASTMG173 terrestrial reference spectra for evaluating PV cell performance, are derived from the NREL's SMARTS model for a south-facing flat surface tilted at 37°, which receives sunlight after air mass (AM) of 1.5 [180]. This study uses the SMARTS 2.9.5 model to simulate daily solar irradiance data resolved in both AOI and wavelength (**Fig. 5.5**) over 12 months. All the parameters are chosen according to the ASTMG173 standard spectra, except for the latitude and tilt angle of the installed PV system. The resolution of the simulated solar irradiance data is 1 degree in the AOI and 10 nm in the wavelength.
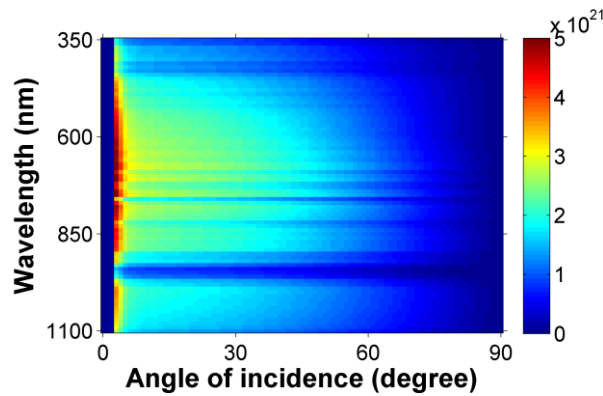
Figure 5.5. Average daily solar irradiance data in September for a surface tilted at 37.73⁰ in Berkeley.

To investigate the effect of angular and spectral variations on energy yield, External Quantum Efficiency (EQE) data for c-Si PV modules, also resolved in both AOI and wavelength, are obtained by combining the Internal Quantum Efficiency (IQE) data from the literature (**Fig. 5.6**) and the transmittance data from modeling the glass/EVA/silicon interfaces [172,181] by ray tracing technique in multilayers [182,183]. The reflectance and transmittance after adding the jth layer, R_{n+j} and T_{n+j}, are obtained from the reflectance and transmittance of previous n layers, R_n and T_n, according to **Eqs. 5.2 & 5.3**.

$$R_{n+j} = R_n + \frac{R_j T_n^2}{1 - R_n R_j} \qquad\qquad\qquad \textbf{Equation 5.2}$$

$$T_{n+j} = \frac{T_n T_j}{1 - R_n R_j} \qquad\qquad\qquad\qquad \textbf{Equation 5.3}$$
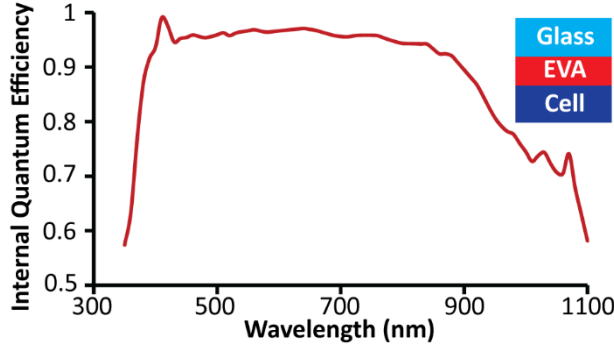
Figure 5.6. IQE profile at normal incidence for the PV cell from literature [184]. The inset shows the architecture of a PV module used in the optical modelling for reflectance and transmittance at the module level.

The power output of the PV module is 182 W/m^2 under normal incidence of sunlight with AM1.5G spectra. The difference in optical response between cell and module is mainly accounted by strong angular dependence of reflection at the air/glass interface and strong UV absorption by the encapsulant in the PV module (**Fig. 5.7**).
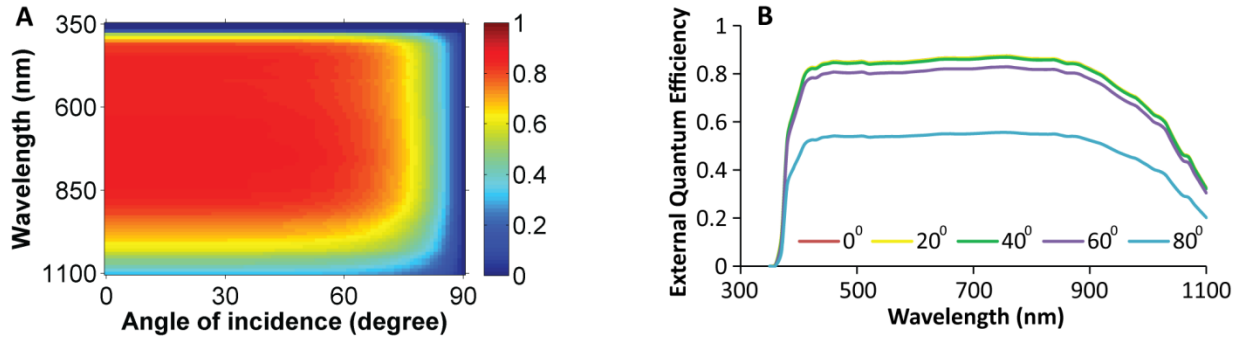
Figure 5.7.   Angle-and-wavelength-resolved EQE for the PV module. The EQE map (A) shows the angular and spectral variations in efficiency. EQE profile at selected AOIs (B) highlights the significant efficiency decrease at short wavelength and large AOI.

The total number of electrons collected in one day is obtained by multiplying the daily solar irradiance I (**Fig. 5.5**) with the EQE data (**Fig. 5.7A**), both of which are resolved in AOI θ and wavelength λ.   In order to present the energy output results in a more meaningful form (kWh/m2), the presented daily energy yield EY (**Eq. 5.4**) is the product of total collected charges and a working voltage Vop of 0.527 Volts [184].

$$EY = \sum_{\theta,\lambda} I_{\theta,\lambda} \cdot EQE_{\theta,\lambda} \cdot V_{op}$$ **Equation 5.4**

5.2.3. Angular and spectral variations from the standard test spectra

The AM1.5G standard spectra are considered to be a reasonable average for the lower 48 continental U.S. states. However, there are clear seasonal variations in the daily average solar spectra (**Fig. 5.8**). Normalized to the same power density in the interested wavelength range (350nm – 1100nm), winter spectrum (Dec) is significantly red shifted with a higher weightage of long-wavelength photons; while summer spectrum (Jun) is somewhat blue shifted with a higher weightage of short-wavelength photons.
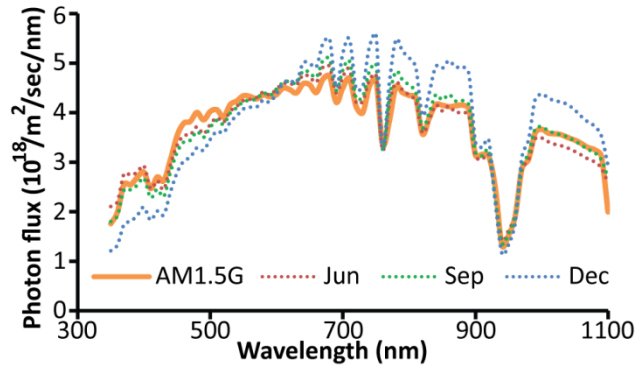
Figure 5.8. Seasonal variations in the normalized solar spectra for a surface tilted at 37.73⁰ in Berkeley.

The angle-and-wavelength-resolved solar irradiance is able to capture both the angular and spectral influences on power output, compared with using standard testing spectrum. **Table 5.1** compares the power output of the PV module between these two approaches. Accounting for only the spectrum difference, power output under the normalized Dec spectrum could be 4.7% higher than using the AM1.5G spectrum, as the Dec spectrum is significantly red shifted. For the same reason, the normalized Dec spectrum turns out to produce more power than the normalized Jun spectrum, as the lower weightage of short-wavelength photons in the Dec spectrum reduces efficiency losses from thermalization of excited charge carriers (see **Section 2.2** for the working principle of a silicon PV cell).

Table 5.1. Angular and spectral effects on power output for a PV module tilted at 37.73⁰ in Berkeley.

(W/m2)	Jun	Sep	Dec
Angular & Spectral	174.1	179.4	188.5
Spectral	181.3	184.0	190.6
AM1.5G	182	182	182

Comparing "Angular & Spectral" and "Spectral" in **Table 5.1**, the power output could be 1.1% - 4% less after also accounting for angular dependence of EQE. The angular effects of solar irradiation and EQE are most significant in June, when about 16% of daily solar irradiance is at large AOIs (>60⁰) (**Fig. 5.9**). When tilted at the latitude angle (LA) in December, only 4% of daily solar irradiance is at these large AOIs, and the angular effect is negligible. As the light refraction

in the glass and EVA layers reduces the AOI at the Si interface (**Fig. 5.10A**), the angular dependence of the module's EQE (**Fig. 5.7**) is only significant at these large AOIs (>60⁰).
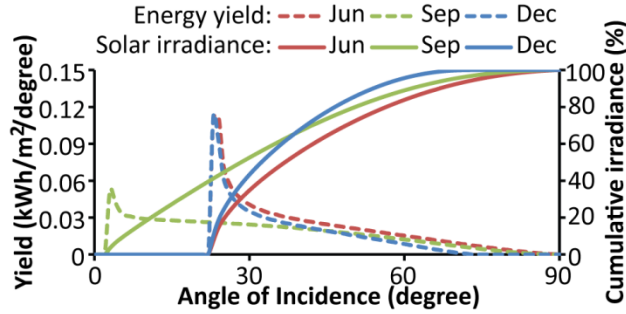
Figure 5.9. Angular distribution of daily energy yield and incident solar irradiance for a surface tilted at 37.73⁰ in Berkeley.
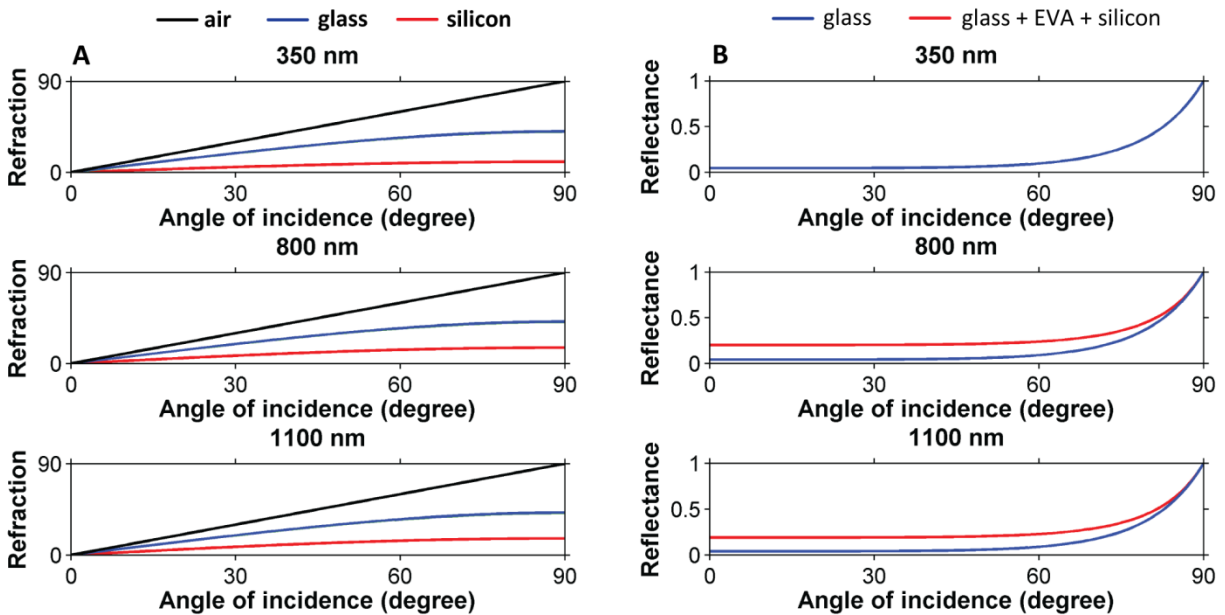
Figure 5.10. Strategies for reducing light reflection from PV modules. Due to refraction of light (A), the AOI at the EVA/silicon interface is much smaller than the AOI at the air/glass. Reflection (B) is dominated by the air/glass (EVA/silicon) interface at large (small) AOIs.

For reducing light reflection from the PV module at large AOIs, innovations should be focus on the air/glass interface, as the AOI after encapsulant at the solar cell surface is significantly smaller (**Fig. 5.10B**). As shown in **Fig. 5.9**, most of solar irradiance is at small AOIs (<60⁰). Therefore, more significant efficiency boost could be realized by adding a more optically suitable encapsulant layer (with higher refractive index than EVA) between glass and silicon to reduce light reflection at small AOIs.

5.2.4. Energy yields of different panel tilt configurations

The NREL SMARTS 2.9.5 is used to generate angle-and-wavelength-resolved solar irradiance data for the 3 U.S. cities covered in this study and for a combination of panel tilt angles, where the selections of tilt angles are based on the results from previous studies [177,178]. Shown in **Table 5.2**, the rule-of-thumb for PV panel orientation (tilted at an angle equals to the latitude and facing south) is optimized for neither summer nor winter times, but it usually yields the highest energy output per m^2 over the whole year. Decrease (increase) in tilt angle from the latitude angle (LA) is required to optimize energy yield for summer (winter). Moreover, the difference in energy yield for a given PV system at different latitudes, installed with optimized tilt angles, is much smaller in summer (1.4%) than that in winter (15%), when comparing northern U.S. cities with southern ones. The large energy yield difference in winter would increase the LCOE for northern cities.

Table 5.2. Average daily energy yield of PV module (kWh/m2) for 3 groups of tilt angles.

Tilt angle = Latitude +		Austin, TX (N 30.17⁰)		Berkeley, CA (N 37.73⁰)		Minneapolis, MN (N 44.96⁰)	
		Summer	Winter	Summer	Winter	Summer	Winter
Year	0	1.500	1.370	1.505	1.287	1.499	1.174
	-4	1.541	1.335	1.534	1.256	1.527	1.143
	-8	1.559	1.300	1.563	1.208	1.549	1.110
	-12	1.577	1.253	1.580	1.180	1.565	1.072
Summer	-24	1.601	1.065	1.590	1.018	1.579	0.933
	-26	1.599	1.043	1.593	0.986	1.577	0.908
	-28	1.589	1.003	1.589	0.952	1.572	0.875
	-30	1.583	0.967	1.583	0.918	1.572	0.844
Winter	10	1.410	1.432	1.406	1.343	1.396	1.217
	12	1.380	1.446	1.377	1.355	1.382	1.232
	14	1.338	1.442	1.361	1.361	1.357	1.227
	16	1.331	1.453	1.334	1.355	1.325	1.235

Figure 5.11 plots the 12 months' breakdown for the Berkeley data in **Table 5.2** for a few optimized tilt configurations, which result in the maximum energy yield during the summer, the winter, or the whole year. In a semiannually-fixed tilt configuration where the PV panels are tilted at two different angles in winter (blue) and in summer (red), the total annual energy yield would be more optimized than all 3 cases shown in **Fig. 5.11**. It is worth noting that around April and September, the energy yield difference between the summer-optimized tilt configuration and the winter-optimized tilt configuration is relatively insignificant. Therefore, the servicing of PV panels has a large time window for tilt angle changes in late March and September. Another observation is that increasing tilt angle in winter to larger than latitude angle is less effective in increasing energy yield, compared with decreasing tilt angle in summer.

Considering shading and the economics of ground cover ratio [*176*,*185*], the semiannually-fixed tilt configuration, in practice, may choose a tilt angle in winter, not optimized for energy yield per area of PV panels but for energy yield per area of constrained rooftop.
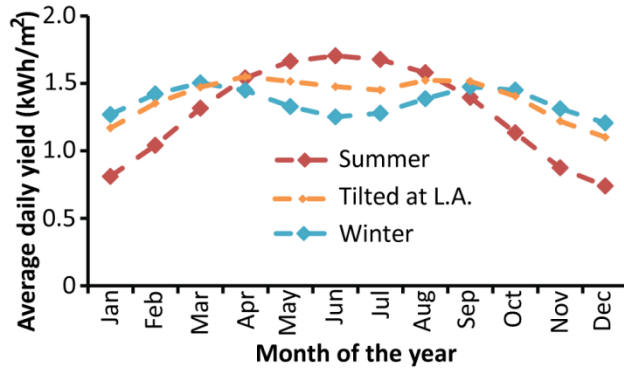
Figure 5.11. Average daily energy yield (Jan. to Dec.) in Berkeley for selected tilt configurations.

The key advantage of the semiannually-fixed tilt configuration, compared with fixed-tilt at the LA is a significant boost in energy yield in summer months (**Fig. 5.11**), which is mainly attributable to improved angular distribution of solar irradiance (**Fig. 5.12**). Compared with a flat horizontal surface, the rule-of-thumb fixed-tilt configuration shifts the angular distribution of sunlight in June towards larger AOIs, while a smaller tilt angle in June in the semiannually-fixed tilt configuration further shifts the distribution towards smaller AOIs and hence increases energy yield in summer.
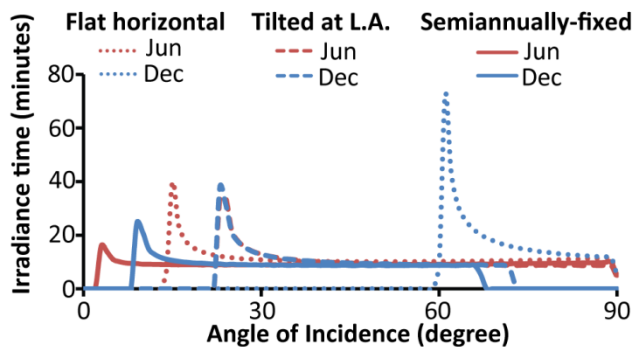
Figure 5.12. Angular distributions of solar irradiance time in Berkeley between summer and winter by different configurations.

The semiannually-fixed tilt configuration is more attractive compared with conventional rule-of-thumb rooftop PV system installations, in terms of performance and economics. **Table 5.3** highlights some key performance and economic results for a given PV system in Berkeley, where the electricity is of the highest rates and generated from the cleanest sources among the 48 states (**Fig. 5.13**). The electricity rate is assumed to be $0.205/kWh in summer (May to October) and $0.144/kWh in winter (November to April). In terms of energy yield, the capacity

factor (CF) is improved by an average of 5.8% over the year. As the summer electricity rate for commercial usage is typically higher than winter rates, the 15.6% increase in July's CF alone would contribute a present value of $19.55 at a discount rate of 5% and over a lifetime of 25 years. Therefore, innovations in the balance of system, which allows such a semiannually-fixed tilt configuration, are likely to increase the net present value of the PV system, if the incremental cost is well below $74/m^2.

Table 5.3. The performance and economics of semiannually-fixed tilt configuration for the PV module in Berkeley.

	Present value of yield improvement	Ratio of Added value to Installed cost	Capacity factor	
			Fixed tilted at L.A.	Semi-annually fixed
Year	$74.25	8.16%	0.320	0.338
Summer	$45.96	5.05%	0.345	0.365
July	$19.55	2.15%	0.332	0.384
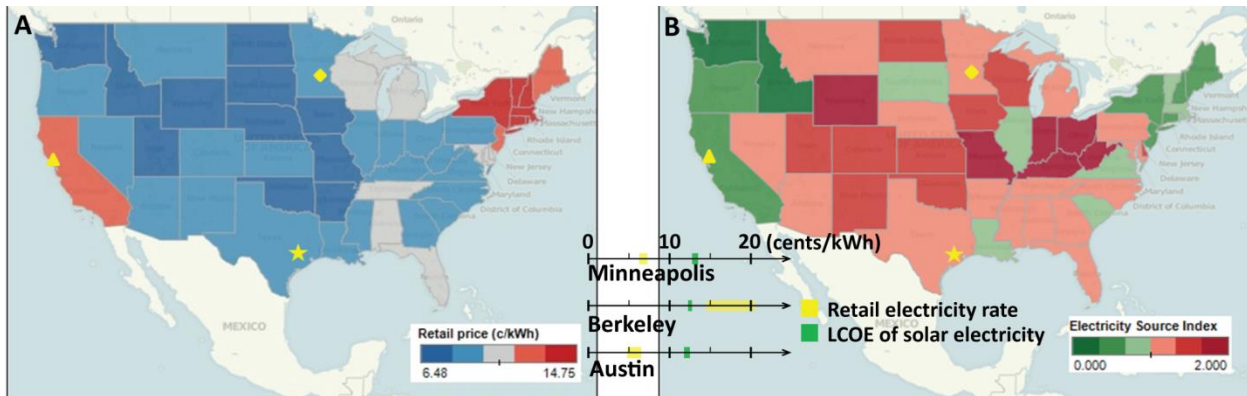
Figure 5.13. Grid parity assessment in Austin, Berkeley, and Minneapolis. The inset shows that the LCOE of solar electricity in Berkeley is lower than the retail commercial electricity rate, where California is among the states with highest electricity rates (A, EIA's 2012 February monthly data) and of the cleanest sources for electricity generation (B, EIA's 2010 yearly data). For computation of the electricity source index, coal, natural gas, nuclear, and renewables are weighted as 2.0, 1.0, 0, and 0, respectively.

To highlight the effect of solar irradiance on the economics of solar electricity, the LCOE is solely based on a cost of $5/W, without accounting for other geographically varying factors such as maintenance cost, tax benefits, and subsidies. As a result, the presented LCOE tends to be the lower-bound value. It is also worth noting that the capacity factor in this study is the upper-bound value, as the clear-sky model neglects the effect of clouds. Nevertheless, the energy yield ratio between the semiannually-fixed tilt configuration and the fixed-tilt configuration is likely to be little affected, as both tilt configurations would be affected by clouds equally.

6. Innovation-Focused Policy Framework for TW-Scale PV Deployment

Previous chapters have reviewed innovations in the photovoltaic (PV) science, manufacturing, and installation, which all have one common goal: to reduce the cost of PV technology and make it an affordable clean energy source on the global scale. These dramatic technological innovations over the past decades were enabled and supported by various policy instruments, ranging from regulation and subsidies to research & development (R&D). These policy instruments in the PV sector can be broadly categorized into two approaches: technology-push which directly supports technological progress such as public R&D funding, and demand-pull which creates or expands the market for PV installations such as tax credits.

This chapter will first review a few key policy instruments in the global PV industry, and discuss some of the major policy innovations. The second section measures the innovation pace in terms of patent applications in PV technologies over the past two decades, examines the key policy lessons from the painful turmoil in the recent few years, and highlights the role of innovation in delivering the long-term promises of PV technology in meeting growing energy demand and mitigating climate change. The last section proposes an innovation-focused policy framework in building a sustainable global PV industry [*160*].

6.1. Demand-Pull and Technology-Push Policy Instruments

PV technology was an expensive niche energy source only for satellite applications, hallmarked by the Bell Lab's launch of the Telstar satellite with PV cells in 1962. Various energy policy instruments have been devised since then to foster research and innovation in PV technology. Without these major policy innovations, it would be impossible to imagine a PV industry for terrestrial power generation with about 38 GW/year installations [*10*] and over $100 billion/year market size in 2013.

Net metering [*186*], which allows consumers to offset their electricity bill with self-generated electricity output, was first enabled in the United States by the Public Utility Regulatory Policy Act (PURPA) of 1978. This law essentially provides the regulatory assurance for the PV technology to compete with retail electricity rates, by requiring the utility companies to purchase electricity from independent generators at "avoided cost" [*187*]. According to the Database of State Incentives for Renewables & Efficiency (DSIRE) [*188*], more than 40 states, the District of Columbia, and 4 territories in the United States have implemented net metering policies in 2014.

Renewables portfolio standard (RPS), which typically sets a series of milestones for the share of renewables in the electricity market, is a state-level mandate, within which a specific portion can be carved out for solar energy due to its higher cost compared with other renewables such as wind energy. For example, New Jersey has an ambitious target of providing 4.1% of retail electricity sales with PV systems by 2028 [*188*]. Together with net metering, RPS

opens up the market for distributed PV deployment and utility-scale PV generation through regulations [189,190]. According to the DSIRE, 29 states, the District of Columbia, and 2 territories in the United States have implemented RPS policies in 2014.

Financial incentives, in the form of government subsidies, have spurred the demand for PV installations dramatically in the past decade, together with the cost of PV modules declining from about $5.0/watt in 2000 to $0.70/watt in August 2014 [191]. In the United States, the most significant subsidy for PV products is the federal investment tax credit (ITC). The Energy Policy Act of 2005 enacted a 30% ITC for residential and commercial solar energy systems, where 30% of the system cost can be deducted from the federal tax, from January 1 2006 to December 31 2007. The ITC was then extended in 2006 and in 2008 to be effective till December 31 2016. However, the ITC would commonly require tax equity, which could be a significant cost factor of the installed PV systems [192]. To stimulate the deployment of PV projects, the ITC was temporarily replaced by the cash grant enacted by the American Recovery and Reinvestment Act of 2009 for PV system constructions that commenced by 2011 [193]. The 30% tax credit could also present an unintended possibility for overstating the PV system price (for instance, there was a high-profile U.S. Treasury investigation of SolarCity in 2012 right before its Initial Public Offering [194]).

One policy innovation to discourage overstating system prices is Japan's "Residential Solar Power Support Measure", which offers cash subsidy to residential PV systems (<10 kW). The subsidy rate is inversely related to the system price: a subsidy of $0.20/W for prices lower than $4.10/W, a subsidy of $0.15/W for prices higher than $4.10/W, and no subsidy for prices higher than $5.00/W [195]. Similar approaches like a moving price ceiling, which will be periodically reviewed with the market development, should be integrated with the type of subsidies, where the amount of subsidy is proportional to system price.

The incentives for purchasing more cost-effective PV system is stronger under the feed-in tariff (FiT) scheme [196,197], where the subsidy is directly tied to the electricity output ($/kWh) for a certain number of years (typically 20 years). Lower prices of PV systems will lead to a higher rate of financial return. Germany's FiT program has made Germany the world's top leader in deploying PV technology, with about 35 GW of total installed capacity by the end of 2013 [10]. The main issue with Germany's FiT program is the runaway rapid expansion in PV deployment and the associated cost burden on retail electricity prices in the form of EEG surcharge. In order to slow down the PV deployment to 2.5 – 3.5 GW/year, several EEG amendments [198,199] to reduce PV FiT rates based on the previous installation volume have been passed by the German lawmakers since 2009 (**Fig. 6.1A**), which in turn "stimulated" demand as installers expected the FiT rates to decline rapidly and rushed to take advantage of the current attractive FiT rates (**Fig. 6.1B**).
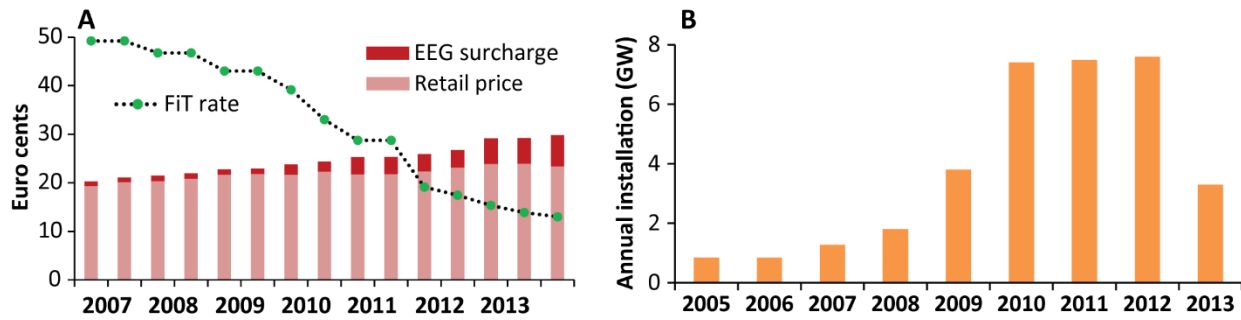
Figure 6.1. FiT-driven PV deployment in Germany. The FiT rates have been declining while the retail electricity prices have been rising for residential consumers in Germany, where the red portion of the price is the EEG surcharge to fund the FiT payment (A). Since 2009 several EEG amendments have been made to rein in the rapid expansion in PV installations (B). Source: Eurostat and EPIA.

In terms of technology-push policies, public R&D in PV has also enjoyed innovations in the recent decade. For example, a U.S. national program, the SunShot Initiative, has been created to focus on funding the most innovative ideas in making PV technology more cost-effective. Innovative R&D models such as the U.S. PV Manufacturing Consortium was funded in 2011 to promote R&D collaboration and technology transfer among PV manufacturers, which borrowed the pre-competitive R&D model from the semiconductor industry.

In the ideal picture, private R&D can be also stimulated by the "demand-pull" policies in a vibrant PV industry through market-driven innovation: PV manufacturers are thriving and re-investing their profits into R&D. An expanding market incentivizes all innovations that aim to further reduce the manufacturing cost. The fundamental long-term needs to deploy cost-competitive, low-carbon energy sources continue to attract private capital to commercialize promising innovations. All these innovation sources together drive the cost of deploying solar PV towards grid parity in a growing number of markets.
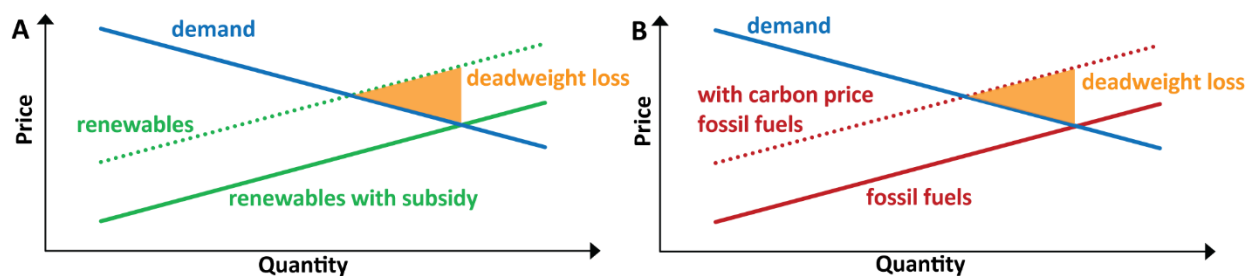
Figure 6.2. Economic deadweight loss from carbon emissions and subsidy to renewables. In the current policy framework, overconsumption of energy (both renewables and fossil fuels) leads to a deadweight loss. The optimum operating point is to replace the patchwork subsidies to renewable energy (A) with market prices on carbon emissions (B).

Pricing carbon emissions globally in the form of either a carbon tax or a cap-and-trade program is a direct and effective way to correct the environmental externalities of fossil fuels and renewables. In a simple theoretical framework (**Fig. 6.2**), subsidizing renewable energy instead of pricing carbon emissions leads to overconsumption of energy and an associated deadweight loss. Moreover, a coordinated global program in pricing carbon emissions, though a challenging policy goal, may provide better sustainability and certainty than the current patchwork approaches towards renewables through regulations and subsidies.

6.2. Policy Lessons from the Rapid Development in the Global PV Industry during 2000-2013

The global photovoltaic (PV) market has undergone a dramatic evolution in the recent decade, expanding from 0.3 gigawatts (GW) of annual installations in 2000 to 38 GW in 2013 [*10*]. This evolution has spurred manufacturing scale-up with GW-size solar panel factories. The innovation pace has been impressive, with patent applications growing by seventeenfold between 2000 and 2011, from 138/year to 2344/year. Accompanying with the impressive scale-up and technological innovation, the inflation-adjusted prices of crystalline-silicon (c-Si) PV modules have declined from $5.0/watt in 2000 to as low as $0.72/watt in September 2013 [*191*].

Billions of dollars in deployment incentives have been spent each year to support the market for solar PV (**Fig. 6.3**), particularly in the Germany via feed-in tariffs (FiT) and in the U.S. via tax credits. These "demand-pull" policies are intended to create a vibrant PV industry through market-driven innovation. The recent overcapacity in the PV module production and the resulting oversupply, however, have caused PV modules being sold at unsustainably low prices and pushed almost all major PV manufacturers into financial losses in 2011 and 2012 (**Fig. 6.4**). There are also signs of cutback in R&D spending among these major PV manufacturers (**Fig. 6.5**).
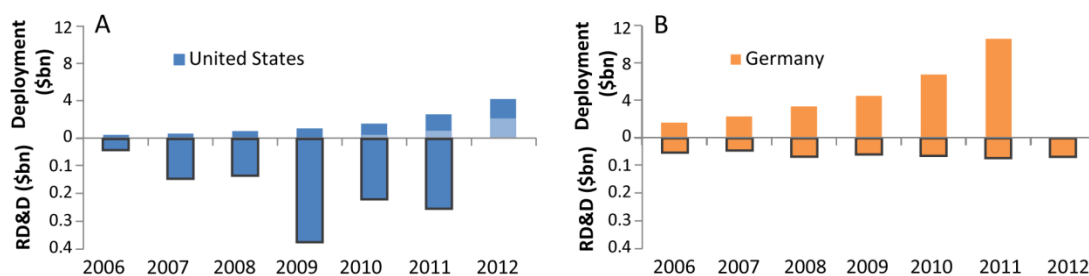
Figure 6.3. Funding allocation between public R&D and deployment for solar PV. The cash grant (from the American Recovery and Reinvestment Act), as part of the deployment funding, is highlighted in lighter color. The R&D budget includes funding for demonstration projects. All prices are inflation-adjusted to the 2010 U.S. dollars. Source: BNetzA, IEA, LBL, and U.S. Treasury.
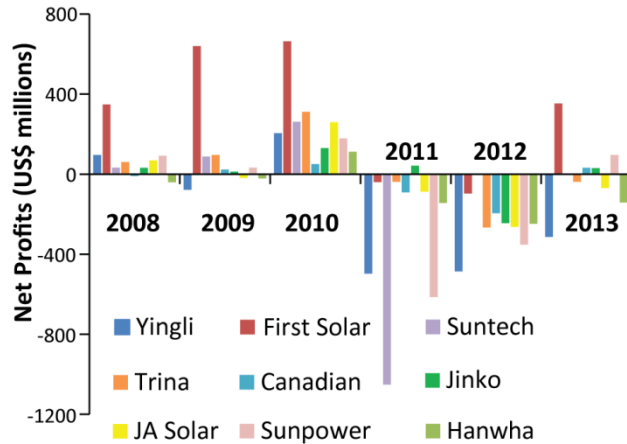
Figure 6.4. Net profits (losses) of 9 major U.S.-listed PV manufacturers during 2008-2013. The 2013 financial results have shown signs of industry-wide recovery from the darkest periods during 2011-2012. Source: U.S. SEC.
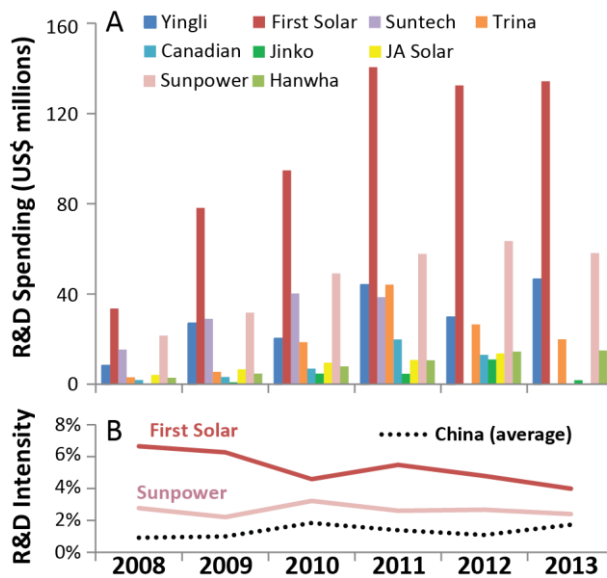
Figure 6.5. Corporate R&D from 9 major U.S.-listed PV manufacturers during 2008-2013. The corporate R&D spending (A) is mostly increasing during 2008-2011 accompanying with increasing sales revenue, but shows signs of declining in 2012 and 2013. Different from the other 8 manufacturers, First Solar is specialized in thin film PV modules and system integration, whose business model enables First Solar to command a notably higher profit margin. The R&D intensity (B) is measured as current year's R&D expense as a percentage of previous year's sales revenue. The 7 China-based PV manufacturers on average have invested 1.33% of their sales revenue into R&D during 2008-2013. Source: U.S. SEC.

In this section we will examine a set of the PV industry's key metrics on innovation, manufacturing, and market. Insights will be developed from the dataset to form a policy framework for building a sustainable PV industry.

6.2.1 Data and methods

We have assembled a comprehensive dataset from 2000 to 2013 for the global PV industry from publicly available sources, including PV installation and manufacturing, research & development (R&D), deployment incentives, and company-level financial performance for major PV manufacturers. For c-Si wafer-based PV modules, the price and market size data are obtained from the Bloomberg New Energy Finance [200] and used in the learning curve models. For First Solar's thin film PV modules, the cost and quarterly production data are obtained from the company's quarterly reports.

There are three common proxies to measure innovation: R&D spending, literature counts, and patents [201]. As we are interested to examine the relationship between innovation and cost reduction in PV technology, the patent approach is chosen to measure innovation output that is closely related to industrial applications [202]. The main limitation of patents as the proxy for innovation output is patent quality, where claims, citations, and number of protected countries have been previously explored to weight the economic value of patents [203]. Furthermore, the overall patent quality could differ significantly across major patent offices [204]. Therefore, this study measures innovation by the number of Patent Cooperation Treaty (PCT) patent applications through the World Intellectual Property Organization (WIPO), a well-established proxy for benchmarking a country's innovation capacity [205]. PCT patent application serves as a proxy for high-value innovation output, as it is a cost-effective approach for patents seeking international protection.

We collect and process the patent data from the WIPO PatentScope database. We are interested in using the same set of PV patent data to analyze the cost reduction through innovation, and to understand the dynamics among innovation, manufacturing and market forces. Therefore, we choose the keywords approach to identify patents focused on PV applications. PV PCT applications are obtained by searching keywords "photovoltaic", "solar cell", "solar module", or "solar panel" in the title and abstract of the applications. C-Si PV PCT applications are the PV PCT applications containing keyword "silicon" but no "amorphous". First Solar's PCT applications used in the learning curve model have excluded applications related to PV system installation. The patent data has been refined using the patent classes approach with technology categories defined in the International Patent Classification (IPC) Green Inventory (**Table A2.1**). All applications are sorted by country according to the applicant's address. The patent data is also sorted by year according to the priority date for quantifying innovation in the learning curve model, or according to the international filing date for measuring patenting activities.

A two-step regression procedure is then adopted to solve the co-linearity issue in the two-factor learning curve model. As both the cumulative PCT applications (T_i) and the annual installations of c-Si PV modules (Q_i) have been increasing in our time frame, the correlations are removed by using the residual variable η_i in **Eq. 6.1** and Q_i to explain the price (P_i) in **Eq. 6.2**.

$$T_i = \alpha_0 + \alpha_1 \log Q_i + \eta_i \qquad\qquad \textbf{Equation 6.1}$$

$$\log P_i = \theta_0 + \theta_1 \log Q_i + \theta_2 \eta_i + \epsilon_i \qquad \textbf{Equation 6.2}$$

The final model is presented in **Eq. 6.3**, or an equivalent form in **Eq. 6.4**. The learning rate (LR) for economies of scale Q_i is defined as cost reduction per doubling in scale. The LR for innovation T_i in this study is defined as cost reduction per 100 patent applications. A summary of the key regression results can be found in **Tables A2.2** and **Table A2.3** in the appendix.

$$\log P_i = \beta_0 + \beta_1 \log Q_i + \beta_2 T_i + \epsilon_i \qquad \textbf{Equation 6.3}$$

$$P = \left(10^{\beta_0} \middle/ Q_i^{-\beta_1}\right)\left(10^{\beta_2}\right)^{T_i} \qquad \textbf{Equation 6.4}$$

6.2.2. Cost-effective policies for further cost reduction

We first estimate the range of cost-reduction potentials in PV modules from projections in three learning curve models. **Table 6.1** estimates the timing and the learning investment for various c-Si PV learning curve projections. The conventional learning curve model (**Eq. A2.1**) for c-Si PV modules has been widely referenced to support policies that rely on a cost-reduction strategy through rapid market expansion, where the average selling price (ASP) of PV modules is projected to decline with increasing cumulative installations [92,206]. As the market grows, production of PV modules benefits from both economies of scale and "learning", where accumulated operating experience leads to innovation and cost reduction through both learning-by-doing and learning-by-searching [207]. However, the LR is known to vary depending on the timeframe of the regression analysis (**Fig. 6.6A**), and this uncertainty in LR will significantly affect the projected timing and cost of reaching the cost-reduction milestones [208,209] and GHG mitigation targets. As detailed in **Table 6.1**, "demand-pull" polices, based on this conventional learning curve model, would experience a range of learning investment with differences by an order of magnitude.

Table 6.1. The timing and cost (learning investment) of various cost-reduction scenarios for c-Si PV modules to reach a price of $0.5/W.

	Market growth at 30%/year		No market growth	
	Timing	Cost (US$ bn)	Timing	Cost (US$ bn)
Conventional (LR=20.9%)	2023	220	2081	252
Conventional (LR=15.2%)	2034	3,576	Not within the 21st century	
Economies of scale	2043	24,837	N.A.	
Innovation (2005 level)	2031	1,616	2041	253
Innovation (2010 level)	2019	72	2019	45
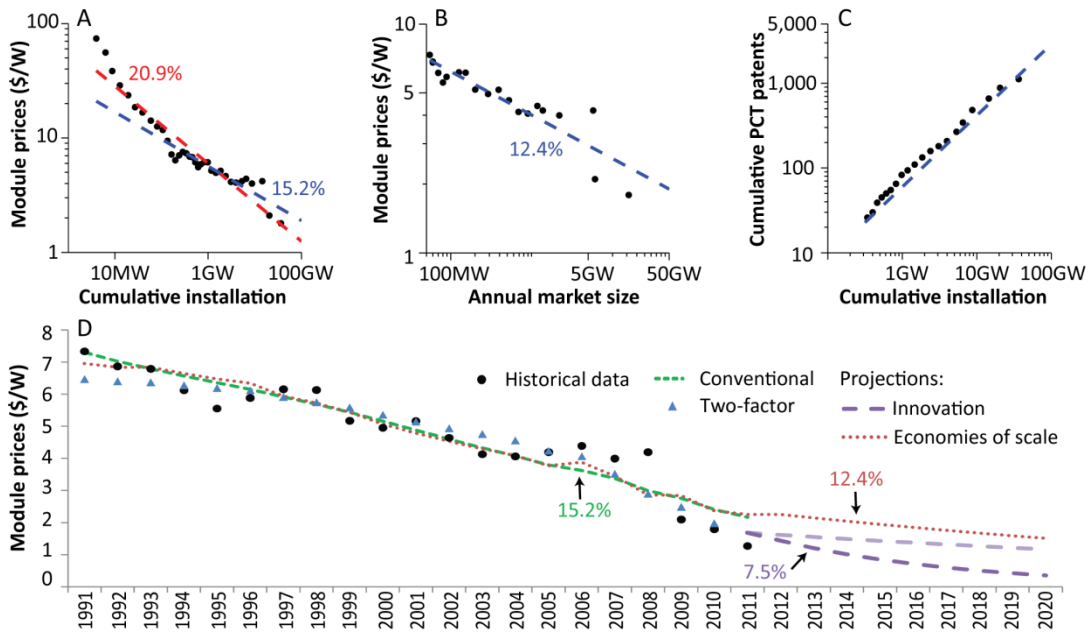
Fig. 6.6. The effect of economies of scale and innovation in the c-Si PV learning curve. Plots A-C show the log-log linear fit of the three models: conventional, economies of scale, and learning. The various LRs are labeled in the corresponding color. The LR for the conventional model during 1976-2010 is labeled in red (A). The upper boundary of the "innovation" projections in the two-factor model (D) is based on a lower level of innovation in 2005 and assumes no market expansion beyond 2012, while the lower boundary is based on a higher level of innovation in 2010 and a market growth rate of 30%/year. See **Table A2.2** in the Appendix for detailed regression results. All prices are inflation-adjusted to the 2010 U.S. dollars. Sources: BNEF and WIPO.

Figure 6.6 highlights the "economies of scale" and "learning" components of the conventional model for c-Si PV modules separately. The "economies of scale" model (**Eq. A2.2**) neglects the "learning" component, and assumes that cost reduction can be fully explained by scaling up the market size. In the projection for c-Si PV in the "economies of scale" model, a target module price of $0.5/W as set by the U.S. SunShot Initiative [88] would require an annual market size of 56 TW (**Table A2.2**) and an estimated learning investment of US$ 25 trillions (**Table 6.1**). The policy implication is that "demand-pull" policies focusing on further market scale-up is likely to be unrealistic given the total market potential and the most expensive approach to achieve the SunShot target price.

The "learning" component in the conventional model is reflected in the strong correlation between market size and innovation for c-Si PV technology (**Eq. A2.3** and **Fig. 6.6C**). We conceptualize the overall mechanism underlying this phenomenon as market-driven innovation: besides enabling learning-by-doing, market expansion incentivizes R&D activities which are aimed at creating commercial value. An expanding market with growing revenue supports and encourages manufacturers' R&D activities, and incentivizes commercialization of important laboratory research results [210].

A two-factor model (**Eq. A2.4** and **Eq. A2.5**) is constructed to make explicit the cost-reduction effect of scaling from that of innovation [207,211]. Compared with the other two models, the two-factor model successfully captures the steeper decline in c-Si PV module prices during 2009-2011 (**Fig. 6.6D**), attributing it to a notably higher level of innovation activities during the corresponding period than previous years (**Fig. 6.7**). Among the different projections in **Table 6.1**, high level of innovation is not only the most promising approach to reach the SunShot goal by 2020, but also presents huge savings in required learning investment. Therefore, balanced fund allocation between R&D and deployment, with significant increases in R&D funding from the current level (**Fig. 6.3**), is likely to be a more efficient approach in further reducing the cost of PV technology.
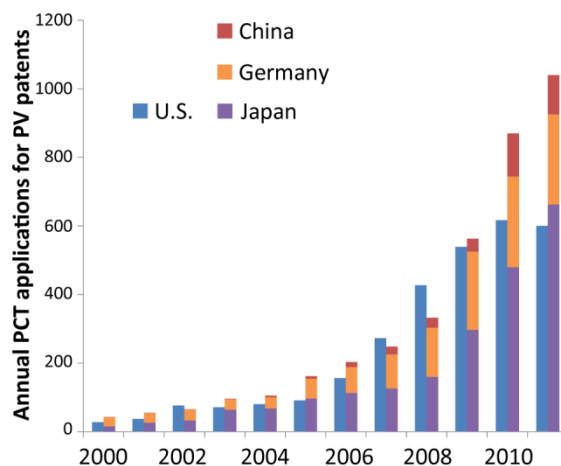
Figure 6.7. PCT applications for PV-related patents by international filing date during 2000-2011. The patent applications are sorted by year of the international filing date (x-axis). Rapid increase in PCT applications have been observed in all four countries during 2000-2010. Together with wind, PV technology has experienced the most rapid growth in patenting activities among the renewables since the 1990s [212]. Slowdown in patenting activities has been observed in 2011 for the U.S., China, and Germany. Despite being the top manufacturer and the top market for PV modules, the number of PCT applications for China and Germany in 2011 were only 19% and 44% of the U.S.', respectively. The four nations together represent about 74% of the world's total PV PCT applications in 2011. Source: WIPO.

Based on similar analysis for First Solar's thin film PV modules (**Fig. 6.8**), innovation without further expanding production scale is projected to bring the module cost to $0.4/W (or a module price of $0.5/W with a 20% gross margin) by 2019. Although the "economies of scale" model with a growth rate of 30%/year is projected to also achieve the cost target in about a decade, innovation in utilizing Tellurium is necessary for sustaining the materials supply in this scale-up [94,95].
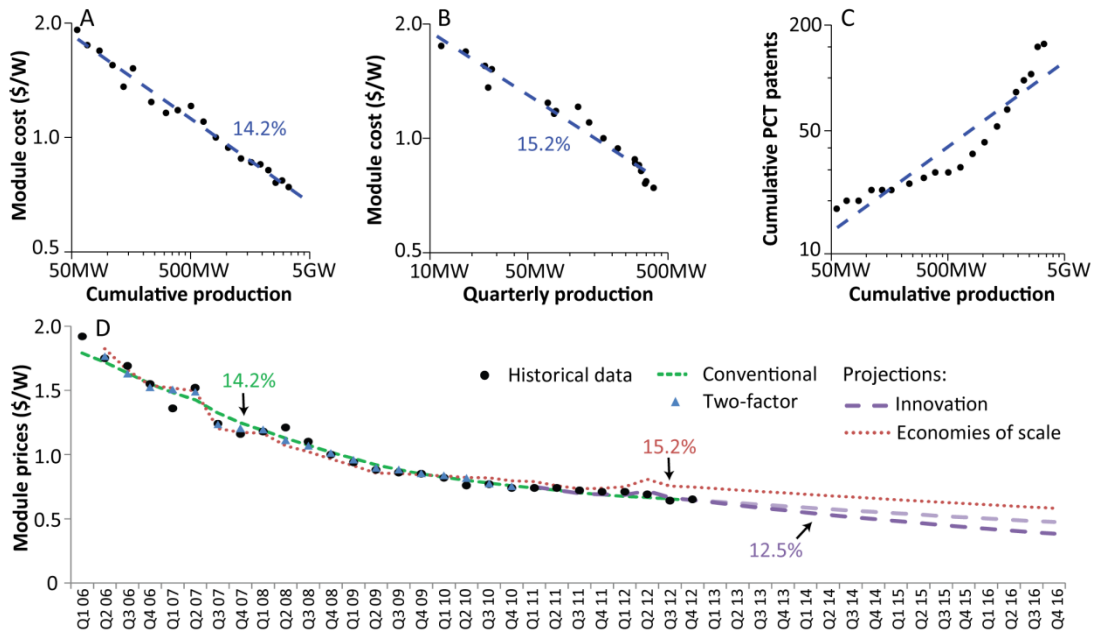
Figure 6.8. The learning curve models for the First Solar's thin film PV modules. Plots A-C show the log-log linear fit of the three models: conventional, economies of scale, and learning. Assuming no further production expansion, the upper and lower boundaries of the "innovation" projections in the two-factor model (D) are based on the level of innovation in 2011 and 2010, respectively. See **Table A2.3** in the Appendix for detailed regression results. All prices are inflation-adjusted to the 2010 U.S. dollars. Sources: BNEF, First Solar, and WIPO.

It is important for the policy community to recognize that the primary driving force underlying the reduction in PV module cost has evolved over time, from module efficiency gains in the early stage of PV technology to economies of scale [*213*], which exhibits diminishing returns with further scaling. The global PV market has expanded from 0.3 GW/year in 2000 to 38 GW/year in 2013, and further expanding the market size at such rates could be difficult. For example, with more than US$10 billions spent each year as deployment incentives for PV since 2011, Germany has revised its incentive programs to aim for a lower level of annual PV installations at 2.5-3.5 GW, which is a significant reduction compared with the annual market size during 2010-2012. For both the c-Si PV modules and the First Solar's thin film PV modules, innovation-focused cost-reduction strategies are not only more effective but also present cost-saving opportunities in terms of required deployment subsidies. The specific challenges and opportunities for innovation in PV technology have been identified in a number of previous studies [*214-218*] and in previous chapters.

6.2.3. Promoting innovation with the "technology-push" and "demand-pull" policies

The progress of developing and deploying PV technology can be greatly impeded by market failures associated with innovation and carbon emissions [*219*]. Therefore, policy intervention is necessary to account for these externalities. Weather catastrophes have caused insurers an

average of US$ 50 billions/year [220], and extreme weather events are projected to become more frequent as the global mean temperature rises [221]. Most importantly, any effective energy policies in mitigating energy-related CO_2 emissions will have to accommodate the developing countries' growing needs for affordable energy sources (**Fig. 1.1**). Therefore, subsidizing the development of clean energy into cost-competitive energy sources is essential for deploying clean energy and mitigating climate change on the global scale.
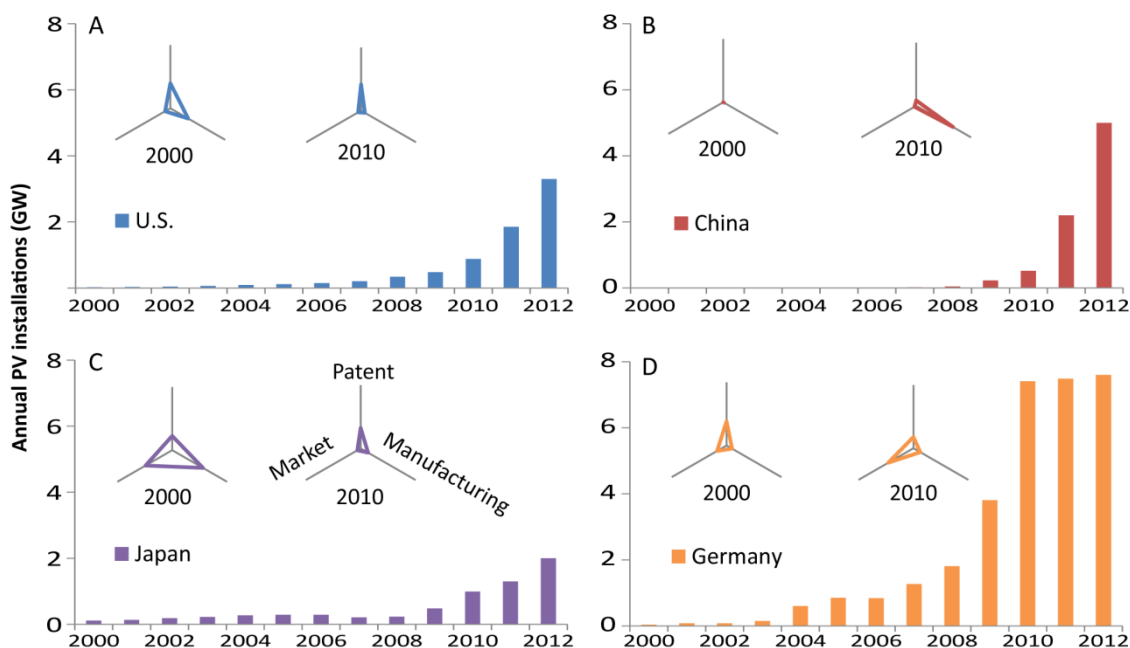
Figure 6.9. Evolution of innovation, manufacturing, and market in four key nations in the global PV industry. The radar plot inserts show the relative shares of market size, manufacturing, and annual PCT patent applications in PV among top four key nations (**Table A2.4** in the Appendix). The PV industry has a globalized value chain with China (B) being the top manufacturer and Germany (D) being the top market. The U.S. (A) and Japan (C) are the top two innovators in PV technology, despite their diminishing share in manufacturing and market size. These dynamics suggest that Germany's "demand-pull" approach had serious leakage problem in a globalized PV industry, and failed to promote a corresponding growth in innovation and manufacturing. Sources: EPI, EPIA, and WIPO.

Public R&D spending ("technology-push") and deployment incentives ("demand-pull") are two main types of government subsidies to solar PV (**Fig. 6.3**). In a relatively mature industry, both forms of subsidies can contribute to the technological development [210,211]. One way that deployment incentives support technological development is through subsidizing the sales of PV modules, where manufacturers use a fraction of the sales revenue for corporate R&D in PV. However, in a globalized market for PV modules, net importing countries could face serious leakage of deployment fund in supporting domestic innovation. For example, generous deployment incentives have made Germany the world's top PV installer, but Germany's innovation output still lags behind the U.S. and Japan (**Fig. 6.9**). Focusing on the role of

government subsidy on technological development, the allocation of government fund between R&D and deployment should be optimized for better efficiency in promoting technological innovation [222].

6.2.4. International coordination in resolving oversupply and restoring the incentives for innovation

The overcapacity situation (**Fig. 6.10A**) across the global PV industry makes capital-intensive investment in expanding production capacity unattractive to investors. Lacking the opportunities to scale up production, early-stage PV companies with innovative technologies, many of which are based on thin film PV, are forced to compete with GW-scale manufacturers at unsustainably low module prices. Based on the economies of scale found in the learning curve for First Solar's thin film technology (**Table A2.3**), the module cost from a 1-GW production scale could be 60%-67% lower than that from a 10-MW production scale. As a result, we see waves of smaller PV manufacturers bankrupt or acquired, some of which are more innovative than most of the top manufacturers (**Fig. 6.10 B&C**).
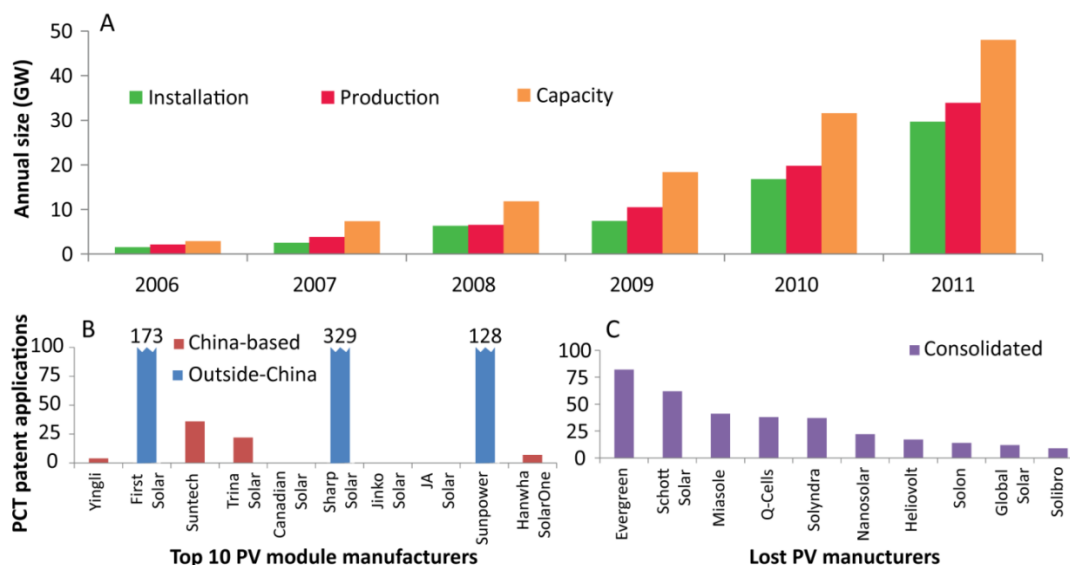
Figure 6.10. Innovative technologies struggling under the weight of oversupply. Excess capacity has been rapidly built up in the global PV industry since 2006 (A), which leads to production exceeding installation demand despite underutilization of production capacity. The top 10 PV module manufacturers (B) capture slightly below 50% of the global demand in 2012, only 3 of which are based outside of China. Among the consolidated PV manufacturers during 2011-2013, the average PCT applications of the top 10 innovative but consolidated companies (C) is about 3 times that of the 7 Chinese PV companies. Sources: EPIA, IEA PVPS, and WIPO.

In addition to the poor financial performance of the PV industry, uncertainties associated with government incentives for deployment and long-term commitment in reducing GHG

emissions also made venture capital (VC) more risk-averse towards investing in innovative solar startups (**Fig. 6.11**).
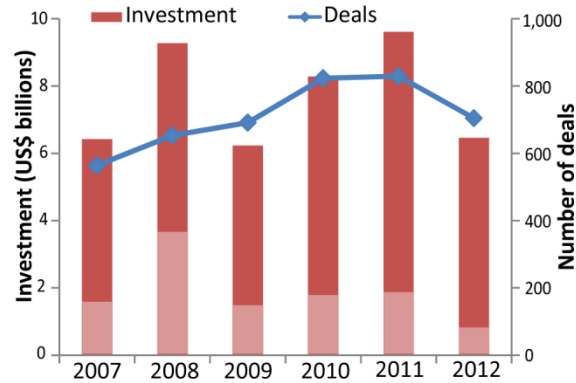
Figure 6.11. Global VC investment in the cleantech sector. The VC funding for solar technologies (in lighter red) is heavily slashed from about $3.6 billion in 2008 to $0.8 billion in 2012. Source: MIT Tech Review.

These disparities signal serious dysfunctions of the current energy policies towards solar PV, which makes the "demand-pull" approach less effective in incentivizing innovation. Key to restoring the incentives for innovation, the oversupply problem needs to be resolved promptly and module prices can temporarily recover to a more sustainable level. An international coordination in PV deployment policies is necessary for timely response, and a binding long-term installation target for PV can help the industry adjust more efficiently. The recent market growth in the U.S., China, and Japan shows encouraging development in increasing demand (**Fig. 6.9**). Being a hotspot in overcapacity (**Fig. 6.12**), China's State Council pledged in late 2012 to encourage consolidation among the Chinese PV manufacturers and banned local government support for failing ones.
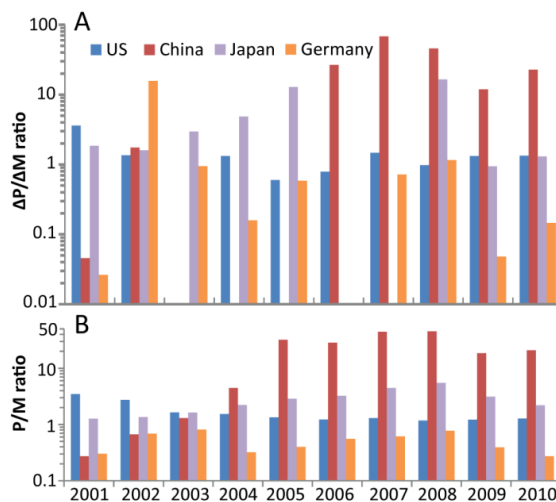
Figure 6.12. The dynamics between module manufacturing (P) and market size (M) in the PV industry. The ratio of production expansion to market expansion (A) is indicative of how well the domestic

manufacturing scales with the market size. Positive ratio shows increases in both production and installation, while negative ratio (not shown in A) is due to temporary reduction in either production or installation. Without considering the effect of inventory changes, the ratio of production to market size (B) of larger than 1.0 suggests the country being a net exporter, and vice versa. Sources: EPI and EPIA.

The need to restore innovation adds a fresh perspective to the discussion of trade issues in the PV industry. The trade tariff imposed by the U.S. [*223*] and the E.U. [*224*] would mitigate the oversupply problem in their home market and help their domestic PV manufacturing sector to recover faster, while accelerating the supply-demand adjustment in the Chinese PV industry. From a global perspective, Chinese PV manufacturers tend to have lower R&D intensity (**Fig. 6.5B**) and produce fewer patents (**Fig. 6.7**). With China's dominating market share in PV manufacturing, public fund through "demand-pull" policies has not been effectively channeled to the most innovative players. China could minimize the damage from an accelerated consolidation by supporting more innovative Chinese manufacturers. Largely as a casualty of the ongoing oversupply situation, the now-bankrupt Suntech was the most innovative Chinese PV manufacturer according to our metrics (R&D spending and patent applications) and established long-term R&D collaborations with leading PV research institutions such as the University of New South Wales.

6.3. Policy Framework for an Innovation-Driven Photovoltaic Industry Moving Forward

In his second inauguration speech President Obama urged the U.S. to lead and to profit from the transition to sustainable energy sources. Such opportunities for technologically advanced nations such as the U.S. may emerge as the PV industry enters an innovation-driven phase. Here we show a conceptual model (**Fig. 6.13**) exploring the dynamics among innovation, manufacturing, and market, and use the U.S. as a case study to explain an innovation-focused policy framework for building a sustainable PV industry on the national level.
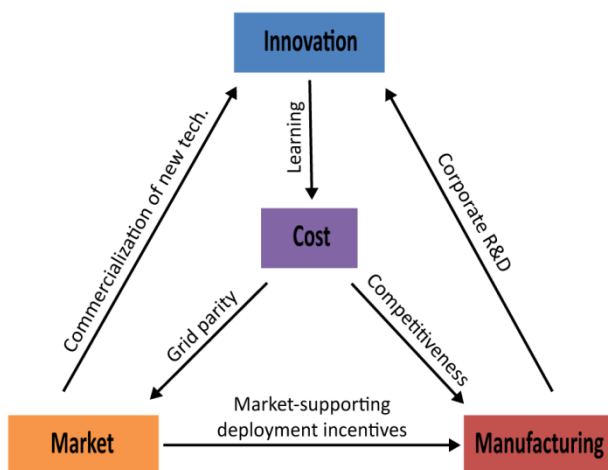
Figure 6.13. The conceptual model for building an innovation-focused and sustainable PV industry. Utilizing the reinforcing dynamics among innovation, manufacturing, and market, a set of long-term,

innovation-focused, and market-supporting policies can lead to a nation's technology leadership and help reduce the cost of PV technology for global deployment.

A set of clear-targeted and long-term deployment policies is essential in the reinforcing dynamics among innovation, manufacturing, and market. Firstly, scaling up the market can be an effective approach in fostering manufacturing base. Even without trade tariff manufacturing expansion has been observed to scale with market expansion (**Fig. 6.12**). Secondly, as part of the market-driven innovation mechanism, a long-term and expanding market also incentivizes commercialization of important laboratory results through channels such as VC funding.

Manufacturing activities are one important source of innovation through learning-by-doing. Moreover, the corporate R&D investment by PV manufacturers (**Fig. 6.5**) enables innovation through learning-by-searching. These R&D activities may prefer to co-locate with manufacturing base for better efficiency and rapid implementation of innovations to manufacturing lines, as highlighted by Applied Materials' largest commercial solar R&D center in China. However, another determining factor in the co-location between manufacturing and R&D activities is the nation's current innovation capacity. Despite its relatively small size in market and manufacturing, the U.S., with world-leading research institutions and talents, still leads in PV innovation, as measured by the number of PCT patent applications (**Fig. 6.7**). As the manufacturers' competitiveness increasingly relies on cost reduction through innovation, it is also possible for a nation to use innovation to anchor manufacturing activities, and thus form a reinforcing dynamics between innovation leadership and manufacturing leadership.

The optimum structure of the PV manufacturing sector will largely depend on trade policies. Without trade barriers, surviving international competition would require economies of scale and thus a critical size of the manufacturing cluster, where a handful of giant PV manufacturers may comprise most of the market share. On the other hand, the ongoing trade tariff will ease the international competition, and policymakers could promote a national PV manufacturing sector with lower market concentration. As previously described, giant incumbent manufacturers present large cost disadvantages and risks for start-up manufacturers, whose innovative technologies are yet to be scaled up. In a segmented global PV market, a national PV industry with low market concentration could be an additional boost to innovation during the next 7 to 10 years of an innovation-driven phase.

Elevated level of public R&D funding and focus on technological development in PV are the other central piece of this conceptual model. "Demand-pull" policies will likely face leakage problems on the national level in a globalized PV value chain (**Fig. 6.9**). Therefore, directly injecting resources to innovation by public R&D funding should play a stronger role. The IEA study in 2010 [225] identified the need to more than doubling the public R&D funding, benchmarking R&D budget as 10% to 20% of deployment cost. **Fig. 6.3** highlights the increasing R&D gap in the U.S. and Germany in the recent market scale-up. When the private sector is experiencing a difficult financial situation, it is a proper timing for increased public R&D funding to fill the gap in fueling innovation.

Innovation itself can be made more cost-effective with innovative R&D models [*226*], such as establishing a national program aimed at promoting R&D collaboration and technology transfer among PV manufacturers. For example, the U.S. funded a shared R&D center in 2011 through the PV Manufacturing Consortium, which borrowed the pre-competitive R&D model from the semiconductor industry.

An open data model could also be adopted by the government to attract more policy and market research. Various data collection efforts (from organizations like IEA to companies like BNEF) already exist; however, variations in data and methodologies are common. It is therefore useful to compile and continue to update an official dataset for the key metrics in the PV industry with well-documented methodologies. Making this dataset publicly available will greatly reduce the cost and time for conducting policy and market research. A richer set of analyses and opinions will be valuable for decision-making in both the government and industry, and accelerating policy and business innovation that address the soft cost of deploying PV technologies [*227*].

References

1   BP Energy Outlook 2035. (BP, http://bit.ly/BP-energy-outlook-2014, 2014).
2   World Energy Outlook 2013. (International Energy Agency, http://www.worldenergyoutlook.org/publications/weo-2013/, 2013).
3   International Energy Outlook 2014. (U.S. Energy Information Administration, http://www.eia.gov/forecasts/ieo/, 2014).
4   Wong, E. *As pollution worsens in China, solutions succumb to inflighting*, <http://bit.ly/NTY-Beijing-air-pollution> (2013).
5   Organization, W. H. *Seven million premature deaths annually linked to air pollution*, <http://www.who.int/mediacentre/news/releases/2014/air-pollution/en/> (2014).
6   World Energy Investment Outlook 2014. (International Energy Agency, http://www.worldenergyoutlook.org/investment/, 2014).
7   Vintage. *New York Killer Smog*, <http://www.vintag.es/2012/03/new-york-killer-smog-1953.html> (2012).
8   Annual Energy Outlook 2014. (U.S. Energy Information Administration, http://www.eia.gov/forecasts/aeo/, 2014).
9   BP Statistical Review of World Energy. (BP, http://bit.ly/BP-Energy-Data-2014, 2014).
10   Rowe, T. Global Market Outlook for Photovoltaics 2014-2018. (European Photovoltaic Industry Association, http://bit.ly/PV-market-EPIA-2014, 2014).
11   Chen, G. *Nanoscale Energy Transport and Conversion: A Parallel Treament of Electrons, Molecules, Phonons, and Photons*. (Oxford University Press, 2005).
12   Bransden, B. H. & Joachain, C. J. *Quantum Mechanics*. 2nd edn, (Prentice Hall, 2000).
13   Kasap, S. O. *Principles of Electronic Materials and Devices*. 2nd edn, (McGraw-Hill, 2000).
14   Swanson, R. M. Point-contact solar cells: Modeling and experiment. *Sol. Cells* **17**, 85-118, doi:10.1016/0379-6787(86)90061-X (1986).
15   Chapin, D. M., Fuller, C. S. & Pearson, G. L. A new silicon p-n junction photocell for converting solar radiation into electrical power. *J. Appl. Phys.* **25**, 676-677, doi:10.1063/1.1721711 (1954).
16   Zhao, J., Wang, A., Altermatt, P. & Green, M. A. Twenty-four percent efficient silicon solar cells with double layer antireflection coatings and reduced resistance loss. *Appl. Phys. Lett.* **66**, 3636-3638, doi:10.1063/1.114124 (1995).
17   NREL. *Research cell efficiency records*, <http://www.nrel.gov/ncpv/images/efficiency_chart.jpg> (2014).
18   Shockley, W. & Queisser, H. J. Detailed Balance Limit of Efficiency of p‐n Junction Solar Cells. *J. Appl. Phys.* **32**, 510-519, doi:10.1063/1.1736034 (1961).
19   Raut, H. K., Ganesh, V. A., Nair, A. S. & Ramakrishna, S. Anti-reflective coatings: A critical, in-depth review. *Energy Environ. Sci.* **4**, 3779-3804, doi:10.1039/c1ee01297e (2011).
20   Zhao, J. & Green, M. A. Optimized antireflection coatings for high-efficiency silicon solar cells. *IEEE Trans. Electr. Dev.* **38**, 1925-1934, doi:10.1109/16.119035 (1991).
21   Chhajed, S., Schubert, M. F., Kim, J. K. & Schubert, E. F. Nanostructured multilayer graded-index antireflection coating for Si solar cells with broadband and omnidirectional characteristics. *Appl. Phys. Lett.* **93**, -, doi:10.1063/1.3050463 (2008).
22   Diedenhofen, S. L. *et al.* Broad-band and omnidirectional antireflection coatings based on semiconductor nanorods. *Adv. Mater.* **21**, 973-978, doi:10.1002/adma.200802767 (2009).
23   Fan, Z. *et al.* Ordered arrays of dual-diameter nanopillars for maximized optical absorption. *Nano Lett.* **10**, 3823-3827, doi:10.1021/nl1010788 (2010).

24   Xi, J. Q. *et al.* Optical thin-film materials with low refractive index for broadband elimination of Fresnel reflection. *Nat. Photon.* **1**, 176-179, doi:10.1038/nphoton.2007.26 (2007).

25   Zhu, J. *et al.* Optical absorption enhancement in amorphous silicon nanowire and nanocone Arrays. *Nano Lett.* **9**, 279-282, doi:10.1021/nl802886y (2008).

26   Wang, K. X., Yu, Z., Liu, V., Cui, Y. & Fan, S. Absorption enhancement in ultrathin crystalline silicon solar cells with antireflection and light-trapping nanocone gratings. *Nano Lett.* **12**, 1616-1619, doi:10.1021/nl204550q (2012).

27   Huang, Y.-F. *et al.* Improved broadband and quasi-omnidirectional anti-reflection properties with biomimetic silicon nanostructures. *Nat. Nanotech.* **2**, 770-774 (2007).

28   Zhu, J., Hsu, C.-M., Yu, Z., Fan, S. & Cui, Y. Nanodome solar cells with efficient light management and self-cleaning. *Nano Lett.* **10**, 1979-1984, doi:10.1021/nl9034237 (2009).

29   Stalmans, L. *et al.* Porous silicon in crystalline silicon solar cells: A review and the effect on the internal quantum efficiency. *Prog. Photovolt: Res. Appl.* **6**, 233-246, doi:10.1002/(sici)1099-159x(199807/08)6:4<233::aid-pip207>3.0.co;2-d (1998).

30   Yuan, H.-C. *et al.* Efficient black silicon solar cell with a density-graded nanoporous surface: Optical properties, performance limitations, and design rules. *Appl. Phys. Lett.* **95**, 123501, doi:10.1063/1.3231438 (2009).

31   Koynov, S., Brandt, M. S. & Stutzmann, M. Black nonreflecting silicon surfaces for solar cells. *Appl. Phys. Lett.* **88**, 203107, doi:10.1063/1.2204573 (2006).

32   Yu, Z., Raman, A. & Fan, S. Fundamental limit of nanophotonic light trapping in solar cells. *Proc. Natl Aca. Sci. USA* **107**, 17491-17496, doi:10.1073/pnas.1008296107 (2010).

33   Hu, L. & Chen, G. Analysis of optical absorption in silicon nanowire arrays for photovoltaic applications. *Nano Lett.* **7**, 3249-3252, doi:10.1021/nl071018b (2007).

34   Garnett, E. & Yang, P. Light trapping in silicon nanowire solar cells. *Nano Lett.* **10**, 1082-1087, doi:10.1021/nl100161z (2010).

35   Wallentin, J. *et al.* InP nanowire array solar cells achieving 13.8% efficiency by exceeding the ray optics limit. *Science* **339**, 1057-1060, doi:10.1126/science.1230969 (2013).

36   Kelzenberg, M. D. *et al.* Enhanced absorption and carrier collection in Si wire arrays for photovoltaic applications. *Nat. Mater.* **9**, 239-244, doi:10.1038/nmat2635 (2010).

37   Atwater, H. A. & Polman, A. Plasmonics for improved photovoltaic devices. *Nat. Mater.* **9**, 205-213, doi:10.1038/nmat2629 (2010).

38   Green, M. A. & Pillai, S. Harnessing plasmonics for solar cells. *Nat Photon* **6**, 130-132 (2012).

39   Bermel, P., Luo, C., Zeng, L., Kimerling, L. C. & Joannopoulos, J. D. Improving thin-film crystalline silicon solar cell efficiencies with photonic crystals. *Opt. Express* **15**, 16986-17000, doi:10.1364/OE.15.016986 (2007).

40   Mallick, S. B., Agrawal, M. & Peumans, P. Optimal light trapping in ultra-thin photonic crystal crystalline silicon solar cells. *Opt. Express* **18**, 5691-5706, doi:10.1364/oe.18.005691 (2010).

41   Zeng, L. *et al.* Efficiency enhancement in Si solar cells by textured photonic crystal back reflector. *Appl. Phys. Lett.* **89**, -, doi:10.1063/1.2349845 (2006).

42   Campbell, P. & Green, M. A. Light trapping properties of pyramidally textured surfaces. *J. Appl. Phys.* **62**, 243-249, doi:10.1063/1.339189 (1987).

43   Green, M. A. Lambertian light trapping in textured solar cells and light-emitting diodes: analytical solutions. *Prog. Photovolt: Res. Appl.* **10**, 235-241, doi:10.1002/pip.404 (2002).

44   Mavrokefalos, A., Han, S. E., Yerci, S., Branham, M. S. & Chen, G. Efficient light trapping in inverted nanopyramid thin crystalline silicon membranes for solar cell applications. *Nano Lett.* **12**, 2792-2796, doi:10.1021/nl2045777 (2012).

45   Pijpers, J. J. H. *et al.* Assessment of carrier-multiplication efficiency in bulk PbSe and PbS. *Nat. Phys.* **5**, 811-814, doi:10.1038/nphys1393 (2009).

46   Karki, K. J. *et al.* Multiple exciton generation in nano-crystals revisited: Consistent calculation of the yield based on pump-probe spectroscopy. *Sci. Rep.* **3**, doi:10.1038/srep02287 (2013).
47   Sambur, J. B., Novet, T. & Parkinson, B. A. Multiple exciton collection in a sensitized photovoltaic system. *Science* **330**, 63-66, doi:10.1126/science.1191462 (2010).
48   Schaller, R. D. & Klimov, V. I. High efficiency carrier multiplication in PbSe nanocrystals: Implications for solar energy conversion. *Phys. Rev. Lett.* **92**, 186601, doi:10.1103/PhysRevLett.92.186601 (2004).
49   Semonin, O. E. *et al.* Peak external photocurrent quantum efficiency exceeding 100% via MEG in a quantum dot solar cell. *Science* **334**, 1530-1533, doi:10.1126/science.1209845 (2011).
50   Gabor, N. M., Zhong, Z., Bosnick, K., Park, J. & McEuen, P. L. Extremely efficient multiple electron-hole pair generation in carbon nanotube photodiodes. *Science* **325**, 1367-1371, doi:10.1126/science.1176112 (2009).
51   Ross, R. T. & Nozik, A. J. Efficiency of hot-carrier solar energy converters. *J. Appl. Phys.* **53**, 3813-3818, doi:10.1063/1.331124 (1982).
52   Würfel, P. Solar energy conversion with hot electrons from impact ionisation. *Sol. Energy Mater. Sol. Cells* **46**, 43-52, doi:10.1016/S0927-0248(96)00092-X (1997).
53   Tisdale, W. A. *et al.* Hot-electron transfer from semiconductor nanocrystals. *Science* **328**, 1543-1547, doi:10.1126/science.1185509 (2010).
54   Conibeer, G. J. *et al.* Selective energy contacts for hot carrier solar cells. *Thin Solid Films* **516**, 6968-6973, doi:10.1016/j.tsf.2007.12.031 (2008).
55   Dimmock, J. A. R., Day, S., Kauer, M., Smith, K. & Heffernan, J. Demonstration of a hot-carrier photovoltaic cell. *Prog. Photovolt: Res. Appl.* **22**, 151-160, doi:10.1002/pip.2444 (2014).
56   Luque, A. & Martí, A. Increasing the efficiency of ideal solar cells by photon induced transitions at intermediate levels. *Phys. Rev. Lett.* **78**, 5014-5017 (1997).
57   Luque, A., Marti, A. & Stanley, C. Understanding intermediate-band solar cells. *Nat. Photon.* **6**, 146-152, doi:10.1038/nphoton.2012.1 (2012).
58   Luque, A. & Martí, A. The intermediate band solar cell: Progress toward the realization of an attractive concept. *Adv. Mater.* **22**, 160-174, doi:10.1002/adma.200902388 (2010).
59   Barnham, K. W. J. & Duggan, G. A new approach to high-efficiency multi-band-gap solar cells. *J. Appl. Phys.* **67**, 3490-3493, doi:10.1063/1.345339 (1990).
60   Araújo, G. L. & Martí, A. Absolute limiting efficiencies for photovoltaic energy conversion. *Sol. Energy Mater. Sol. Cells* **33**, 213-240, doi:10.1016/0927-0248(94)90209-7 (1994).
61   Coutts, T. J. *et al.* Critical issues in the design of polycrystalline, thin-film tandem solar cells. *Prog. Photovolt: Res. Appl.* **11**, 359-375, doi:10.1002/pip.491 (2003).
62   Takamoto, T., Ikeda, E., Kurita, H. & Ohmori, M. Over 30% efficient InGaP/GaAs tandem solar cells. *Appl. Phys. Lett.* **70**, 381-383, doi:10.1063/1.118419 (1997).
63   Dou, L. *et al.* Tandem polymer solar cells featuring a spectrally matched low-bandgap polymer. *Nat. Photon.* **6**, 180-185, doi:http://www.nature.com/nphoton/journal/v6/n3/abs/nphoton.2011.356.html#supplementary-information (2012).
64   King, R. R. *et al.* 40% efficient metamorphic GaInP ∕ GaInAs ∕ Ge multijunction solar cells. *Appl. Phys. Lett.* **90**, -, doi:10.1063/1.2734507 (2007).
65   Geisz, J. F. *et al.* 40.8% efficient inverted triple-junction solar cell with two independently metamorphic junctions. *Appl. Phys. Lett.* **93**, -, doi:10.1063/1.2988497 (2008).
66   Guter, W. *et al.* Current-matched triple-junction solar cell reaching 41.1% conversion efficiency under concentrated sunlight. *Appl. Phys. Lett.* **94**, -, doi:10.1063/1.3148341 (2009).
67   Imenes, A. G. & Mills, D. R. Spectral beam splitting technology for increased conversion efficiency in solar concentrating systems: a review. *Sol. Energy Mater. Sol. Cells* **84**, 19-69, doi:10.1016/j.solmat.2004.01.038 (2004).

68   Polman, A. & Atwater, H. A. Photonic design principles for ultrahigh-efficiency photovoltaics. *Nat Mater* **11**, 174-177 (2012).

69   Goetzberger, A., Goldschmidt, J. C., Peters, M. & Löper, P. Light trapping, a new approach to spectrum splitting. *Sol. Energy Mater. Sol. Cells* **92**, 1570-1578, doi:10.1016/j.solmat.2008.07.007 (2008).

70   Green, M. A. & Ho-Baillie, A. Forty three per cent composite split-spectrum concentrator solar cell efficiency. *Prog. Photovolt: Res. Appl.* **18**, 42-47, doi:10.1002/pip.924 (2010).

71   McCambridge, J. D. *et al.* Compact spectrum splitting photovoltaic module with high efficiency. *Prog. Photovolt: Res. Appl.* **19**, 352-360, doi:10.1002/pip.1030 (2011).

72   Mitchell, B. *et al.* Four-junction spectral beam-splitting photovoltaic receiver with high optical efficiency. *Prog. Photovolt: Res. Appl.* **19**, 61-72, doi:10.1002/pip.988 (2011).

73   ARC Photovoltaics Center of Excellence Annual Report. (University of New South Wales, http://bit.ly/PV-make-UNSW2009, 2009).

74   Mono- and Multicrystalline Solar Cells. (Q-Cells, http://bit.ly/PV-make-Si-wafer-process).

75   Bullis, K. *China's solar industry: Behind the scenes at Suntech Power, the world's largest solar manufacturer*, <http://bit.ly/PV-make-suntech> (2011).

76   Nositschka, W. A., Voigt, O., Kenanoglu, A., Borchert, D. & Kurz, H. Dry phosphorus silicate glass etching for multicrystalline silicon solar cells. *Prog. Photovolt: Res. Appl.* **11**, 445-451, doi:10.1002/pip.505 (2003).

77   Scree Printing for Crystalline Silicon Solar Cells. (Applied Materials, http://bit.ly/PV-make-screen-print-AM, 2011).

78   Britt, J. & Ferekides, C. Thin‐film CdS/CdTe solar cell with 15.8% efficiency. *Appl. Phys. Lett.* **62**, 2851-2852, doi:10.1063/1.109629 (1993).

79   Wu, X. High-efficiency polycrystalline CdTe thin-film solar cells. *Sol. Energy* **77**, 803-814, doi:10.1016/j.solener.2004.06.006 (2004).

80   Gessert, T. A. *et al.* Research strategies toward improving thin-film CdTe photovoltaic devices beyond 20% conversion efficiency. *Sol. Energy Mater. Sol. Cells* **119**, 149-155, doi:10.1016/j.solmat.2013.05.055 (2013).

81   Cunningham, D., Rubcich, M. & Skinner, D. Cadmium telluride PV module manufacturing at BP Solar. *Prog. Photovolt: Res. Appl.* **10**, 159-168, doi:10.1002/pip.417 (2002).

82   Solar, F. *First Solar builds the highest efficiency thin film PV cell on record*, <http://investor.firstsolar.com/releasedetail.cfm?ReleaseID=864426> (2014).

83   Green, M. A., Emery, K., Hishikawa, Y., Warta, W. & Dunlop, E. D. Solar cell efficiency tables (version 44). *Prog. Photovolt: Res. Appl.* **22**, 701-710, doi:10.1002/pip.2525 (2014).

84   Solar, F. *First Solar Series 3 module manufacturing process*, <https://www.youtube.com/watch?v=87_a7LJhRgY> (2014).

85   Başol, B. M. & McCandless, B. Brief review of cadmium telluride-based photovoltaic technologies. *J. Photon. Energy* **4**, 040996-040996, doi:10.1117/1.jpe.4.040996 (2014).

86   Dunsky, C. M. & Colville, F. Scribing Thin-film Solar Panels. (Coherent, http://bit.ly/PV-make-laser-scribe-Coherent, 2008).

87   Mileva, A., Nelson, J. H., Johnston, J. & Kammen, D. M. SunShot solar power reduces costs and uncertainty in future low-carbon electricity systems. *Environ. Sci. Technol.* **47**, 9053-9060, doi:10.1021/es401898f (2013).

88   Margolis, R. SunShot Vision Study. (U.S. Department of Energy, http://bit.ly/PV-Sunshot-vision-study-2012, 2012).

89   Commission, E. A roadmap for moving to a competitive low carbon economy in 2050. (European Commission, http://ec.europa.eu/clima/policies/roadmap/index_en.htm, 2011).

90   Williams, J. H. *et al.* The technology path to deep greenhouse gas emissions cuts by 2050: The pivotal role of electricity. *Science* **335**, 53-59, doi:10.1126/science.1208365 (2012).

91   Hoffert, M. I. *et al.* Advanced technology paths to global climate stability: Energy for a greenhouse planet. *Science* **298**, 981-987, doi:10.1126/science.1072357 (2002).

92   Hoffert, M. I. Farewell to Fossil Fuels? *Science* **329**, 1292-1294, doi:10.1126/science.1195449 (2010).

93   Davis, S. J., Caldeira, K. & Matthews, H. D. Future CO2 emissions and climate change from existing energy infrastructure. *Science* **329**, 1330-1333, doi:10.1126/science.1188566 (2010).

94   Wadia, C., Alivisatos, A. P. & Kammen, D. M. Materials availability expands the opportunity for large-scale photovoltaics deployment. *Environ. Sci. Technol.* **43**, 2072-2077, doi:10.1021/es8019534 (2009).

95   Zweibel, K. The impact of tellurium supply on cadmium telluride photovoltaics. *Science* **328**, 699-701, doi:10.1126/science.1189690 (2010).

96   Andersson, B. A. Materials availability for large-scale thin-film photovoltaics. *Prog. Photovolt: Res. Appl.* **8**, 61-76, doi:10.1002/(sici)1099-159x(200001/02)8:1<61::aid-pip301>3.0.co;2-6 (2000).

97   Feltrin, A. & Freundlich, A. Material considerations for terawatt level deployment of photovoltaics. *Renew. Energy* **33**, 180-185, doi:10.1016/j.renene.2007.05.024 (2008).

98   Fthenakis, V. Sustainability metrics for extending thin-film photovoltaics to terawatt levels. *MRS Bulletin* **37**, 425-430, doi:10.1557/mrs.2012.50 (2012).

99   Solar, F. *First Solar to acquire TetraSun to expand addressable market opportunity*, <http://bit.ly/PV-make-FS-acquire-TetraSun> (2013).

100   Solar, F. *First Solar TetraSun module: Unprecedented performanceinrestricted spaces and distributed generation*, <http://www.firstsolar.com/en/technologies-and-capabilities/pv-modules/first-solar-tetrasun-module> (2014).

101   Yablonovitch, E. Statistical ray optics. *J. Opt. Soc. Am.* **72**, 899-907, doi:10.1364/josa.72.000899 (1982).

102   Yablonovitch, E. & Cody, G. D. Intensity enhancement in textured optical sheets for solar cells. *IEEE Trans. Electron Devices* **29**, 300-305, doi:10.1109/t-ed.1982.20700 (1982).

103   Schiff, E. A. Thermodynamic limit to photonic-plasmonic light-trapping in thin films on metals. *J. Appl. Phys.* **110**, 104501, doi:10.1063/1.3658848 (2011).

104   Dross, F. *et al.* Crystalline thin-foil silicon solar cells: where crystalline quality meets thin-film processing. *Prog. Photovolt: Res. Appl.* **20**, 770-784, doi:10.1002/pip.1238 (2012).

105   Bergmann, R. B., Berge, C., Rinke, T. J., Schmidt, J. & Werner, J. H. Advances in monocrystalline Si thin film solar cells by layer transfer. *Sol. Energy Mater. Sol. Cells* **74**, 213-218, doi:10.1016/S0927-0248(02)00070-3 (2002).

106   Reuter, M., Brendle, W., Tobail, O. & Werner, J. H. 50 μm thin solar cells with 17.0% efficiency. *Sol. Energy Mater. Sol. Cells* **93**, 704-706, doi:10.1016/j.solmat.2008.09.035 (2009).

107   Petermann, J. H. *et al.* 19%-efficient and 43 μm-thick crystalline Si solar cell from layer transfer using porous silicon. *Prog. Photovolt: Res. Appl.* **20**, 1-5, doi:10.1002/pip.1129 (2012).

108   Martin, I. T., Teplin, C. W., Doyle, J. R., Branz, H. M. & Stradins, P. Physics and chemistry of hot-wire chemical vapor deposition from silane: Measuring and modeling the silicon epitaxy deposition rate. *J. Appl. Phys.* **107**, 054906, doi:10.1063/1.3298455 (2010).

109   Alberi, K. *et al.* Material quality requirements for efficient epitaxial film silicon solar cells. *Appl. Phys. Lett.* **96**, 073502-073503, doi:10.1063/1.3309751 (2010).

110   Branz, H. M. *et al.* Hot-wire chemical vapor deposition of epitaxial film crystal silicon for photovoltaics. *Thin Solid Films* **519**, 4545-4550, doi:10.1016/j.tsf.2011.01.335 (2011).

111   Im, J. S. *et al.* Mixed-phase solidification of thin Si films on SiO2. *J. Cryst. Growth* **312**, 2775-2778, doi:10.1016/j.jcrysgro.2010.05.037 (2010).

112 Groves, J. R. *et al.* Biaxially-textured photovoltaic film crystal silicon on ion beam assisted deposition CaF2 seed layers on glass. *Energy Environ. Sci.* **5**, 6905-6908, doi:10.1039/c2ee21097e (2012).

113 Kim, D. R., Lee, C. H., Weisse, J. M., Cho, I. S. & Zheng, X. Shrinking and growing: Grain boundary density reduction for efficient polysilicon thin-film solar cells. *Nano Lett.* **12**, 6485-6491, doi:10.1021/nl3041492 (2012).

114 Wee, S. H. *et al.* Heteroepitaxial film silicon solar cell grown on Ni-W foils. *Energy Environ. Sci.* **5**, 6052-6056, doi:10.1039/C2EE03350J (2012).

115 Im, J. S., Sposili, R. S. & Crowder, M. A. Single-crystal Si films for thin-film transistor devices. *Appl. Phys. Lett.* **70**, 3434-3436, doi:10.1063/1.119194 (1997).

116 Ishihara, R. *et al.* Advanced excimer-laser crystallization process for single-crystalline thin film transistors. *Thin Solid Films* **427**, 77-85, doi:10.1016/s0040-6090(02)01250-6 (2003).

117 Vogel, E. Technology and metrology of new electronic materials and devices. *Nat. Nano.* **2**, 25-32, doi:10.1038/nnano.2006.142 (2007).

118 De Vos, K., Bartolozzi, I., Schacht, E., Bienstman, P. & Baets, R. Silicon-on-Insulator microring resonator forsensitive and label-free biosensing. *Opt. Express* **15**, 7610-7615, doi:10.1364/oe.15.007610 (2007).

119 Xia, F., Sekaric, L. & Vlasov, Y. Ultracompact optical buffers on a silicon chip. *Nat. Photon.* **1**, 65-71, doi:10.1038/nphoton.2006.42 (2007).

120 Miyao, M., Ohkura, M., Warabisa, T. & Tokuyama, T. Characterization and application of laser induced seeded-lateral epitaxtal Si layers on SiO2. *MRS Proc.* **13**, 499-510, doi:10.1557/proc-13-499 (1982).

121 Hu, S., Leu, P. W., Marshall, A. F. & McIntyre, P. C. Single-crystal germanium layers grown on silicon by nanowire seeding. *Nature Nanotechnology* **4**, 649-653, doi:10.1038/nnano.2009.233 (2009).

122 Im, J. S. & Kim, H. J. On the super lateral growth phenomenon observed in excimer laser-induced crystallization of thin Si films. *Appl. Phys. Lett.* **64**, 2303-2305, doi:10.1063/1.111651 (1994).

123 Chimmalgi, A., Hwang, D. J. & Grigoropoulos, C. P. Nanoscale rapid melting and crystallization of semiconductor thin films. *Nano Lett.* **5**, 1924-1930, doi:10.1021/nl051244q (2005).

124 Lee, M., Moon, S., Hatano, M., Suzuki, K. & Grigoropoulos, C. P. Relationship between fluence gradient and lateral grain growth in spatially controlled excimer laser crystallization of amorphous silicon films. *J. Appl. Phys.* **88**, 4994-4999, doi:10.1063/1.1314303 (2000).

125 Sposili, R. S. & Im, J. S. Sequential lateral solidification of thin silicon films on SiO2. *Applied Physics Letters* **69**, 2864-2866, doi:10.1063/1.117344 (1996).

126 Voutsas, A. T., Limanov, A. & Im, J. S. Effect of process parameters on the structural characteristics of laterally grown, laser-annealed polycrystalline silicon films. *J. Appl. Phys.* **94**, 7445-7452, doi:10.1063/1.1627462 (2003).

127 Lee, M., Moon, S. & Grigoropoulos, C. P. In situ visualization of interface dynamics during the double laser recrystallization of amorphous silicon thin films. *J. Cryst. Growth* **226**, 8-12, doi:10.1016/S0022-0248(01)01272-6 (2001).

128 Xu, L., Grigoropoulos, C. P. & King, T.-J. High-performance thin-silicon-film transistors fabricated by double laser crystallization. *J. Appl. Phys.* **99**, 034508-034506, doi:10.1063/1.2171807 (2006).

129 Lee, M., Moon, S., Hatano, M. & Grigoropoulos, C. P. Ultra-large lateral grain growth by double laser recrystallization of a-Si films. *Appl. Phys. A* **73**, 317-322, doi:10.1007/s003390100874 (2001).

130 Carey, V. *Statistical Thermodynamics and Microscale Thermophysics*. 93-95 (Cambridge Uni. Press, 1999).

131 Jackson, K. A. *Kinetic Processes: Crystal Growth, Diffusion, and Phase Transistions in Materials*. (Wiley-VCH, 2010).

132 Donovan, E. P., Spaepen, F., Turnbull, D., Poate, J. M. & Jacobson, D. C. Heat of crystallization and melting point of amorphous silicon. *Appl. Phys. Lett.* **42**, 698-700, doi:10.1063/1.94077 (1983).

133 Stiffler, S. R., Thompson, M. O. & Peercy, P. S. Supercooling and nucleation of silicon after laser melting. *Phys. Rev. Lett.* **60**, 2519-2522 (1988).

134 Shao, Y. & Spaepen, F. Undercooling of bulk liquid silicon in an oxide flux. *J. Appl. Phys.* **79**, 2981-2985, doi:10.1063/1.361222 (1996).

135 Liu, R. P., Volkmann, T. & Herlach, D. M. Undercooling and solidification of Si by electromagnetic levitation. *Acta Mater.* **49**, 439-444, doi:10.1016/S1359-6454(00)00330-X (2001).

136 Motooka, T. & Munetoh, S. Molecular-dynamics simulations of nucleation and crystallization in supercooled liquid silicon: Temperature-gradient effects. *Phys. Rev. B* **69**, 073307, doi:10.1103/PhysRevB.69.073307 (2004).

137 Landau, L. D. & Lifshitz, E. M. *Statistical Physics I*. 3 edn, 333-346 (Elsevier, 1980).

138 Mittiga, A., Fornarini, L. & Carluccio, R. Numerical modeling of laser induced phase transitions in silicon. *Appl. Surf. Sci.* **154**, 112-117, doi:10.1016/S0169-4332(99)00436-5 (2000).

139 Kelton, K. F., Greer, A. L. & Thompson, C. V. Transient nucleation in condensed systems. *J. Chem. Phys.* **79**, 6261-6276, doi:10.1063/1.445731 (1983).

140 Broughton, J. Q. & Li, X. P. Phase diagram of silicon by molecular dynamics. *Phys. Rev. B* **35**, 9120-9127, doi:10.1103/PhysRevB.35.9120 (1987).

141 Turnbull, D. Kinetics of Solidification of Supercooled Liquid Mercury Droplets. *J. Chem. Phys.* **20**, 411-424, doi:10.1063/1.1700435 (1952).

142 Wood, R. F. & Geist, G. A. Modeling of nonequilibrium melting and solidification in laser-irradiated materials. *Phys. Rev. B* **34**, 2606-2620, doi:10.1103/PhysRevB.34.2606 (1986).

143 Galvin, G. J. *et al.* Measurement of the Velocity of the Crystal-Liquid Interface in Pulsed Laser Annealing of Si. *Phys. Rev. Lett.* **48**, 33-36, doi:10.1103/PhysRevLett.48.33 (1982).

144 Thompson, M. O. *et al.* Melting temperature and explosive crystallization of amorphous silicon during pulsed laser irradiation. *Phys. Rev. Lett.* **52**, 2360-2363, doi:10.1103/PhysRevLett.52.2360 (1984).

145 Moon, S., Lee, M. & Grigoropoulos, C. P. Heat transfer and phase transformations in laser annealing of thin Si films. *J. Heat Transfer* **124**, 253-264, doi:10.1115/1.1447941 (2002).

146 Hatano, M., Moon, S., Lee, M., Suzuki, K. & Grigoropoulos, C. P. Excimer laser-induced temperature field in melting and resolidification of silicon thin films. *J. Appl. Phys.* **87**, 36-43, doi:10.1063/1.371823 (2000).

147 Stolk, P. A., Polman, A. & Sinke, W. C. Experimental test of kinetic theories for heterogeneous freezing in silicon. *Phys. Rev. B* **47**, 5-13, doi:10.1103/PhysRevB.47.5 (1993).

148 Salinga, M. *et al.* Measurement of crystal growth velocity in a melt-quenched phase-change material. *Nat. Commun.* **4**, doi:10.1038/ncomms3371 (2013).

149 Kluge, M. D. & Ray, J. R. Velocity versus temperature relation for solidification and melting of silicon: A molecular-dynamics study. *Phys. Rev. B* **39**, 1738-1746, doi:10.1103/PhysRevB.39.1738 (1989).

150 Ryu, S.-G., Gruber, I., Grigoropoulos, C. P., Poulikakos, D. & Moon, S.-J. Large area crystallization of amorphous Si with overlapping high repetition rate laser pulses. *Thin Solid Films* **520**, 6724-6729, doi:10.1016/j.tsf.2012.07.052 (2012).

151 Habenicht, A., Olapinski, M., Burmeister, F., Leiderer, P. & Boneberg, J. Jumping nanodroplets. *Science* **309**, 2043-2045, doi:10.1126/science.1116505 (2005).

152 Craster, R. V. & Matar, O. K. Dynamics and stability of thin liquid films. *Rev. Mod. Phys.* **81**, 1131-1198, doi:10.1103/RevModPhys.81.1131 (2009).

153 Singer, J. P. *et al.* Direct-write thermocapillary dewetting of polymer thin films by a laser-induced thermal gradient. *Adv. Mater.* **25**, 6100-6105, doi:10.1002/adma.201302777 (2013).

154 Yuan, Z. F., Mukai, K. & Huang, W. L. Surface tension and its temperature coefficient of molten silicon at different oxygen potentials. *Langmuir* **18**, 2054-2062, doi:10.1021/la0112920 (2002).

155 Zhou, Z., Mukherjee, S. & Rhim, W.-K. Measurement of thermophysical properties of molten silicon using an upgraded electrostatic levitator. *J. Cryst. Growth* **257**, 350-358, doi:10.1016/S0022-0248(03)01430-1 (2003).

156 Nerding, M. *et al.* Microstructure of laser-crystallized silicon thin films on glass substrate. *J. Appl. Phys.* **91**, 4125-4130, doi:doi:http://dx.doi.org/10.1063/1.1454189 (2002).

157 Weizman, M., Klimm, C., Nickel, N. H. & Rech, B. Origin of preferential grain orientation in excimer laser-induced crystallization of silicon thin films. *Appl. Phys. Lett.* **100**, 161906, doi:10.1063/1.4704559 (2012).

158 Wu, Y. *et al.* Controlled growth and structures of molecular-scale silicon nanowires. *Nano Lett.* **4**, 433-436, doi:10.1021/nl035162i (2004).

159 Xiang, B. *et al.* In situ TEM near-field optical probing of nanoscale silicon crystallization. *Nano Lett.* **12**, 2524-2529, doi:10.1021/nl3007352 (2012).

160 Zheng, C. & Kammen, D. M. An innovation-focused roadmap for a sustainable global photovoltaic industry. *Energy Policy* **67**, 159-169, doi:10.1016/j.enpol.2013.12.006 (2014).

161 Breyer, C. & Gerlach, A. Global overview on grid-parity. *Prog. Photovolt: Res. Appl.* **21**, 121-136, doi:10.1002/pip.1254 (2013).

162 Lorenz, P., Pinner, D. & Seitz, T. The Economics of Solar Power. (McKinsey, 2008).

163 Frankel, D., Ostrowski, K. & Pinner, D. The Disruptive Potential of Solar Power. (McKinsey, http://www.mckinsey.com/insights/energy_resources_materials/the_disruptive_potential_of_solar_power, 2014).

164 Bazilian, M. *et al.* Re-considering the economics of photovoltaic power. *Renew. Energy* **53**, 329-338, doi:10.1016/j.renene.2012.11.029 (2013).

165 Darling, S. B., You, F., Veselka, T. & Velosa, A. Assumptions and the levelized cost of energy for photovoltaics. *Energy Environ. Sci.* **4**, 3133-3139, doi:10.1039/C0EE00698J (2011).

166 Baker, E., Fowlie, M., Lemoine, D. & Reynolds, S. S. The Economics of Solar Electricity. (Energy Institute at Haas, http://ei.haas.berkeley.edu/pdf/working_papers/WP240.pdf, 2013).

167 Campbell, M. The Drivers of the Levelized Cost of Electricity for Utility-scale Photovoltaics. (SunPower, 2008).

168 Breyer, C. & Schmid, J. Global distribution of optimal tilt angles for fixed tilted PV systems. *Proc. WCPEC-5*, 4715-4721, doi:10.4229/25thEUPVSEC2010-4BV.1.93 (2010).

169 Boden, S. A. & Bagnall, D. M. Sunrise to sunset optimization of thin film antireflective coatings for encapsulated, planar silicon solar cells. *Prog. Photovolt: Res. Appl.* **17**, 241-252, doi:10.1002/pip.884 (2009).

170 Bunea, G., Xavier, G., Rose, D., Nelson, L. & Peurach, J. Performance and Reliability of Modules with Anti-Reflective Coated Glass. (SunPower, 2010).

171 Yu, E. T. & van de Lagemaat, J. Photon management for photovoltaics. *MRS Bulletin* **36**, 424-428, doi:10.1557/mrs.2011.109 (2011).

172 Nagel, H., Aberle, A. G. & Hezel, R. Optimised antireflection coatings for planar silicon solar cells using remote PECVD silicon nitride and porous silicon dioxide. *Prog. Photovolt: Res. Appl.* **7**, 245-260, doi:10.1002/(sici)1099-159x(199907/08)7:4<245::aid-pip255>3.0.co;2-3 (1999).

173 Min, W.-L., Jiang, B. & Jiang, P. Bioinspired self-cleaning antireflection coatings. *Adv. Materials* **20**, 3914-3918, doi:10.1002/adma.200800791 (2008).

174 Aanesen, K., Heck, S. & Pinner, D. Solar Power: Darkest before Dawn. (McKinsey, http://bit.ly/PV-installation-McKinsey, 2012).

175 Chang, T. P. Output energy of a photovoltaic module mounted on a single-axis tracking system. *Appl. Energy* **86**, 2071-2078, doi:10.1016/j.apenergy.2009.02.006 (2009).

176 Narvarte, L. & Lorenzo, E. Tracking and ground cover ratio. *Prog. Photovolt: Res. Appl.* **16**, 703-714, doi:10.1002/pip.847 (2008).

177 Lave, M. & Kleissl, J. Optimum fixed orientations and benefits of tracking for capturing solar radiation in the continental United States. *Renew. Energy* **36**, 1145-1152, doi:10.1016/j.renene.2010.07.032 (2011).

178 Calabrò, E. Determining optimum tilt angles of photovoltaic panels at typical north-tropical latitudes. *J. Renew. Sustain. Energy* **1**, 033101, doi:10.1063/1.3148272 (2009).

179 Ganesh, V. A., Raut, H. K., Nair, A. S. & Ramakrishna, S. A review on self-cleaning coatings. *J. Mater. Chem.* **21**, 16304-16322, doi:10.1039/C1JM12523K (2011).

180 Gueymard, C. A., Myers, D. & Emery, K. Proposed reference irradiance spectra for solar energy systems testing. *Sol. Energy* **73**, 443-467, doi:10.1016/S0038-092X(03)00005-7 (2002).

181 Green, M. A. & Keevers, M. J. Optical properties of intrinsic silicon at 300 K. *Prog. Photovolt: Res. Appl.* **3**, 189-192, doi:10.1002/pip.4670030303 (1995).

182 Siegel, R. & Howell, J. R. *Thermal Radiation Heat Transfer*. 4 edn, 779-784 (Taylor & Francis, 2002).

183 Ciddor, P. E. Refraction into an absorbing medium. *Am. J. Phys.* **44**, 786-787, doi:10.1119/1.10317 (1976).

184 Zhao, J., Wang, A., Green, M. A. & Ferrazza, F. 19.8% efficient "honeycomb" textured multicrystalline and 24.4% monocrystalline silicon solar cells. *Appl. Phys. Lett.* **73**, 1991-1993, doi:10.1063/1.122345 (1998).

185 Culligan, M. & Botkin, J. Impact of Tilt Angle on System Economics for Area Constrained Rooftops. (SunPower, 2007).

186 Darghouth, N. R., Barbose, G. & Wiser, R. The impact of rate design and net metering on the bill savings from distributed PV for residential customers in California. *Energy Policy* **39**, 5243-5253, doi:10.1016/j.enpol.2011.05.040 (2011).

187 Benson, G. S. PURPA at 35: At a crossroads? *Power* **157**, 30, doi:http://www.powermag.com/purpa-at-35-at-a-crossroads (2013).

188 DSIRE. *DSIRE solar policy guide*, <http://www.dsireusa.org/solar/solarpolicyguide/> (2014).

189 Sarzynski, A., Larrieu, J. & Shrimali, G. The impact of state financial incentives on market deployment of solar technology. *Energy Policy* **46**, 550-557, doi:10.1016/j.enpol.2012.04.032 (2012).

190 Li, H. & Yi, H. Multilevel governance and deployment of solar PV panels in U.S. cities. *Energy Policy* **69**, 19-27, doi:10.1016/j.enpol.2014.03.006 (2014).

191 pvXchange. *Price index: Crystalline modules*, <http://www.pvxchange.com/priceindex> (2014).

192 Sharif, D., Grace, A. & Capua, M. D. The Return - and Returns - of Tax Equity for US Renewable Projects. (Bloomberg New Energy Finance, http://about.bnef.com/white-papers/, 2011).

193 *1603 program: Payments for specified energy property in lieu of tax credits*, <http://www.treasury.gov/initiatives/recovery/Pages/1603.aspx> (2014).

194 Farrell, J. *Treasury Dept. fingers SolarCity in exploration of the dark underbelly of solar leasing*, <http://bit.ly/PV-ITC-high-price> (2012).

195 Friedman, B., James, T., Margolis, R. & Seel, J. Comparing Photovoltaic Costs and Deployment Drivers in the Japanese and U.S. Residential and Commercial Markets. (National Renewable Energy Laboratory, http://bit.ly/PV-policy-Japan-US-NREL-2014, 2014).

196 Solangi, K. H., Islam, M. R., Saidur, R., Rahim, N. A. & Fayaz, H. A review on global solar energy policy. *Renew. Sustain. Energy Rev.* **15**, 2149-2163, doi:10.1016/j.rser.2011.01.007 (2011).

197 Timilsina, G. R., Kurdgelashvili, L. & Narbel, P. A. Solar energy: Markets, economics and policies. *Renew. Sustain. Energy Rev.* **16**, 449-465, doi:10.1016/j.rser.2011.08.009 (2012).

198 Fulton, M. & Capalino, R. The German Feed-In Tariff: Recent Policy Changes. (Deutsch Bank Research, http://bit.ly/PV-FiT-DB-2012, 2012).

199 Davis, L. L. & Allen, K. Feed-in tariffs in turmoil. *West Virginia Law Rev.* **116**, 937 (2014).

200 Finance, B. N. E. *Solar's 'leanring curve'*, <http://go.bloomberg.com/multimedia/solar-silicon-price-drop-brings-renewable-power-closer/> (2012).

201 Acs, Z. J., Anselin, L. & Varga, A. Patents and innovation counts as measures of regional production of new knowledge. *Res. Policy* **31**, 1069-1085, doi:10.1016/S0048-7333(01)00184-6 (2002).

202 Margolis, R. M. & Kammen, D. M. Underinvestment: The energy technology and R&D policy challenge. *Science* **285**, 690-692, doi:10.1126/science.285.5428.690 (1999).

203 Lanjouw, J. O. & Schankerman, M. Patent quality and research productivity: Measuring innovation with multiple indicators. *Econ. J.* **114**, 441-465, doi:10.2307/3590103 (2004).

204 van Pottelsberghe de la Potterie, B. The quality factor in patent systems. *Ind. Corp. Change* **20**, 1755-1793, doi:10.1093/icc/dtr066 (2011).

205 Schwab, K. The Global Competitiveness Report. (World Economic Forum, http://bit.ly/WEF-competitiveness-2013, 2012).

206 Sagar, A. D. & van der Zwaan, B. Technological innovation in the energy sector: R&D, deployment, and learning-by-doing. *Energy Policy* **34**, 2601-2608, doi:10.1016/j.enpol.2005.04.012 (2006).

207 Qiu, Y. & Anadon, L. D. The price of wind power in China during its expansion: Technology adoption, learning-by-doing, economies of scale, and manufacturing localization. *Energy Econ.* **34**, 772-785, doi:10.1016/j.eneco.2011.06.008 (2012).

208 van der Zwaan, B. & Rabl, A. The learning potential of photovoltaics: Implications for energy policy. *Energy Policy* **32**, 1545-1554, doi:10.1016/S0301-4215(03)00126-5 (2004).

209 Ferioli, F., Schoots, K. & van der Zwaan, B. C. C. Use and limitations of learning curves for energy technology policy: A component-learning hypothesis. *Energy Policy* **37**, 2525-2535, doi:10.1016/j.enpol.2008.10.043 (2009).

210 Bettencourt, L. M. A., Trancik, J. E. & Kaur, J. Determinants of the pace of global innovation in energy technologies. *PLoS ONE* **8**, e67864, doi:10.1371/journal.pone.0067864 (2013).

211 Jamasb, T. Technical change theory and learning curves: Patterns of progress in electricity generation technologies. *Energy J.* **28**, 51-71, doi:10.2307/41323109 (2007).

212 Hafner, F. Patents and Clean Energy. (European Patent Office, http://bit.ly/PV-patent-clean-energy-EPO, 2010).

213 Nemet, G. F. Beyond the learning curve: factors influencing cost reductions in photovoltaics. *Energy Policy* **34**, 3218-3232, doi:10.1016/j.enpol.2005.06.020 (2006).

214 Lewis, N. S. Toward cost-effective solar energy use. *Science* **315**, 798-801, doi:10.1126/science.1137014 (2007).

215 Chu, S. & Majumdar, A. Opportunities and challenges for a sustainable energy future. *Nature* **488**, 294-303, doi:10.1038/nature11475 (2012).

216 Goodrich, A., James, T. & Woodhouse, M. Residential, commercial, and utility-scale photovoltaic systems in the United States: Current drivers and cost-reduction opportunities. (National Renewable Energy Laboratory, http://www.nrel.gov/docs/fy12osti/53347.pdf, 2012).

217 Powell, D. M. *et al.* Crystalline silicon photovoltaics: A cost analysis framework for determining technology pathways to reach baseload electricity costs. *Energy Environ. Sci.* **5**, 5874-5883, doi:10.1039/c2ee03489a (2012).

218 Goodrich, A. *et al.* A wafer-based monocrystalline silicon photovoltaics road map: Utilizing known technology improvement opportunities for further reductions in manufacturing costs. *Sol. Energy Mater. Sol. Cells* **114**, 110-135, doi:10.1016/j.solmat.2013.01.030 (2013).

219 Jaffe, A. B., Newell, R. G. & Stavins, R. N. A tale of two market failures: Technology and environmental policy. *Ecol. Econ.* **54**, 164-174, doi:10.1016/j.ecolecon.2004.12.027 (2005).

220 Mills, E. The greening of insurance. *Science* **338**, 1424-1425, doi:10.1126/science.1229351 (2012).

221 Hansen, J., Sato, M. & Ruedy, R. Perception of climate change. *Proc. Natl. Aca. Sci. USA*, doi:10.1073/pnas.1205276109 (2012).

222 Frondel, M., Ritter, N. & Schmidt, C. M. Germany's solar cell promotion: Dark clouds on the horizon. *Energy Policy* **36**, 4198-4204, doi:10.1016/j.enpol.2008.07.026 (2008).

223 Deutch, J. & Steinfeld, E. A duel in the sun: The solar photovoltaics technology conflict between China and the United States. (Massachusetts Institute of Technology, http://mitei.mit.edu/publications/reports-studies/future-solar, 2013).

224 James, A. & Mehta, S. The EU-China deal: What we know and don't know. (GTM Research, 2013).

225 Kerr, T. Global Gaps in Clean Energy RD&D. (International Energy Agency, http://bit.ly/PV-RDD-IEA, 2010).

226 Coggeshall, C. & Margolis, R. M. Consortia Focused on Photovoltaic R&D, Manufacturing, and Testing: A Review of Existing Models and Structures. (National Renewable Energy Laboratory, doi: 10.2172/974459, 2010).

227 Seel, J., Barbose, G. & Wiser, R. Why are Residential PV Prices in Germany so much Lower than in the United States? , (Lawrence Berkeley National Laboratory, http://bit.ly/PV-installation-US-DE-2013, 2013).

A1. Laser Crystallization Experiment

A1.1. Chemical vapor deposition of thin a-Si films

The a-Si film is deposited using the standard low pressure chemical vapor deposition (LPCVD) process in cleanroom. 100 nm of a-Si film is deposited using the standard recipe (10vdasia) at 550 oC for 30 minutes in the tystar10 LPCVD furnace in the Marvell Nanolab.

Cross-section SEM image is used to calibrate the deposition rate, which turns out to be about 3.33 nm/min. The trick for high contrast cross-section SEM image for the a-Si film is to deposit the film on an oxide-coated control sample: after 60 seconds 5:1 BHF etching, about 250 nm of oxide will be etched away, creating step change in height at the interface between a-Si and oxide as shown in **Fig. A1.1**.
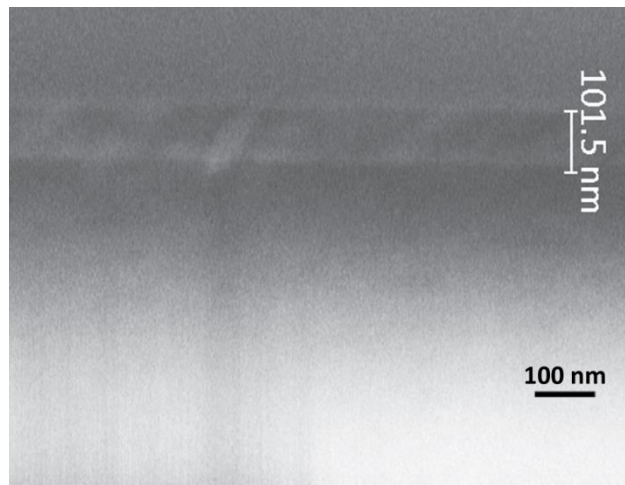
Figure A1.1. Cross-section SEM image of the deposited a-Si film on top of an oxide layer.

A1.2. Control and measurement of the laser power

The laser beam is of 532 nm in wavelength and 22 ns in full-width-half-maximum (FWHM) pulse duration, generated from frequency doubling by a second harmonic generator after a diode-pumped Nd:YVO$_4$ laser with a repetition rate of 10 kHz. The laser power is controlled by using a half-wave plate and a beam splitter as in **Fig. A1.2**. The half-wave plate rotates the polarization of the laser beam by 2θ and the beam splitter allows only the p-polarization to transmit, effectively controlling the laser power. The laser power P_c with respect to the angle θ on the half-wave plate is measured and modeled as in **Eq. A1.1** and **Fig. A1.3**.
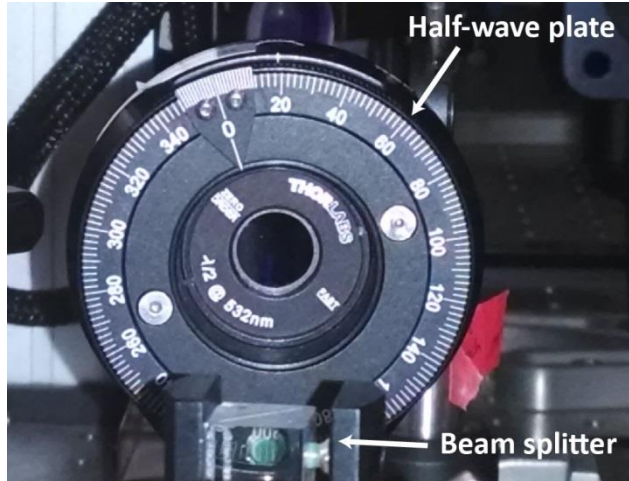
Figure A1.2. Control of laser power by a half-wave plate and a beam splitter.

$$P_c = \alpha_0 + \alpha_1 \sin(2\theta)$$
<div align="right">**Equation A1.1**</div>
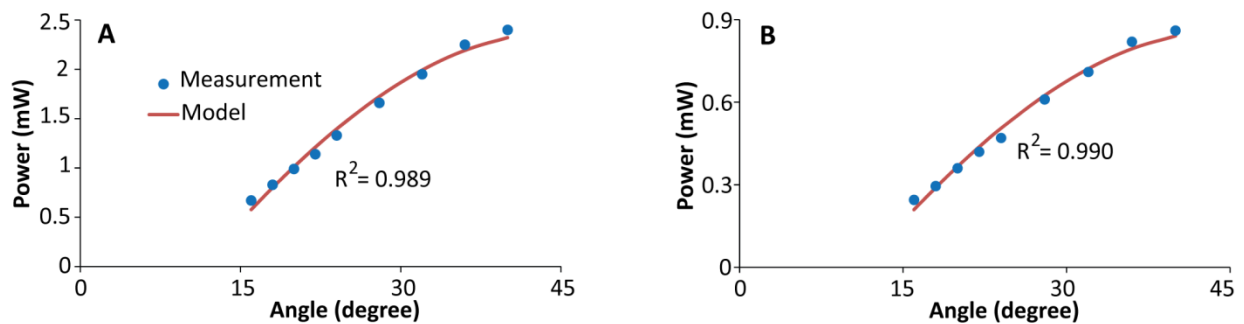
Figure A1.3. Measurement and calibration of laser power. The model is based on Eq. 4B-1, and the R-squared (R^2) values for the regression are 0.989 and 0.990 for 10x lens (A) and 20x lens (B), respectively.

A1.3. Characterization of the laser beam profile

The diameter of the focused laser beams on the a-Si film, after the objective lens (20X and 10X), are about 3.2 μm and 6 μm, respectively. The laser beam is characterized by the knife-edge method [1], where the razor edge blocks part of the laser beam and yields a distance-dependent power readings. For a circular Gaussian beam, the laser intensity can be expressed as a function of peak intensity in the center I_0, the distance from the center r, and the radius of the beam w, as in **Eq. A1.2**.

$$I(r) = I_0 \exp\left(-\frac{2r^2}{w^2}\right)$$
<div align="right">**Equation A1.2**</div>

The total power of the circular laser beam P_c can be expressed as in **Eq. A1-3**.

$$P_c = \int_{-\infty}^{\infty} I_0 \exp\left(-\frac{2r^2}{w^2}\right) dr = \pi w^2 \frac{I_0}{2}$$ **Equation A1.3**

The distance-dependent power readings P(x), as in **Eq. A1.4**, is used to fit the curves in **Fig. A1.4**.

$$P(x) = I_0 \int_{-\infty}^{\infty} \exp\left(-\frac{2y^2}{w^2}\right) dy \int_{-\infty}^{x} \exp\left(-\frac{2X^2}{w^2}\right) dX == \frac{P_c}{2}\left[1 - \mathrm{erf}\left(\frac{\sqrt{2}x}{w}\right)\right]$$ **Equation A1.4**
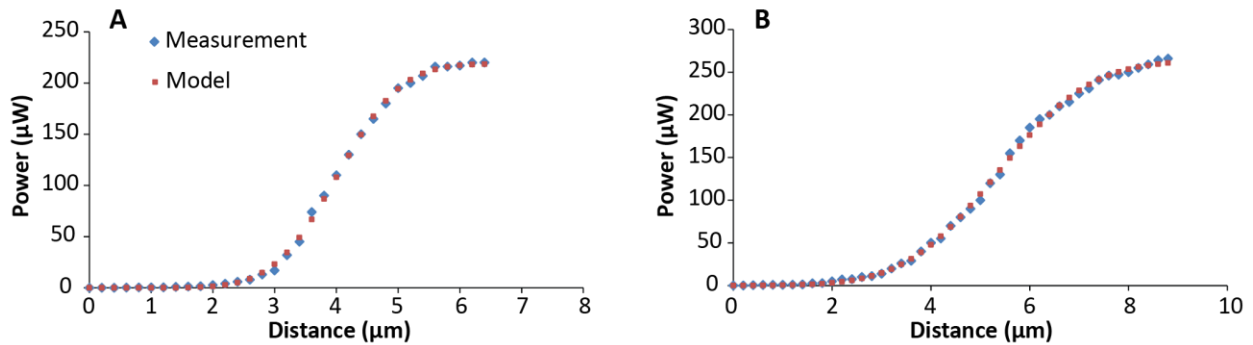

Figure A1.4. Laser beam profile characterization by knife-edge method. The beam diameter of 3.2 μm and 6 μm are obtained from curve fitting of the power readings with varying blocking distance for the 20X objective lens (A) and 10X objective lens (B).

A1.4. Characterization of grain boundaries using Secco etching

The commercial Secco etchant, used to prepare the crystallized samples for morphology characterization, consists of a mixture of $K_2Cr_2O_7$, HF, and H_2O [2]. The Secco etching process involves wet etching in a solution of 1 part of the commercial Secco etchant diluted with 4 parts of DI water, where dilution reduces the etching rate and improves process control with etching time. A final 3-second dip in 5:1 buffered hydrofluoric (BHF) acid is necessary to remove any thin oxide layer on the surface of c-Si grains due to oxidization during Secco etching. Because of a faster reaction rate with a-Si and crystalline defects such as grain boundaries, Secco etching is successfully employed to delineate the grain boundaries of crystallized Si film with moderate etching time (45 seconds), or to remove both a-Si and fine c-Si grains (tens of nanometers in lateral dimensions) under heavy Secco etching (**Fig. A1.5**).

The black circle from the SEM image (**Fig. A1.5A**) highlights the boundary between the a-Si region and the fine c-Si region, due to a step change in height (**Fig. A1.5B**) as measured by laser confocal microscope. The proposed mechanism for selectively removing fine c-Si grains while leaving larger lateral c-Si grains intact is from a lift-off process (**Fig. A1.6**). Secco etching removes Si in the dense grain boundaries of the fine c-Si region, and opens a channel across the thickness of the film to the quartz substrate in about 60 seconds. As the Secco etchant contains HF, further Secco etching removes the SiO_2 under the fine c-Si grains, resulting in those fine c-Si

grains being lifted off. The lateral c-Si grains are typically more than 100 nm in the shortest lateral dimension, which requires an even longer etching time for lift-off. Due to the difference in the removal mechanism between a-Si and fine c-Si grains, step changes in height form at the boundary between the initially a-Si region and the initially fine c-Si region.
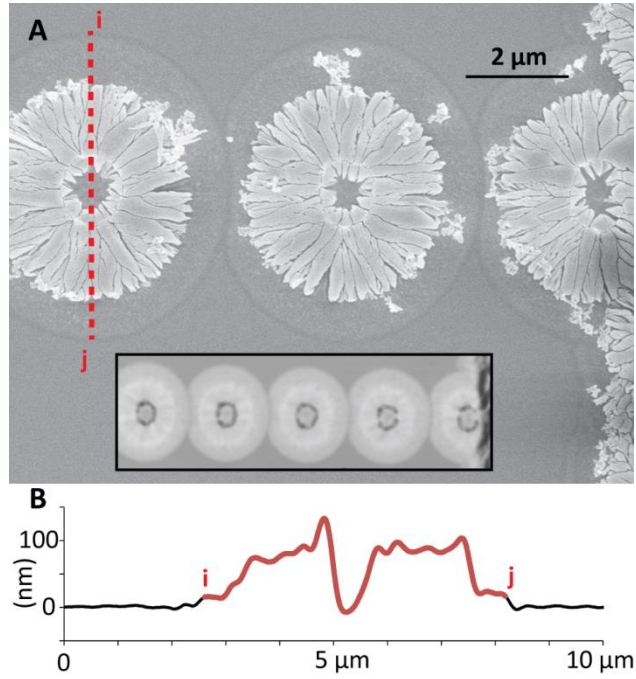
Figure A1.5. Morphology characterization of the crystallized Si film after heavy Secco etching. In the SEM image (A), both the a-Si outside the black circle and the fine c-Si grains inside the black circle are removed after 2-minute etching. The inset, from laser confocal image of the same area, shows that the boundary of the phase-change area before Secco etching corresponds to the black circle in the SEM image. The highlighted (red) height profile (B) corresponds to the dotted line.
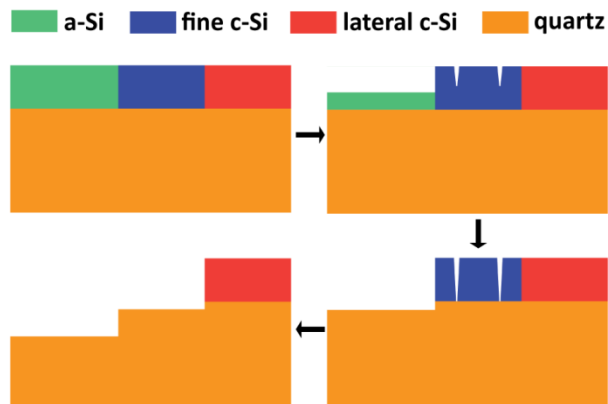
Figure A1.6. The proposed lift-off mechanism of fine c-Si grains during heavy Secco etching. A-Si is removed by directly reacting with the Secco etchant, while fine c-Si grains are likely to be removed by lift-off. The diffferent mechanisms result in different volume of the quartz substrate being etched away, and a step change in height at the boundary between the two regions is observable.

90

A1.5. Optical absorption in thin films VS the Beer's law

Due to the wave effect at a length scale smaller than the light wavelength (532 nm), the

optical activities (reflection, absorption, and transmission) for the 100 nm a-Si film could

deviates significantly from the bulk values as highlighted in **Table A1.1**, based on finite-

difference time-domain (FDTD) simulations. Another notable difference is 73% higher reflection

from the c-Si film than that from bulk c-Si materials. Applying the Beer's law to the 100 nm

liquid silicon (l-Si) film is valid, as the absorption coefficient of l-Si is more than 7 times of a-Si's

absorption coefficient at 532 nm (**Table A1.2**). As a result, the reflection and absorption values

from the FDTD approach agree with the bulk values.

Table A1.1. Comparison of reflection, absorption, and transmission of 532 nm laser energy between FDTD approach and bulk values.

	FDTD approach			Bulk values		
	Reflection	Absorption	Transmission	Reflection	Absorption	Transmission
c-Si	0.65	0.05	0.30	0.37	0.06	0.56
a-Si	0.40	0.50	0.10	0.44	0.44	0.12
l-Si	0.70	0.30	0.00	0.71	0.29	0.00

Table A1.2. Optical properties of Si at 532 nm wavelength.

	n	k	Reflectance	$\alpha \ (cm^{-1})$
c-Si [3]	4.15	0.044	0.37	1.039E+04
a-Si [4]	4.86	0.654	0.44	1.544E+05
l-Si [5]	2.53	4.74	0.71	1.120E+06
quartz [6]	1.547	0	0.046	0

Figure A1.7 is generated from FDTD simulations, showing the per unit volume optical

absorption for the thin film with a quartz substrate in the bottom and with a plane wave

incident from the top. Sensitivity analysis with varying a-Si film thickness is also carried out to

gauge the uncertainties in light absorption due to imperfect control of the film thickness during micro-fabrication process. As shown in **Fig. A1.7D**, the range of uncertainties for the normalized light absorption (per 100 nm thickness) is from -10.5% to 3.0%.

The FDTD simulation is carried out in Lumerical FDTD solutions version 8.0. Periodic boundary condition is applied in the x direction (along the film), and perfectly matched layers (PML) boundary condition is applied in the y direction (across the film) where light exiting the simulation volume will be completely absorbed.
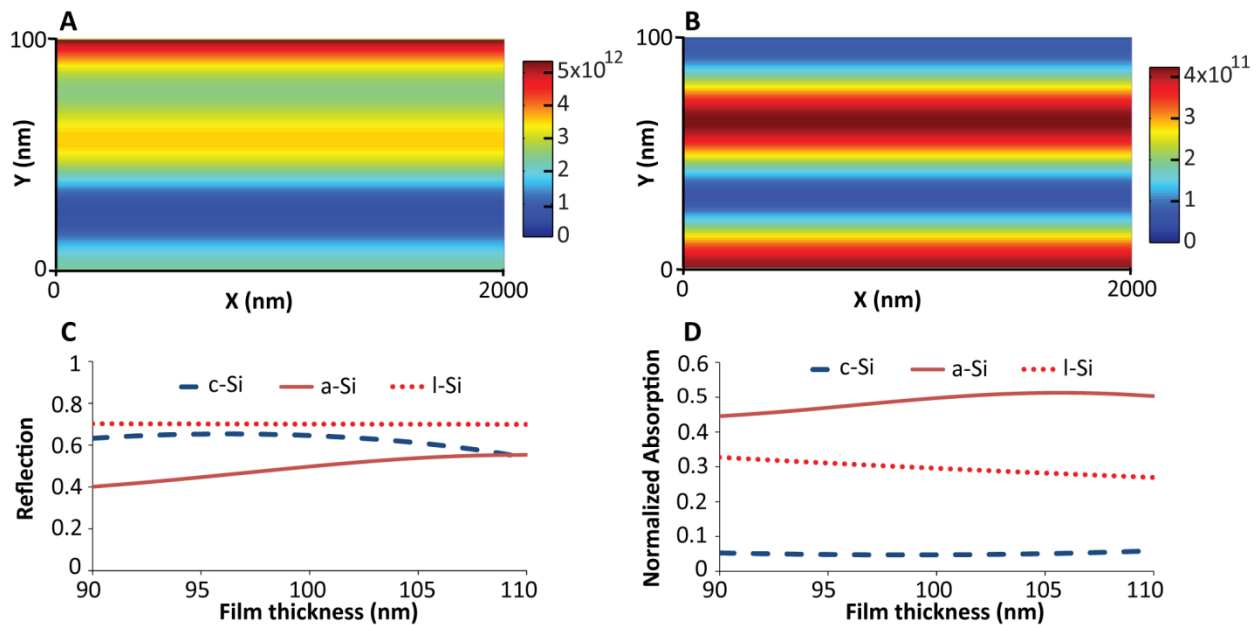
Figure A1.7. Light reflection and absorption in the 100-nm-thick Si film. For a-Si (A) and c-Si (B) film, the wave effect is significant. Sensitivity analysis for reflection (C) and normalized absorption (D) with varying film thickness shows the uncertainties due to imperfect fabrication process.

A1.6. Dry etching of thin films

During the fabrication of nanostructures, dry etching of thin films has been employed to remove Si, SiO_x, SiN_x, and photoresist (PR). The etching process is carried out inside the Plasma-Therm PK-12 reactive ion etcher (RIE). The recipes for etching different materials are listed in **Table A1.3**. Etching time is varied according to the individual application. For short duration of

etching such as 5 seconds, the power ramp-up time should be considered as part of the total etching time.

Table A1.3. RIE dry etching recipes for various.

	CHF3 (sccm)	O2 (sccm)	SF6 with 10% O2 (sccm)	Power (W)	Estimated etch rate (nm/min)
a-Si			50	50	~ 600
SiNx			90	200	~ 120
SiOx	80	4		150	~ 30
PR descum		60		100	< 200
PR ash		80		200	< 350

For example, the micro-ring arrays are produced after removal of background a-Si film by RIE dry etching. 5-second oxide etching is always performed before a-Si or SiN_x etching, to remove any thin oxide layer on the surface, which can be an etching barrier for SF_6 chemistry.

In preparing the suspended bridge for laser crystallization in reduced dimensions, a 30-second PR descum process is first applied to remove any residual PR in the developed pattern, and 5-second oxide etching is applied to remove any thin oxide before etching Si and SiN_x with SF_6. Finally, the PR pattern is ashed by oxygen plasma with high power. A 30-second BHF wet etching is used to clean away the surface oxide layer generated during the oxygen plasma, and to expose the pristine Si surface.

A1.7. Process flow of fabricating suspended a-Si membranes

In order for the a-Si membranes to be mechanically stable during pulsed laser crystallization, where the a-Si is heated to its molten liquid phase, the 100-nm nitride layer in the sandwiched a-Si/SiN_x/a-Si structure (**Fig. A1.8**) is designed to provide mechanical support while a-Si layers are molten. Absorbing laser energy at the same time, the bottom a-Si layer serves as a heated substrate and reduces the heat loss rate from the top a-Si layer to the nitride layer.

Figure A1.8 shows the major steps for fabricating the suspended a-Si membranes. First, a 1.3-μm-thick G-line photoresist (PR) is spin-coated at 5000 rpm. Second, laser lithography with 532-nm wavelength nanosecond pulsed laser is used to define in-plane patterns of the bridges, where a combined effect of light and heat makes the PR easily removable in a standard G-line PR developer. The hard-baked (for 30 minutes at 120 ^{0}C) sample goes through 30-second PR descum and 5-second oxide dry etching, to improve the reproducibility of the subsequent Si etching steps. The patterns in the PR layer are transferred to the a-Si/SiN_x/a-Si sandwich layers by plasma dry etching with the recipes listed in **Table A1.3**. The suspended structure is made

by undercutting the oxide layer while immersing the sample in 5:1 BHF solution for 15 minutes. Finally, the PR layer is ashed away by oxygen plasma etching for 6 minutes.
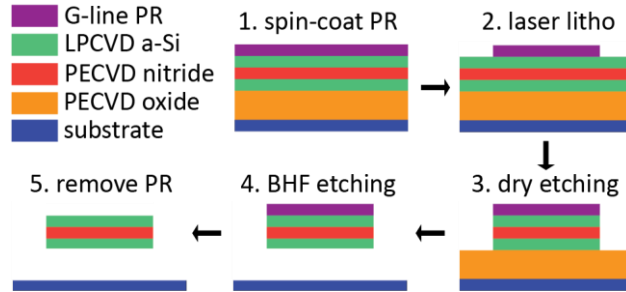

Figure A1.8. Process flow for fabricating suspended a-Si membranes. Laser lithography on the photoresist layer writes an opening between two membranes, and subsequent dry etching and BHF wet etching lead to suspended a-Si membranes.

A2. Regression Analysis on PV Innovation

Table A2.1. Summary of the PV patent data by technology. The technology category of the patent applications (PV or solar thermal) is defined using the IPC Green Inventory, which lists a range of IPC classes for a given technology.

	U.S.	China	Japan	Germany	World	c-Si PV
PV	2,187	277	1,969	976	7,055	932
Solar thermal	341	59	93	209	1,307	15
Total	3,300	411	2,232	1,459	9,987	1,150

From **Table A2.1**, we note that around 10% of the PV patents are likely to be related to solar thermal technologies, which are removed from the final PV patent data presented in **Fig. 6.7** and **Fig. 6.9**. Due to the additional keyword "silicon", only 1.5% of the c-Si PV patents are likely to be related to solar thermal technologies. After a manual inspection of these 15 patents, we find 12 of them are PV patents but have misleading IPC classes, 1 of them is about hybrid-PV-solar-thermal technology. Therefore, the c-Si PV patent data has not been refined using IPC classes to avoid introducing greater inaccuracy.

We run linear regression models (**Eqs. A2.1-A2.5**) for both c-Si PV and First Solar's thin film PV data. The summary of key regression results are in **Tables A2.2** and **Table A2.3**.

$$\log P_i = \alpha_0 + \alpha_1 \log(CQ_i)$$

<div align="right">**Equation A2.1**</div>

$$\log P_i = \alpha_0 + \alpha_1 \log(Q_i)$$

<div align="right">**Equation A2.2**</div>

$$\log T_i = \alpha_0 + \alpha_1 \log(CQ_i)$$

<div align="right">**Equation A2.3**</div>

$$T_i = \alpha_0 + \alpha_1 \log Q_i + \eta_i$$

<div align="right">**Equation A2.4**</div>

$$\log P_i = \alpha_0 + \alpha_1 \log Q_i + \alpha_2 \eta_i + \epsilon_i$$

<div align="right">**Equation A2.5**</div>

The coefficients of the two-factor learning curve model (**Eq. 6.3**) can be derived from **Eqs. A2.4 and A2.5**, yielding **Eqs. A2.6-A2.8**.

$$\beta_0 = \theta_0 - \theta_2 \cdot \alpha_0$$

<div align="right">**Equation A2.6**</div>

$$\beta_1 = \theta_1 - \theta_2 \cdot \alpha_1$$

<div align="right">**Equation A2.7**</div>

$$\beta_2 = \theta_2$$

<div align="right">**Equation A2.8**</div>

Table A2.2. Summary of key regression results for c-Si PV modules. Standard error of the coefficient is in parenthsis. The p-value follows the convention: ***<0.001<**<0.01<*<0.05. Minimization of the values from the Bayesian Information Criterion (BIC) suggests the best model.

	A2.1 (1976-2010)	A2.1 (1991-2010)	A2.2 (1991-2010)	A2.3 (1991-2010)	A2.4 (1991-2010)	A2.5 (1991-2010)
α_0	1.79178 (0.05238) ***	1.46396 (0.08217) ***	1.17325 (0.05506) ***	-0.74792 (0.05948) ***	-640.47 (89.08) ***	1.17325 (0.04730) ***
α_1	-0.33909 (0.01869) ***	-0.23733 (0.02432) ***	-0.19029 (0.02023) ***	0.84159 (0.0176) ***	326.73 (32.72) ***	-0.19029 (0.01738) ***
α_2						-0.0003402 (0.0001252) *
R^2	0.9089	0.8411	0.8310	0.9922	0.8471	0.8822
BIC	-45.38	-46.29	-45.06	-59.22	250.5	-49.28
LR	20.9%	15.2%	12.4%			
Q at $0.5/W	1.5 TW	27 TW	56 TW			

Based on the BIC values, the conventional model during 1991-2010 is a better fit to data after adjusting for the fact that the conventional model during 1976-2010 has 75% more data points, yielding a better R-square value. The two-factor model (**Eq. A2.5**) is a further improvement, with a lower BIC value and better R-square value than both the conventional model (**Eq. A2.1**, 1991-2010) and the "economies of scale" model (**Eq. A2.2**).

Table A2.3. Summary of key regression results for First Solar's thin film PV modules.

	A2.1 (2006Q1-2010Q4)	A2.1 (2006Q1-2012Q4)	A2.2 (2006Q2-2010Q4)	A2.3 (2006Q1-2010Q4)	A2.4 (2006Q2-2010Q4)	A2.5 (2006Q2-2010Q4)
α_0	0.644524 (0.02080) ***	0.61933 (0.01605) ***	0.51882 (0..02416) ***	0.30092 (0.1222) *	-62.7 (24.52) *	0.51882 (0.01763) ***
α_1	-0.22054 (0.007514) ***	-0.20998 (0.005222) ***	-0.23822 (0.01156) ***	0.48395 (0.04415) ***	54.54 (11.74) ***	-0.23822 (0.00844) ***
α_2						-0.0006956 (0.0001744) **
R^2	0.9795	0.9842	0.9615	0.8697	0.5595	0.9807
BIC	-94.43	-135.97	-80.21	-23.59	183	-90.38
LR	14.2%	13.5%	15.2%			13.0%
Q at $0.4/W	53 GW	70 GW	7GW			

Table A2.4. The importance of the U.S., China, Japan, and Germany in the global PV energy landscape in 2010. Source: EIA , EPI, EPIA, WIPO, and World Bank.

	U.S.	China	Japan	Germany	World	The top four's world share
GDP (2010 US$ billions)	14,419	5,931	5,488	3,284	63,195	46%
PV market size (GW)	0.88	0.52	0.99	7.41	16.82	58%
Cumulative PV capacity (GW)	2.53	0.89	3.62	17.19	40.02	61%
PV manufacturing (GW)	1.12	10.85	2.17	2.02	24.05	67%
Annual PCT patent applications (#)	685	142	492	306	2,198	74%
National electricity consumption (TWh)	3,886	3,634	1,002	549	18,466	49%

References:

1 *Gaussian beams and the knife-edge measurement*, <http://massey.dur.ac.uk/resources/grad_skills/KnifeEdge.pdf> (2014).
2 Secco d' Aragona, F. Dislocation etch for (100) planes in silicon. *J. Electrochem. Soc.* **119**, 948-951, doi:10.1149/1.2404374 (1972).
3 Palik, E. D. *Handbook of Optical Constants of Solids*. (Academic Press, 1985).
4 Refractive Index Database. *Optical constants of amorphous silicon*, <http://refractiveindex.info/> (2014).
5 Unamuno, S., Toulemonde, M. & Siffert, P. *Melting model for UV lasers*. Vol. 3 (Springer, 1984).
6 Ghosh, G. Dispersion-equation coefficients for the refractive index and birefringence of calcite and quartz crystals. *Opt. Commun.* **163**, 95-102, doi:10.1016/S0030-4018(99)00091-7 (1999).